Experimental Adsorption and Reaction Studies on Transition Metal Oxides Compared to DFT Simulations

Han Chen

Dissertation submitted to the faculty of the Virginia Polytechnic Institute and State University in partial fulfillment of the requirements of the degree of

Doctor of Philosophy

In

Chemical Engineering

David F. Cox

William A. Ducker

Ayman M. Karim

Hongliang Xin

May, 10, 2021

Blacksburg, VA

Keywords: Benchmark, density functional theory, temperature-programmed desorption, adsorption, reaction, manganese oxide, chromia

Experimental Adsorption and Reaction Studies on Transition Metal Oxides Compared to DFT Simulations

Han Chen

ABSTRACT

A temperature-programmed desorption (TPD) study of CO and NH_3 adsorption on MnO(100) with complimentary density functional theory (DFT) simulations was conducted. TPD reveals a primary CO desorption signal at 130 K from MnO(100) in the low coverage limit giving an adsorption energy of -35.6 $\pm$2.1 kJ/mol on terrace sites. PBE+U gives a more reasonable structural result than PBE, and the adsorption energy obtained by PBE+U and DFT-D3 Becke-Johnson gives excellent agreement with the experimentally obtained ΔE_{ads} for adsorption at Mn^{2+} terrace sites. The analysis of NH_3-TPD traces revealed that adsorption energy on MnO(100) is coverage-dependent. At the low-coverage limit, the adsorption energy on terraces is -58.7$\pm$ 1.0 kJ/mol. A doser results in the formation of a transient NH_3 multilayers that appears in TPD at around 110K. For a terrace site, PBE+U predicts a more realistic surface adsorbate geometry than PBE does, with PBE+U with Tkatchenko-Scheffler method with iterative Hirshfeld partitioning (TSHP) provides the best prediction.

DFT simulations of the dehydrogenation elementary step of the ethyl and methyl fragments on α-$Cr_2O_3(10\bar{1}2)$ were also conducted to complement previous TPD studies of these subjects. On the nearly-stoichiometric surface of α-$Cr_2O_3(10\bar{1}2)$, CD_3- undergoes dehydrogenation to produce CD_2=CD_2 and CD_4. Previous TPD traces suggest that the α-hydrogen (α-H) elimination of methyl groups on α-$Cr_2O_3(10\bar{1}2)$ is the rate-limiting step, and has an activation barrier of 135 $\pm$ 2 kJ/mol. DFT simulations showed that PBE gives reasonable prediction of the adsorption sites for CH_3- fragments in accordance with XPS spectra, while PBE+U did not. Both PBE and PBE+U failed to predict the correct adsorption sites for CH_2=. When the simulation is set in accordance with the experimentally observed adsorption sites for the carbon species, PBE gives very accurate prediction on the reaction barrier when an adjacent I adatom is present, while PBE+U failed spectacularly. When the simulation is set in accordance with the DFT-predicted adsorption sites, PBE is still able to accurately predict the reaction barrier (<1% to 8.7% error) while PBE+U is less accurate. DFT is also used to complement the previous study of the β-H elimination an ethyl group on the α-$Cr_2O_3(10\bar{1}2)$ surface. The DFT simulation shows that absent surface Cl adatoms, PBE predicts an activation barrier of 92.6 kJ/mol, underpredicting the experimental activation barrier by 28.7%, while PBE+U predicts a barrier of 27.0 kJ/mol, under-predicting the experimental barrier by 79.2%. The addition of chlorine on the adjacent cation improved the prediction on barrier by PBE+U marginally, while worsened the prediction by PBE marginally.

Grant information

Financial support provided by the U.S. Department of Energy through grant DE-FG02-97ER14751.

Experimental Adsorption and Reaction Studies on Transition Metal Oxides Compared to DFT Simulations

Han Chen

General Audience Abstract

Nowadays, density functional theory (DFT), a computational approach to chemistry has become increasingly more popular due to it being less computationally expensive than other traditional computational approaches. One major shortcoming of DFT is its inability to explain the electronic interactions within transition metal oxides, where the electronic configuration within one cation is intimately linked to those on adjacent cations. To address this, DFT+U, a variant of DFT, has been developed to better account for these special electronic interactions. However, not enough experimental comparisons have been established to verify the accuracy of DFT and DFT+U.

Our lab focuses on providing high quality experimental benchmarks that can be readily compared to by the DFT community. To establish the experimental benchmarks, we use a technique called temperature-programmed desorption (TPD), which focuses on measuring the rate at which gas molecules leave a sample surface populated with a pre-determined amount of gas molecules as the temperature of the surface is raised at constant but slow temperature ramp rate. Through analysis of the results, the adsorption energy can be obtained for a desorption process, or an activation barrier if the desorption is the result of a surface reaction. Some simple calculations involving PBE, a popular functional used in the DFT community, and its variant PBE+U were conducted for comparison purposes. The transition metal oxide surfaces chosen in this study is MnO(100) and of α-$Cr_2O_3(10\bar{1}2)$, because they both possess the special electronic interactions between their own cations.

For adsorption studies, we determined adsorption energies of carbon monoxide (CO), and ammonia (NH_3) on MnO(100) single crystal surface. For CO, TPD study revealed that CO undergoes weak adsorption on the surface, with no dissociation of CO detected. PBE predicts an unreasonable surface adsorption geometry while PBE+U predicts a reasonable one. When coupled with a particular dispersion correction method named DFT-D3 Becke-Johnson, PBE+U predicts a very accurate adsorption energy of CO on MnO(100). TPD shows that NH_3 undergoes a stronger adsorption on MnO(100) with no dissociation of NH_3. Similarly, PBE+U predicted a more reasonable adsorption geometry while PBE did not. Coupled with a dispersion correction named Tkatchenko-Scheffler method with iterative Hirshfeld partitioning (TSHP), PBE+U provides an accurate prediction of adsorption energy. In comparison to previous experimental works based on TPD results, the simple decomposition reactions of an ethyl group and a methyl group were also studied on α-$Cr_2O_3(10\bar{1}2)$ surface using DFT. Overall, PBE gave better prediction on the activation barrier than PBE+U did in comparison to experimentally observed barriers.

Acknowledgements

First, I would like to thank my adviser Dr. David F. Cox, for his teachings and guidance over the past eight years. With the conclusion of his career as the department head I wish for him a happy and relaxing retirement in Florida. I would also like to thank my committee members Dr. William Ducker, Dr. Ayman M. Karim, Dr. Hongliang Xin for their advice on my PhD endeavor. My thanks also go to the previous students from the lab, Xu Feng, who was like a mentor to me, John Brooks, Chad Byrd, Yujung Dong, Mary Minton, and Steven York. Reading your dissertations deeply humbles me, and if I have seen further, it is by standing on the shoulders of giants.

My gratitude should also go to the chemical engineering staff of the department, including but not limited to, Diane Cannaday, Tina Russell, Andrea Linkous, Stacey Ratcliffe. Special thanks should also go to the machine shop staff Kevin Holshouer and Michael Vaught, who have generously allocated their time to make niche items I needed. I would like to thank Bradley Reed who has helped me also with niche tasks as well.

During my time at Virginia Tech I had the fortune of starting a music band of many genres with the following talented members: Wenhui Li, Ayaan Kazerouni, Gregory Lambert, Ethane Smith, Saikat Mukherjee, Kirkland Broadwell, and Disha Sardana. Your beautiful talents brought happiness and inspirations to me and I will always remember.

Special thanks should also go to Dr. Abhiram Arunkumar, who has given me many invaluable pieces of advice regarding my PhD and has render assistance to me and my wife in other capacities. We are forever grateful. Thanks should also go to my roommate James Dickmann, I enjoyed our many lunches together with banters back and forth. I would also like to thank Satoshi Nakamoto, whose invention has not only bettered my financial situation, but has also taught me valuable lessons on the human nature. You inspired me to think differently about science and about the world.

I would also like to thank my mother, Lin Kang, whose support in every capacity helped kick start, and sustained my PhD endeavor. Thank you, mom!

A very special acknowledgement should be mentioned for my wife Ai Lin Chin, who has stood by me through the best, and the worst periods of my PhD endeavor. Without her my journey certainly would not have been successful. I look forward to sharing the fruits of my labor and the rest of my life with her.

Table of contents

List of figures

List of tables

Chapter 1

Introduction

1.1 Density functional theory and benchmarks for transition metal oxide surface chemistry

Density functional theory (DFT) [1-3] is widely used to provide insight into fundamental processes on surfaces such as adsorption and surface reactions. While it is widely applied, the applicability of DFT and related methods to highly correlated systems with unpaired d electrons like transition metal oxides remains problematic [4, 5]. For surface chemistry in particular, the lack of benchmark experimental data for adsorption and reaction systems on well-defined single crystal transition metal oxide surfaces continues to be an issue in determining the applicability of different DFT methods in transition metal oxide catalysis. A goal of this work is to provide these experimental benchmarks for a few systems.

The DFT + U [6] method employees a parameterized Hubbard-type on-site coulomb repulsion term that has found significant success in improving DFT predictions for highly correlated systems. However, the parameters are generally determined from bulk experimental properties (energies of formation, lattice parameters, bulk modulus, band gaps, cation magnetic moments, etc.), so the applicability of parameters determined from bulk properties to questions of surface phase stability and surface chemistry is "subject to some uncertainty" [7]. Nevertheless, this method has found wide-spread use in computational studies of transition metal oxide catalysis using +U parameters determined from bulk data. These benchmarks established here for a few initial systems may provide

guidance to the theoretical community that is actively working on modifications to DFT to handle such systems.

1.2 Choosing transition metal oxide surfaces and gas molecules

Considering the type of benchmark that need to be established, several factors should be considered when choosing surfaces for adsorption or reaction studies. First, the bulk of the transition metal oxide must have strongly correlated electronic structures due to the presence of unpaired d-electrons. Materials such as MnO, FeO, CoO, NiO [8], Cr_2O_3 [9] and V_2O_3 [10] satisfy this requirement. Further, a well-established procedure to achieve a clean, well-define single crystal surface with mostly homogenous adsorption sites is necessary for direct comparison to periodic DFT slab calculations. Our lab is in possession of, and has demonstrated the ability to prepare clean and nearly-stoichiometric MnO(100) [11] and α-Cr_2O_3 ($10\bar{1}2$) and other single crystal oxide surfaces [12]. These materials have the additional benefit of having different d-electron counts, as Mn is $3d^5$ in MnO [13], while Cr is $3d^3$ in Cr_2O_3 [12]. Choosing these two surfaces for establishing adsorption and reaction benchmarks will serve as a starting point for providing the computational chemistry community with high-quality benchmarks on transition metal oxides with highly correlated electronic structures.

The molecules selected for benchmarking adsorption energy are carbon monoxide (CO) and ammonia (NH_3). CO is used because it is a simple, and widely-used probe for catalytic surfaces, including single crystal surfaces [14-22], while NH_3 is widely used as a probe of acidic sites on oxide surfaces [23-26]. These two small molecules typically undergo unactivated adsorption. This is an important property because the activation energy for desorption can be directly related to the adsorption enthalpy which can be

compared to DFT total energy calculations [27, 28]. For reaction systems, the halogenated hydrocarbon CH_3CH_2Cl and CH_3I are chosen because they have been demonstrated to undergo dissociative adsorption on various surface [29-37], breaking carbon-halogen bonds and providing an opportunity to study simple alkyl surface chemistry for methyl and ethyl surface intermediates.

1.3 DFT methods and functionals selected

It is also of interest to conduct some basic DFT calculations for comparing to the experimental results. The Perdue-Burke-Ernzerhof (PBE) [38], the most widely used functional is chosen to be used in all calculations for its popularity. The +U package [39] in addition to PBE is also used, as it purportedly is superior at handling systems with highly correlated electrons. For adsorption systems (found in chapter 2 and 3), geometric relaxation simulations of the adsorbed state and the free state (where gas molecules and surface are simulated separately) are done separately to determine the adsorption energy using both PBE and PBE+U. For reaction systems (found in chapter 4 and 5), geometric relaxation simulations of the initial state and the final state of the reactions are done first, followed by the climbing image nudged elastic band [40, 41] calculations to determine the minimum energy pathways and the transition states, also using PBE and PBE+U. The results can be readily compared to the experimental results.

1.4 Objective

Within this work, adsorption system studies that can found in chapter 2 and 3. the experimental adsorption energy benchmarks of CO and NH_3 on well-defined single-crystal MnO(100) surface are established using temperature-programmed desorption (TPD). Also

found with these benchmarks are calculations of the two adsorption systems using PBE and PBE+U. For reaction systems, we used PBE and PBE+U to calculate the activation barriers for α-hydrogen elimination from methyl groups (chapter 4) and the β-hydrogen elimination of the ethyl groups (chapter 5), and the results are compared to previously established experimental activation barriers for the reactions in question.

In addition to the reported studies, attempts were also made to determine experimental adsorption energies of CO and NH_3 on α-Cr_2O_3 $(10\bar{1}2)$, but were not successful due to the surface being highly defective despite our best efforts at preparation. In addition, attempts were also made to study the α- and β-hydrogen elimination on MnO(100), but these efforts were not successful due to a lack of dissociation of the reaction precursors under a wide range of thermal conditions. Efforts to promote carbon halogen bond cleavage via electron stimulation were also unsuccessful.

References

[1] W. Kohn, L.J. Sham, Self-consistent equations including exchange and correlation effects, Physical Review, 140 (1965) A1133.

[2] P. Hohenberg, W. Kohn, Inhomogeneous Electron Gas, Physical Review, 136 (1964) B864-B871.

[3] A. Sarmah, Density Functional Theory (DFT): Periodic Advancement and New Challenges, Research Methodology in Chemical Sciences: Experimental and Theoretical Approach, (2017) 219.

[4] C. Franchini, V. Bayer, R. Podloucky, J. Paier, G. Kresse, Density functional theory study of MnO by a hybrid functional approach, Physical Review B, 72 (2005) 045132.

[5] A.J. Cohen, P. Mori-Sánchez, W. Yang, Insights into Current Limitations of Density Functional Theory, Science, 321 (2008) 792-794.

[6] V.I. Anisimov, F. Aryasetiawan, A. Lichtenstein, First-principles calculations of the electronic structure and spectra of strongly correlated systems: the LDA+ U method, Journal of Physics: Condensed Matter, 9 (1997) 767.

[7] A. Rohrbach, J. Hafner, G. Kresse, Ab initio study of the (0001) surfaces of hematite and chromia: Influence of strong electronic correlations, Physical Review B, 70 (2004) 125426.

[8] W. Roth, Magnetic structures of MnO, FeO, CoO, and NiO, Physical Review, 110 (1958) 1333.

[9] L. Corliss, J. Hastings, R. Nathans, G. Shirane, Magnetic structure of Cr_2O_3, Journal of Applied Physics, 36 (1965) 1099-1100.

[10] M. Brahlek, L. Zhang, J. Lapano, H.-T. Zhang, R. Engel-Herbert, N. Shukla, S. Datta, H. Paik, D.G. Schlom, Opportunities in vanadium-based strongly correlated electron systems, MRS Communications, 7 (2017) 27-52.

[11] X. Feng, D.F. Cox, Na Deposition on MnO (100), Surface Science, 645 (2016) 23-29.

[12] A.H. Hill, A. Harrison, C. Dickinson, W. Zhou, W. Kockelmann, Crystallographic and magnetic studies of mesoporous eskolaite, Cr_2O_3, Microporous and Mesoporous Materials, 130 (2010) 280-286.

[13] J. Van Elp, R. Potze, H. Eskes, R. Berger, G. Sawatzky, Electronic structure of MnO, Physical Review B, 44 (1991) 1530.

[14] J. Heidberg, M. Kandel, D. Meine, U. Wildt, The monolayer CO adsorbed on MgO (100) detected by polarization infrared spectroscopy, Surface Science, 331 (1995) 1467-1472.

[15] G. Pacchioni, T. Minerva, P.S. Bagus, Chemisorption of CO on defect sites of MgO, Surface Science, 275 (1992) 450-458.

[16] R. Wichtendahl, M. Rodriguez-Rodrigo, U. Härtel, H. Kuhlenbeck, H.J. Freund, Thermodesorption of CO and NO from Vacuum-Cleaved NiO (100) and MgO (100), Physical Status Solidi A, 173 (1999) 93-100.

[17] S. Briquez, C. Girardet, J. Goniakowski, C. Noguera, Molecular adsorption on unrelaxed and relaxed ionic steps. Application to Ar, CO, CO_2, and NH_3 adsorbed on MgO (001), The Journal of Chemical Physics, 105 (1996) 678-685.

[18] Z. Dohnalek, G.A. Kimmel, S.A. Joyce, P. Ayotte, R.S. Smith, B.D. Kay, Physisorption of CO on the MgO (100) Surface, The Journal of Physical Chemistry B, 105 (2001) 3747-3751.

[19] S.M. Vesecky, X. Xu, D.W. Goodman, Infrared study of CO on NiO (100), Journal of Vacuum Science & Technology A: Vacuum, Surfaces, and Films, 12 (1994) 2114-2118.

[20] R. Wichtendahl, M. Rodriguez-Rodrigo, U. Härtel, H. Kuhlenbeck, H.-J. Freund, TDS study of the bonding of CO and NO to vacuum-cleaved NiO (100), Surface Science, 423 (1999) 90-98.

[21] D. Cappus, J. Klinkmann, H. Kuhlenbeck, H.-J. Freund, CO on NiO (100): orientation and bonding, Surface Science, 325 (1995) L421-L427.

[22] A. Rohrbach, J. Hafner, G. Kresse, Molecular adsorption on the surface of strongly correlated transition-metal oxides: A case study for CO/NiO (100), Physical Review B, 69 (2004) 075413.

[23] M.W. Abee, D.F. Cox, NH_3 chemisorption on stoichiometric and oxygen-deficient SnO_2(110) surfaces, Surface Science, 520 (2002) 65-77.

[24] D. Arthur, D. Meixner, M. Boudart, S. George, Adsorption, desorption, and surface diffusion kinetics of NH_3 on MgO (100), The Journal of Chemical Physics, 95 (1991) 8521-8531.

[25] S. Koust, K.C. Adamsen, E.L. Kolsbjerg, Z. Li, B. Hammer, S. Wendt, J.V. Lauritsen, NH_3 adsorption on anatase-TiO_2 (101), The Journal of Chemical Physics, 148 (2018) 124704.

[26] M.C. Wu, C.M. Truong, D.W. Goodman, Interactions of ammonia with a nickel oxide (100) surface studied by high-resolution electron energy loss spectroscopy and temperature programmed desorption spectroscopy, The Journal of Physical Chemistry, 97 (1993) 4182-4186.

[27] W. Brown, R. Kose, D. King, Femtomole adsorption calorimetry on single-crystal surfaces, Chemical Reviews, 98 (1998) 797-832.

[28] J. Wellendorff, T.L. Silbaugh, D. Garcia-Pintos, J.K. Nørskov, T. Bligaard, F. Studt, C.T. Campbell, A benchmark database for adsorption bond energies to transition metal surfaces and comparison to selected DFT functionals, Surface Science, 640 (2015) 36-44.

[29] C.M. Byrd, Reaction chemistry of C_1 hydrocarbon fragments and oxygenates on Cr_2O_3 (1012), in, Virginia Tech, 2003.

[30] Y. Dong, J.D. Brooks, T.-L. Chen, D.R. Mullins, D.F. Cox, Reactions of methyl groups on a non-reducible metal oxide: The reaction of iodomethane on stoichiometric α-Cr_2O_3 (0001), Surface Science, 641 (2015) 148-153.

[31] F. Solymosi, L. Bugyi, A. Oszkó, Generation of C_2H_5 species: Thermal and photoinduced dissociation of C_2H_5I on Rh (111), Langmuir, 12 (1996) 4145-4152.

[32] C. Su, J.-C. Yeh, C.-C. Chen, J.-C. Lin, J.-L. Lin, Study of adsorption and reactions of methyl iodide on TiO_2, Journal of Catalysis, 194 (2000) 45-54.

[33] F. Solymosi, K. Révész, Spectroscopic study on the adsorption and dissociation of CH_3I on Pd (100): thermal and photo effects, Surface Science, 280 (1993) 38-49.

[34] C. Bol, C. Friend, Effects of Oxygen Coverage on the Partial Oxidation of Methylene: Reactions of Diiodomethane on Oxygen-Covered Rh (111), Journal of the American Chemical Society, 117 (1995) 11572-11579.

[35] J.D. Brooks, Q. Ma, D.F. Cox, Reactions of ethyl groups on a model chromia surface: Ethyl chloride on stoichiometric α-Cr_2O_3 (101¯2), Surface Science, 603 (2009) 523-528.

[36] F. Zaera, Formation and thermal decomposition of ethyl groups on transition metal surfaces: Ethyl iodide on Pt (111), Surface Science, 219 (1989) 453-466.

[37] X.-L. Zhou, J. White, Alkyl halide photochemistry on Ag (111): III. Methyl iodide, Surface Science, 241 (1991) 270-278.

[38] J.P. Perdew, K. Burke, M. Ernzerhof, Generalized Gradient Approximation Made Simple, Physical Review Letters, 77 (1996) 3865-3868.

[39] S. Dudarev, G. Botton, S. Savrasov, C. Humphreys, A. Sutton, Electron-energy-loss spectra and the structural stability of nickel oxide: An LSDA+ U study, Physical Review B, 57 (1998) 1505.

[40] G. Henkelman, B.P. Uberuaga, H. Jónsson, A climbing image nudged elastic band method for finding saddle points and minimum energy paths, The Journal of Chemical Physics, 113 (2000) 9901-9904.

[41] G. Henkelman, H. Jónsson, Improved tangent estimate in the nudged elastic band method for finding minimum energy paths and saddle points, The Journal of Chemical Physics, 113 (2000) 9978-9985.

Chapter 2

CO adsorption on MnO(100): Experimental benchmarks compared to DFT[1]

2.1 Introduction

Density functional theory (DFT) provides a cost-effective way for addressing large-scale problems with first-principles calculations, however, the treatment of electron correlation remains a weakness of DFT [1-3]. This problem is severe for transition metal oxides with strongly correlated electronic structures [4, 5]. While progress has been made to address the problems [6-8], high-quality experimental benchmarks for adsorption and reaction on transition metal oxides remain scarce. Here we provide an adsorption energy benchmark for CO on MnO(100), a transition metal oxide with highly-correlated electronic structure [9, 10] and a simple rocksalt bulk structure [11].

Rocksalt is the simplest form of metal oxide in terms of the bulk structure [12], with the (100) surface being the most thermodynamically stable [13]. Known metal oxides with a rocksalt structure are MgO, CaO, TiO, VO, MnO, FeO, CoO, NiO, SrO, BaO, CdO, and EuO [12, 14, 15]. Among these materials, experimental studies for (100) surfaces are available on: MgO(100) [16-34], CaO(100) [35], MnO(100) [36, 37], FeO(100) [38], CoO(100) [39, 40], NiO(100) [18, 41-47], SrO(100) [48] and BaO(100) [49].

CO is a commonly used probe molecule for examining single crystal surfaces, however, with the exception of MgO(100) [17, 18, 21, 50, 51] and NiO(100) [18, 41-43, 52], detailed CO adsorption studies on single crystal metal oxide rocksalt (100) surfaces, experimental or computational, are scarce. To our knowledge, there are currently no

[1] This material has been published, H. Chen, D.F. Cox, Surface Science, (2021) 121808. and is reproduced with permission.

reported experimental studies of CO adsorption on MnO(100). The existing experimental studies on rocksalt oxide (100) surfaces have shown that CO is weakly adsorbed on rocksalt oxide (100) surfaces. The adsorption energy in the low-coverage limit is about -13 kJ/mol on MgO(100) [18], -27 kJ/mol on NiO(100) [18], and -28 kJ/mol on CaO(100) [35]. Above the low-coverage limit, adsorbate lateral repulsion [53, 54] lowers the adsorption energy as coverage increases, as observed on MgO(100) [18], NiO(100) [18] and CaO(100) [35]. If the sample is dosed at temperatures lower than 30 K, the formation of a CO multilayer can also be observed [18].

Experimental studies have revealed that CO adsorbs C-down onto the metal center on rocksalt (100) surfaces, with varying degrees of tilt of the CO molecule. For example, a polarization infrared spectroscopy study shows that CO adsorbs C-down onto surface Mg^{2+} cations on MgO(100) perpendicular to the surface plane [17]. On NiO(100), a photoelectron diffraction study shows that CO adsorbs C-down onto the metal center, with the Ni-C bond deviating 7 degrees from the surface normal, and the C-O bond by 12 degrees [55]. This tilt has been attributed to the interactions of unpaired d-electrons in the Ni^{2+} cation and the 1π orbital of adsorbed CO [52].

While no experimental studies are available for CO adsorption on MnO(100), one molecular orbital study utilizing an atom superposition and electron delocalization (ASED) technique and cluster models of stoichiometric MnO (100) [56] determined a CO adsorption energy of about -161 kJ/mol, and a perpendicular CO adsorbate geometry with carbon end down on the five-fold-coordinated Mn^{2+} site. The magnitude of this adsorption energy is large in comparison to those reported for other rocksalt oxide (100) surfaces [18, 35].

CO adsorption studies on MnO powders are also scarce, despite significant interest [57-61] in the use of manganese oxides powders (MnO_2, Mn_2O_3, Mn_3O_4) for the CO oxidation reaction [61, 62]. Among the manganese oxides, MnO shows less catalytic activity than other manganese oxides, resulting in less interests in MnO powders [62]. Despite this, a number of studies [63-65] have examined the interaction between CO molecules and Mn^{3+} and Mn^{2+} sites using infrared spectroscopy on oxidized and reduced MnO_x powder, respectively. A small (10 cm^{-1}) drop in C-O stretching frequency from Mn^{3+}-CO to Mn^{2+}-CO, was observed by Angevaare et al. [64], Kantcheva et al. [63], and Craciun et al. [65], which suggests that CO adsorption onto Mn^{2+} may involve a slightly larger σ-bonding contribution compared Mn^{3+}.

Included in this work is the use of temperature-programmed desorption to establish an adsorption energy benchmark for CO on single-crystal MnO(100) for comparison to computational results. Also included are DFT calculations for CO adsorption on terrace sites and two common defect sites: step edges, and oxygen vacancy point defects. The experimental benchmarks are particularly useful given the known problems for DFT simulations of systems with highly-correlated electronic system [5].

2.2 MnO(100)

MnO has a rocksalt structure [11] and is an insulator at room temperature [66] with a band gap of 3.6 – 3.8 eV [67, 68]. MnO(100) is used for this study because it is non-polar and thermodynamically stable [13, 69]. A ball model illustration of the ideal MnO(100) surface structure is shown in figure 2-1. Each Mn^{2+} cation and O^{2-} anion in the top atomic layer are five-fold-coordinated with one degree of coordinative unsaturation relative to the bulk. Each Mn^{2+} cation has a d^5, high-spin electronic configuration [70]. As a result, MnO

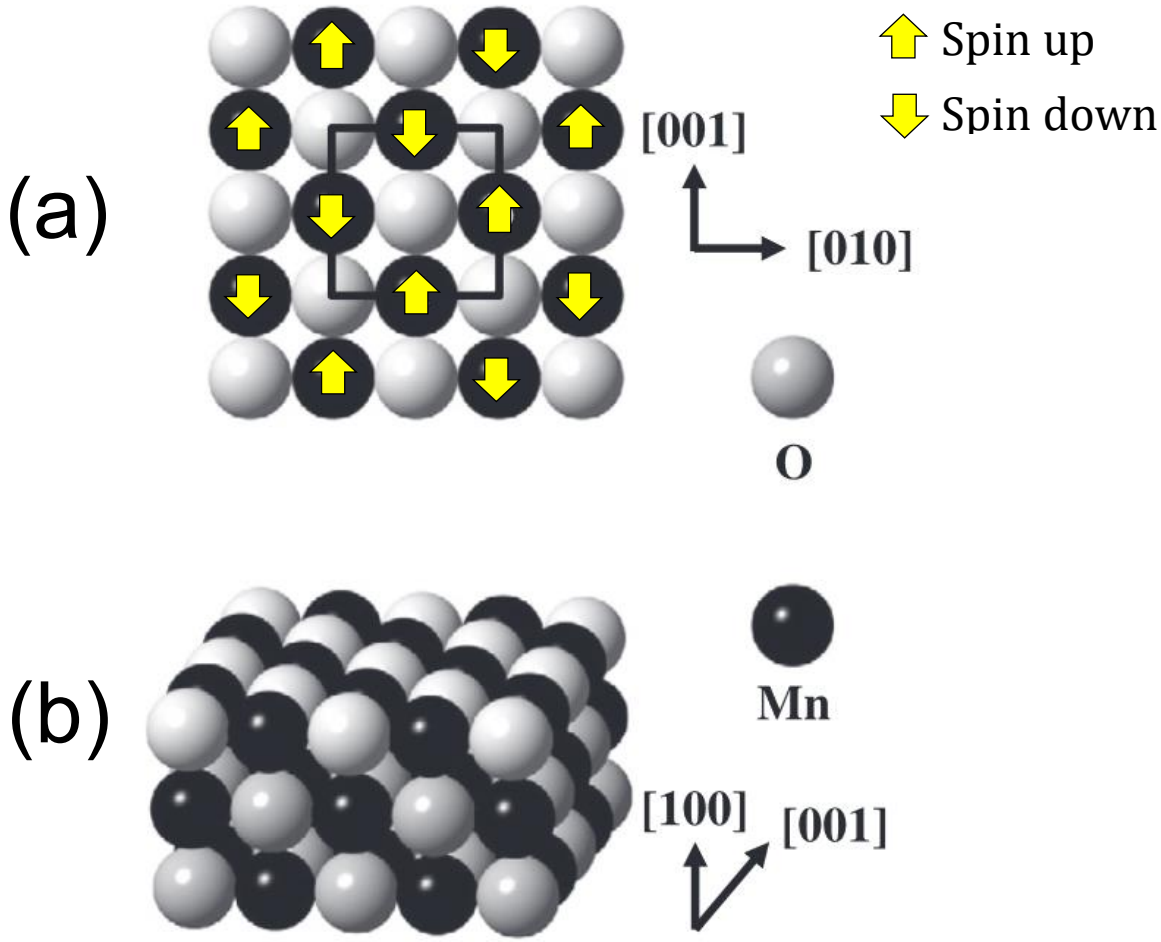

Figure 2-1 Ball model illustration of the ideal stoichiometric MnO(100) surface. (a) Top view of one layer of the MnO(100) surface looking down the [100] surface normal. The lack spheres represent Mn^{2+} cations, white spheres represent O^{2-} cations. A unit cell on the surface of MnO(100) is labeled in black solid lines. The opposing magnetic moments related to (111) planes are illustrated with yellow arrows. (b) Cross-section view along the [001] direction. Adapted from Feng, Cox, (2016).

has a highly-correlated electronic structure. It is anti-ferromagnetic with an AFM-II ordering of the magnetic moments [71]. The arrangement of spin magnetic moments within a (100) plane is shown in figure 2-1 (a), with parallel spins along [011] [9, 71].

2.3 Methods

2.3.1 Experimental Methods

Temperature-programmed desorption (TPD) experiments were conducted in a stainless steel, ion-pumped, ultra-high vacuum system. The sample heating rate was limited to 2.5 K/sec because of the possibility of breakage due to thermal shock of our ceramic MnO(100) sample. The chamber contains an Inficon Quadrex 200 mass spectrometer for TPD experiments, and is equipped with a glass skimmer that covers the ionization zone. The chamber also contains a set of Princeton Research Instruments reverse view low-energy electron diffraction (LEED) optics. A Perkin-Elmer Phi 15-155 single-pass cylindrical mirror analyzer is used for Auger electron spectroscopy to examine surface cleanliness and composition. The chamber has a base pressure of 1×10^{-10} Torr.

The MnO(100) single crystal was purchased from SurfaceNet GmbH with an EPI polish and mounted on a tantalum sample holder connected to a manipulator via liquid-nitrogend-cooled (or LN_2-cooled) copper rods. The sample temperature is measured by a type K thermocouple glued to the back of the sample with Aremco 569 ceramic cement through a hole in the tantalum sample holder. Before TPD experiments, the MnO(100) single-crystal surface is cleaned by bombardment with 2 keV Ar^+ ions. The sample is then heated to 1000 K for 10 min to establish an ordered surface with a (1×1) LEED periodicity.

This procedure yields a clean, ordered, nearly-stoichiometric MnO(100) surface as per previous work [36]. Matheson carbon monoxide (99.997%) was used as received.

2.3.2 Obtaining adsorption energies from TPD

The experimental activation energy of desorption, E_a, can be readily determined from a Redhead analysis [72], and is related to the experimental internal energy of adsorption, ΔE_{ads}, through the following:

$$\Delta H^{\circ}_{ads} = -(E_a + 0.5\, R\, T_p) \quad (1)$$

$$\Delta E_{ads} = \Delta H^{\circ}_{ads} + R\, T_p \quad (2)$$

where ΔH°_{ads} is the adsorption enthalpy, T_p the desorption peak temperature determined from the TPD experiment, and ΔE_{ads} is the adsorption energy. The first equation is derived by assuming an equilibrium between adsorption and desorption rates and a temperature independent prefactor and activation energy for desorption [73]. The second equation accounts for the ideal gas $\Delta(PV)$ contribution to enthalpy [74].

2.3.3 Estimations of desorption prefactors for TPD

It is often assumed [18, 36, 72, 75-77] that a desorption prefactor, ν, of 10^{13} sec^{-1} yields an acceptable value of E_a in a first-order Redhead analysis. In this work, we make use of an empirical entropic scaling relation for terraces [78] along with site-dependent corrections based on considerations from transition state theory for defect sites. Note that we are unable to use a variable heating rate method to determine the prefactor experimentally due to the limited heating rates available to avoid thermal fracture of the sample. For adsorption on flat terraces, Campbell and Sellers [78, 79] introduced a relationship for estimating the prefactor from an empirical linear scaling relation between

the gas-phase entropy of the adsorbate molecules and the adsorbate entropy. It should be noted this relationship is suitable for flat terrace sites, not for defect sites [78].

Transition state theory (TST) can also be used for estimating desorption prefactors for a small molecule like CO [80]. In this work, TST estimates of the variation in prefactor from terrace and defect sites are used as corrections to the empirical prefactor of Campbell and Sellers [81] for desorption from terraces through a simple scaling relationship:

$$\nu_{defect} \approx \frac{\nu_{defect,TST}}{\nu_{terrace,TST}} * \nu_{terrace,S_o} \quad (3)$$

where $\nu_{terrace,S_o}$ is estimated using Campbell and Seller's empirical entropic scaling relation, $\nu_{defect,TST}$ and $\nu_{terrace,TST}$ are desorption prefactors for a defect site and for a flat terrace site, respectively, estimated using transition state theory [80].

In transition state theory, prefactors are represented by equation 4:

$$\nu_{TST} = \frac{q^{\neq}}{q_{ads}} * \frac{k_B T}{h} * \kappa \quad (4)$$

where $q^{\neq}$ is the partition function of the transition state, q_{ads} is the partition function of the adsorbed state, and κ is the transmission coefficient [80]. The transition state for desorption, regardless of the adsorption site, can be approximated as a "2-D gas" from a precursor adsorbed state that translates and rotates freely in a plane parallel to the surface [80]. Therefore, assuming the transmission coefficients are unity and the defect and terrace estimates are made at a constant temperature, the variation in the prefactor between defect and terrace sites is driven primarily by differences in the partition functions of the adsorbed species. Consequently, the prefactor at defect sites can be approximated by equation 5:

$$\nu_{defect} \approx \frac{q_{ads,terrace}}{q_{ads,defect}} * \nu_{terrace,S_o} \quad (5)$$

The partition functions for adsorbed states (q_{ads}) depends on the adsorption site. For a desorption event below 500 K for a simple molecule like CO, the electronic states for the molecules are mostly in the ground-state ($q_{elec} = 1$)[80], and ground state vibrational frequencies can be used for vibrational partition functions (q_{vib}). Compared to adsorption on a flat terrace where translational freedom is allowed in 2-dimensions, a molecule adsorbed onto a step edge is assumed to be free to move only along the step edge and behave like a 1-D gas [82] with the loss of 1 degree of translational freedom compared to the terrace. For a molecule adsorbed onto a point defect, the molecule can be assumed to be translationally "confined in all three dimensions" [81] where all translational degrees of freedom are lost. For a simple molecule adsorbed on the flat terrace site, on the step defect, and at an oxygen vacancy, the adsorbed state partition functions are given by:

$$q_{ads,terrace} = {q_{trans}}^2 * q_{vib} * q_{elec} \quad (6)$$

$$q_{ads,step} = q_{trans} * q_{vib} * q_{elec} \quad (7)$$

$$q_{ads,OV} = q_{vib} * q_{elec} \quad (8)$$

where q_{trans} is the 1-D translational partition function. Most estimates of prefactors for desorption from defects are several orders of magnitude larger than the prefactors for terraces. Campbell and coworkers [78, 82] have described increases as high as a factor of 10^4–10^5 for heavy metal atoms (Pb) with high desorption temperatures along a step edge based on their work on metal adatom desorption from Mo(100). For the lower desorption temperature range of 100 K to 500 K in this study and the smaller mass of CO, q_{trans} is of magnitude 20, leading to significantly smaller correction factors at defects in the present case. Assuming the loss of translational degrees of freedom are the greatest contributing factor to prefactor variations at defects, and that the vibrational partition functions vary

little from site to site, TST estimates of the ratio of $\frac{\nu_{step\ defect,\ TST}}{\nu_{terrace,\ TST}}$ is of order 20, and the ratio of $\frac{\nu_{point\ defect,\ TST}}{\nu_{terrace,\ TST}}$ is of order 400.

2.3.4 DFT Calculations

Density functional theory [1, 2] was used to examine the adsorption chemistry of CO on MnO(100). All of the simulations were performed using the projector-augmented-wave method [83, 84] within the Vienna Ab-initio Simulation Package (VASP) [85-87]. The Perdue-Burke-Ernzerhof (PBE) [88] approximation was used to account for exchange and correlation via a standard generalized gradient approximation (GGA). For calculations on flat terraces, a stoichiometric 256 atom cell was used to provide a slab with a (4×4) surface cell and a thickness of 4 atomic layers along [100]. A 15 Å vacuum gap was introduced after optimization of the bulk structure. All 64 atoms in the bottom layer were frozen in their bulk positions for surface geometry optimization. A 1×3×3 k-point sampling based on the Monkhorst-Pack scheme [89] was used. For all calculations, the initial magnetic moments of Mn^{2+} cations were configured to follow the AFM-II antiferromagnetic arrangement in bulk MnO, verified by powder neutron diffraction [71] and also found to be the ground-state magnetic ordering for DFT within the GGA [90]. A cut-off energy of 400 eV was used for all calculations. For geometric relaxations, forces were minimized to less than 0.01 eV/Å. For dynamical matrix calculations [91, 92] used to estimate vibrational frequencies of adsorbate and free gas molecules, forces are less than 5×10^{-4} eV/Å.

The PBE+U using the method of Dudarev [93] was used to also provide another estimate of the adsorption energy because of the highly correlated electronic structure of MnO. A U-J value of 4.0 eV yields the best energy of formation for bulk MnO [90], and is

used in all calculations. In addition, a range of van der Waals (vdW) dispersion corrections were used, including the DFT-D2 method of Grimme [94], DFT-D3 method of Grimme [95], DFT-D3 Becke-Johnson [96], Tkatchenko-Scheffler method [97], Tkatchenko-Scheffler method with iterative Hirshfeld partitioning [98] and dDsC [99, 100].

Calculations involving a single-atomic step defect and an oxygen vacancy point defect were also conducted. The step defect was created by removing half of the atoms in the top atomic layer to produce a step that runs along [010]. An oxygen vacancy defect was created by removing one top-layer lattice oxygen atom. Both types of defective surfaces were geometry-optimized prior to the examination of CO adsorption.

The energies obtained in the simulations are used to determine the ground state adsorption energies. The ground state adsorption energy is defined as the difference between the internal energy of the adsorbed state (E_{ads}), where a molecule is adsorbed on the surface, and the internal energy of the initial state, where the internal energy of a gas molecule (E_{gas}) and the clean surface ($E_{surface}$) are calculated separately. In all cases, the surface energy is determined following geometric relaxation to find the minimum energy clean surface structure. Equation 9 below defines the adsorption energy, ΔE_{ads} [78]. Zero point energy corrections, ΔZPE, are determined from the vibrational frequencies within the harmonic oscillator approximation, and are obtained via a dynamical matrix calculations [91, 92] in VASP:

$$\Delta E_{ads} = E_{ads} - \left(E_{gas} + E_{surface}\right) + \Delta ZPE \qquad (9)$$

where the ΔZPE is calculated per equation 10 [101]:

$$\Delta ZPE \approx \sum_i \frac{h\,v_i^{ads}}{2} - \sum_i \frac{h\,v_i^{gas}}{2} \qquad (10)$$

where h is the Plank's constant and ν_i^{ads} and ν_i^{gas} are the frequencies of the vibrational modes of the molecules in the adsorbed state and in the free-molecule initial state.

2.4 Results and Discussion

2.4.1. TPD experimental results

2.4.1.1. Experimental adsorption energy for CO on MnO(100)

For each TPD experiment, the sample was cooled to 85 K, followed by the dose, and then heated at 2.5 K/s up to a temperature of 770 K. Desorption signals were monitored by a mass spectrometer. TPD traces for CO desorption from MnO(100) following doses of 0.06 L (1 L ≡ 1×10^{-6} Torr-sec), 0.08 L and 0.11 L are shown in figure 2-2 (a). At these low dosing levels, the MnO(100) surface is sparsely populated with CO molecules to minimize repulsive CO to CO (dipole-dipole) lateral interactions. A consistent peak desorption temperature at 130 K is observed in each TPD trace as the coverage varies, indicating a first-order desorption process at this temperature [72]. This main desorption feature increases in intensity with increasing dose. Trailing this main desorption feature is a gradually diminishing desorption tail that extends into the high-temperature range up to about 400 K. This trend is consistent among all three desorption traces.

Figure 2-2(b) shows TPD traces for higher initial coverages formed by doses up to about 30 L. The figure shows a decreasing desorption peak temperature from 130 K to 100 K due to lateral repulsive CO interactions [53, 54] as dose (and coverage) increases. Similar features are observed on other rocksalt (100) surfaces like CaO(100) [35], MgO(100) and NiO(100) [18]. Note that in figure 2-2(b), the desorption peaks at higher coverage begin in close proximity to the adsorption temperature of 85 K, well above the 30 K desorption temperature for multilayer CO. Hence, CO multilayers are not observed at large doses.

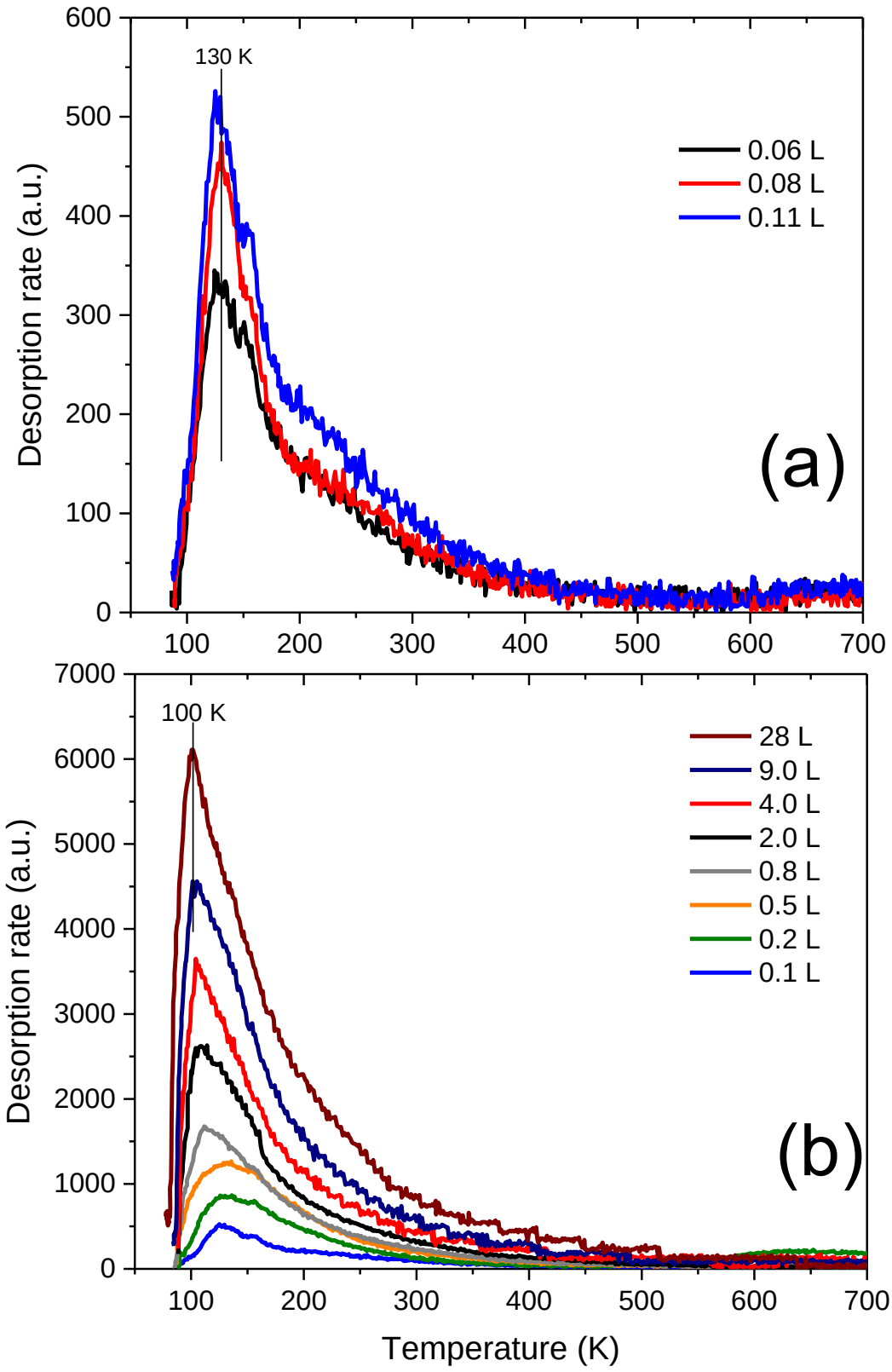

Figure 2-2 (a) The TPD plot of three low dosage of CO desorption from MnO(100). The exposure is 0.06 Langmuir, 0.08 Langmuir, and 0.11 Langmuir. (insert high coverage desorption data). (b) TPD spectra of the higher doses with their desorption peak temperatures labeled.

The desorption peak at 130 K is attributed to desorption from terrace sites and the high-temperature tail to desorption from surface defect sites. The activation energy of desorption from a first-order Redhead analysis [72] is 36.0 $\pm$ 1.7 kJ/mol using a desorption prefactor of 1.9×10^{14} sec^{-1} determined from Campbell and Sellers' empirical entropic scaling relations [78]. The corresponding experimental adsorption energy is -35.6 $\pm$ 2.1 kJ/mol. For comparison, an assumed desorption prefactor of 10^{13} sec^{-1}, gives an activation energy of desorption from flat terraces of 32.9 $\pm$ 1.4 kJ/mol, and a corresponding adsorption energy of -32.4 $\pm$ 1.3 kJ/mol, with both values within the error of our measurements. The magnitude of the adsorption energy at flat terrace sites suggests primarily a non-bonded (physisorption) interaction between CO and MnO(100). It should be noted here that the experimentally obtained adsorption energy is much smaller than the -161 kJ/mol value determined from the ASED cluster model [56]. Activation energies of desorption of CO from other rocksalt oxide terrace sites are also small [78]. For example, on the NiO(100) surface, CO has an activation energy of desorption of 28.0 kJ/mol [18]. The activation energy for CO desorption from MgO(100) is even smaller at 20 kJ/mol in the low-coverage limit [21]. The appearance of a high-temperature tail is also observed on MgO(100), and is similarly attributed to desorption from surface defect sites [21].

2.4.1.2. Desorption order

The constant desorption peak temperature at low coverages indicates a first-order desorption process [102] near 130 K, but the high-temperature tail is not characteristic of a 1st-order desorption process with a constant activation energy. Using the method of Jong and Niemantsverdriet [102], an order plot for CO desorption from MnO(100) was generated (figure 2-3). The method consists of generating desorption isotherms by fitting

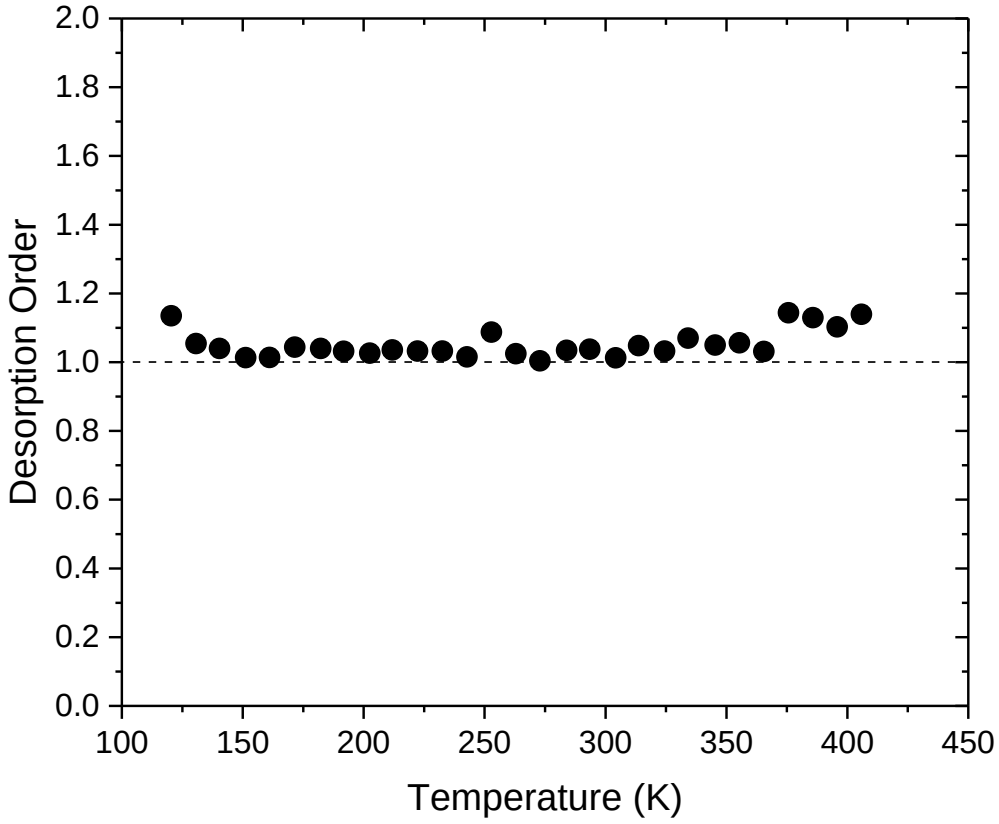

Figure 2-3 The aggregated order plot of CO desorption from MnO(100) surface, in the temperature range of 100 to 300 Kelvin, where the desorption rate signal was the most pronounced.

TPD data from different initial coverages to a linearized desorption rate equation (see Supplemental Material). The temperature range selected for this analysis corresponds to the temperature range where the desorption signal is the most pronounced, and covers not only the primary desorption peak temperature at 130 K, but also the high-temperature tail. As shown in figure 2-3, the order of desorption for CO from the MnO(100) surface is consistently near unity throughout the full temperature range.

2.4.1.3. Coverage vs. Dose

Figure 2-4 (a) shows the coverage vs. dose relationship, with coverage shown via a dual y-axis in both the integrated area obtained from TPD traces, and their corresponding CO upper limit coverage in monolayers (see discussion below). Initially, the coverage increases sharply with respect to the dose, but the rate of increase falls quickly as the dose increases beyond several Langmuirs. An expanded look at the 0 – 0.2 L dose range in figure 2-4 (b) indicates an initial proportionality in uptake vs dose. The coverage eventually rolls over with increasing dose, and plateaus for doses greater than about 20 L.

An upper limit estimate of the CO coverage as a function of dose can be made using the kinetic theory of gases [103] to estimate the number of adsorbate collisions with the surface for a given dose and assuming a unity sticking coefficient in the initial linear coverage growth region. Defining one monolayer as one CO molecule per surface Mn^{2+} site leads to an upper limit estimate of CO coverage displayed on the right-hand vertical axis. At the dosing temperature of 85 K, MnO(100) has an upper limit CO coverage of about 0.4 monolayers. We note that for the highest doses shown in figure 2-3, desorption occurs immediately upon heating hence higher coverages might be possible at lower dosing

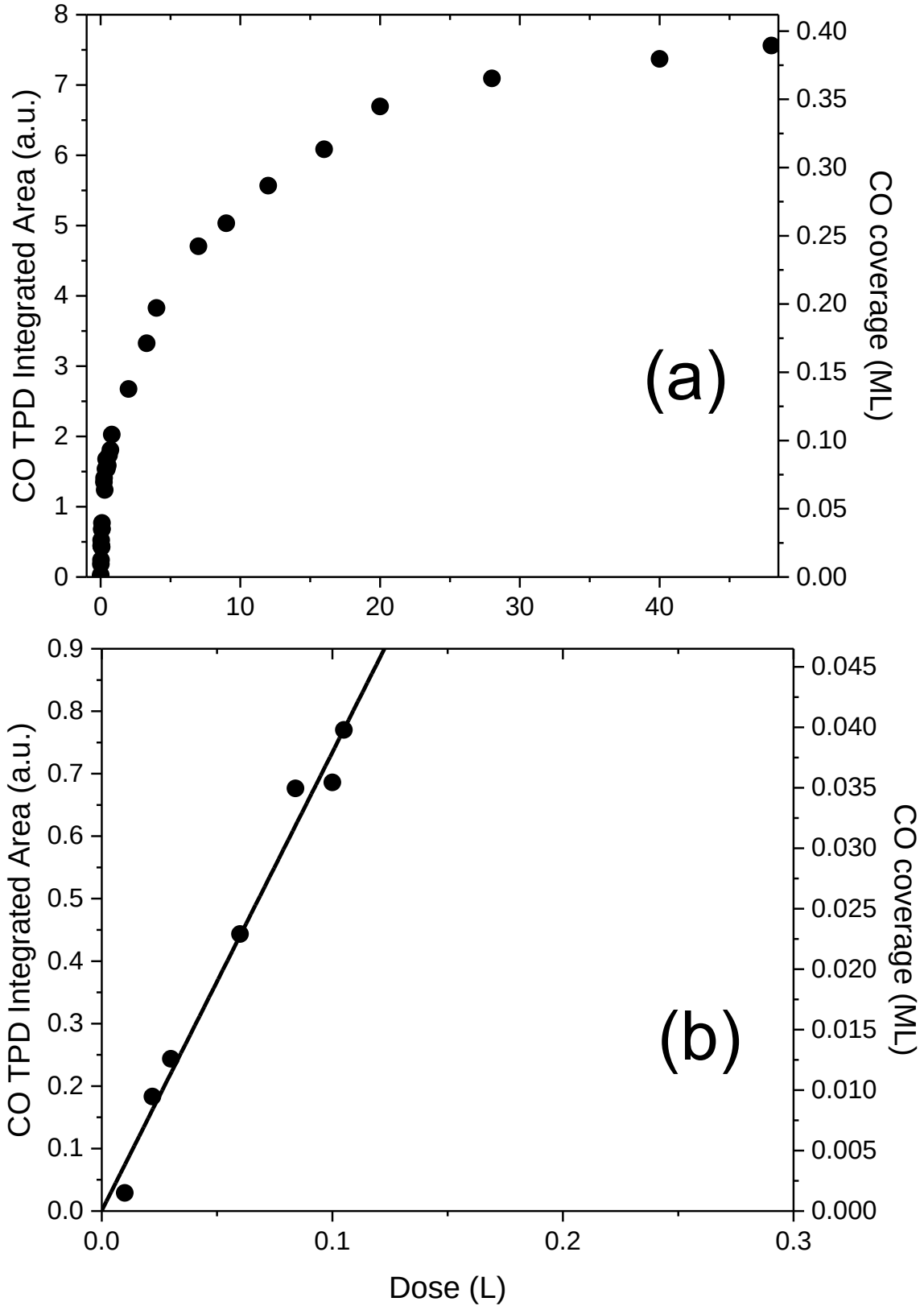

Figure 2-4 (a) The upper limit estimation of CO coverage vs. dose plot on MnO(100). (b) The zoomed-in view at 0.0 – 0.2 L with a linear fit depicted in orange line.

temperatures. The plateauing is due to the repulsive dipole-dipole interactions between adsorbate CO molecules, which is also observed on the CaO(100) rocksalt surface [35].

2.4.1.4. Defect Density

Further TPD experiments were conducted to determine the desorption peak temperatures of CO from surface defect sites. For these additional experiments, the sample is dosed at 85 K, then heated slowly to 130 K and held until the chamber pressure goes through a maximum to remove the primary desorption feature attributed to CO desorption from terrace sites at 130 K. The sample is then cooled back to 85 K to begin a TPD run. Figure 2-5 shows the TPD trace that results from a 0.11 L CO dose, compared to one where the 130 K desorption feature attributed to terrace sites has been removed.

The resulting TPD trace shows a desorption feature with a maximum at 185 K that tails to higher temperatures up to about 300 K. This "defect" TPD trace is attributed to CO desorption from features other than flat terraces. The defect desorption feature at 185 K shows no variance in temperature with respect to initial coverages and can be attributed to a first-order desorption process. Figure 2-6 shows the equivalent defect "coverage" as a function of dose. The coverage rolls over as dose increases, plateauing at an equivalent coverage of about 8% of a monolayer of defect sites (i.e., approximately 20% of the saturation CO coverage.).

2.4.2. DFT simulations

To better understand the CO adsorption behavior from MnO(100), DFT simulations of CO on a terrace, step defect, and at an oxygen vacancy point defect were conducted using

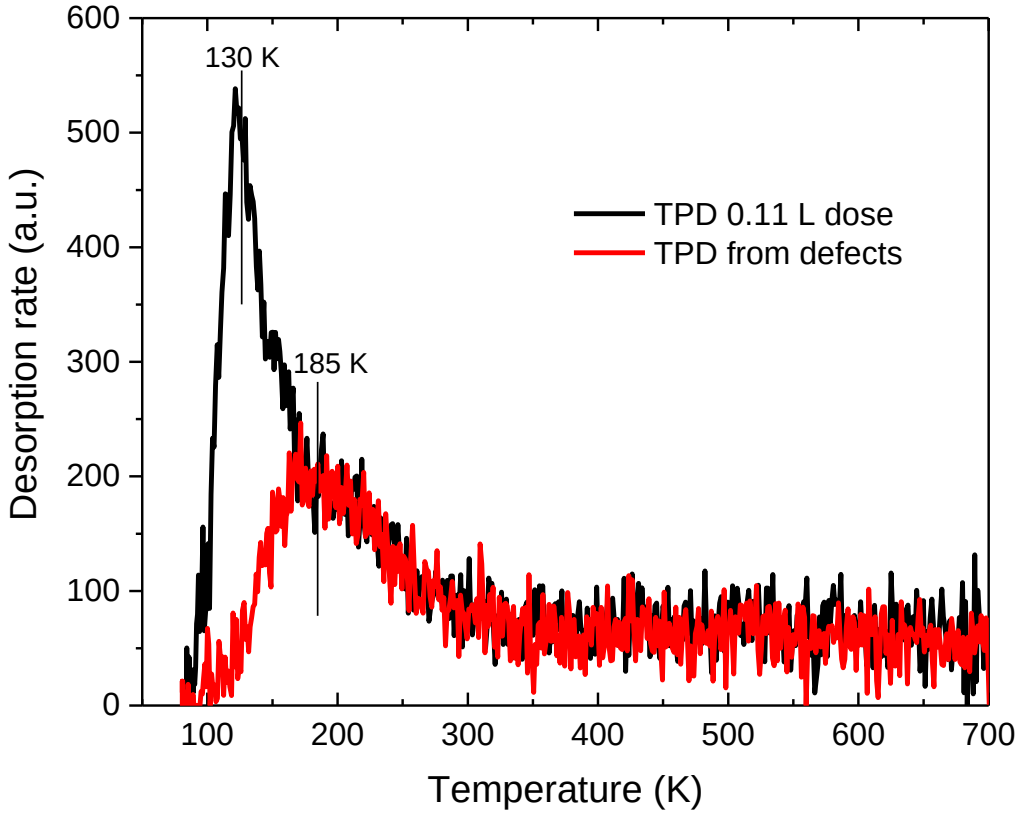

Figure 2-5 The TPD plot of 0.11 L initial dose of a standard TPD (blue), and the TPD plot of a defect TPD of 0.11 L initial dose (orange).

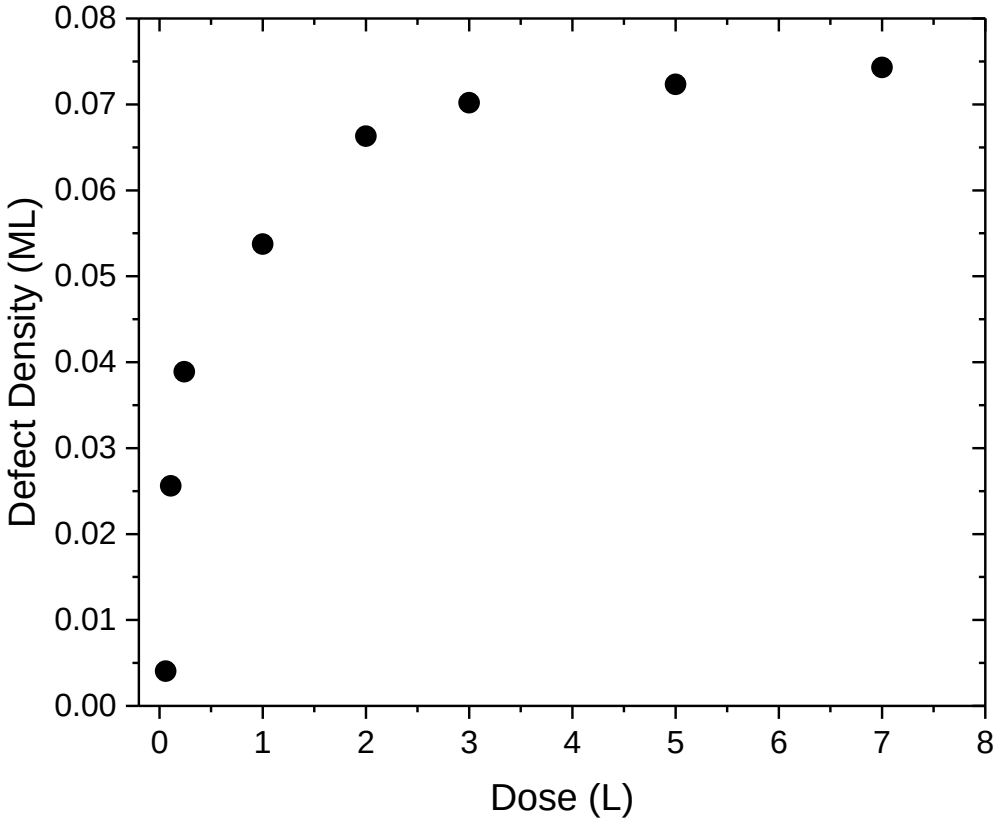

Figure 2-6 The upper limit estimation of CO coverage vs. dose plot on MnO(100) surface defect sites.

PBE and PBE+U to calculate the adsorption energies. Also, various van der Waals corrections are examined to determine their impact on the adsorption energies.

2.4.2.1. DFT Simulations of CO on a MnO(100) terrace

For a simulated CO molecule on a MnO(100) terrace using the PBE functional (Figure 2-7a), an adsorption energy of -32.6 kJ/mol is obtained, compared to the experimental adsorption energy of -35.6 kJ/mol. Geometry optimization of the clean surface to find the minimum energy configuration yields a simple bulk-like termination with no surface reconstruction. The simulation gives a tilted CO that adsorbs carbon-down on a surface Mn cation, but also gives rise to a (2×2) surface reconstruction of the top atomic layer. Given that the low values of the experimental and computed adsorption energies are characteristic of a physisorption (non-bonded) interaction, it seems unlikely that the weak adsorption of CO should drive a surface reconstruction. Because of the insulating nature of MnO and the low (130 K) desorption temperature of CO from terrace sites, the structure cannot readily be examined experimentally with LEED. We note, however, that PBE simulations of Na adatoms on MnO(100) predict a similar reconstruction that is not observed experimentally [36]. Examining the adsorption process with PBE in the absence of a surface reconstruction (i.e., with the atoms in the MnO slab frozen in their clean surface positions) gives an adsorption energy of -26.5 kJ/mol with a CO geometry atop a Mn site and perpendicular to the surface plane (not shown).

Given the unpaired d electrons associated with the Mn cations in MnO, PBE+U simulations were employed to help account for the highly correlated electronic structure. The simulations yield an adsorption energy of -16.7 kJ/mol, lower than either simulation

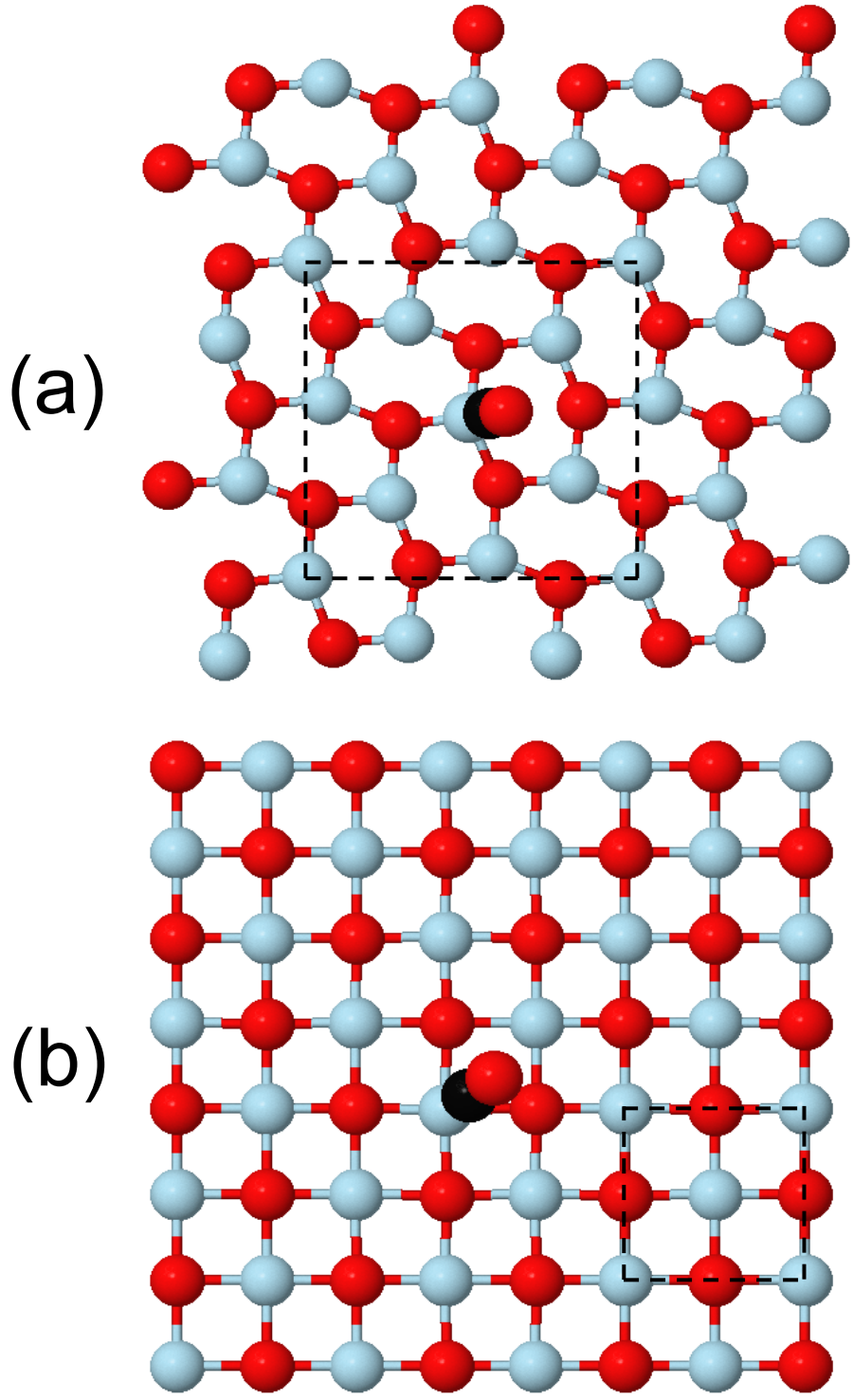

Figure 2-7 (a) A top view of the surface reconstruction caused by the adsorption of a CO molecule on the MnO(100) surface using the PBE functional alone. Only the top layer of MnO(100) is shown. The (2×2) reconstruction pattern is shown with dashed lines. (b) A top view of the surface with CO adsorption using PBE+U as the method. A surface unit cell is labeled in dashed lines. No surface reconstruction is observed when PBE+U is used.

with PBE alone, and with a greater deviation from the experimental adsorption energy of -35.6 kJ/mol. The predicted structure is shown in Figure 2-7(b); no reconstruction of the top atomic layer is predicted with PBE+U. Hence, the +U simulation seems to give a more reasonable accounting of the structure but a poorer description of the energetics.

The adsorption geometry in figure 2-7(b) is shown in a side view in figure 2-8. CO adsorbs carbon-down onto Mn^{2+} with a Mn-C bond length of 2.40 Å, and a CO bond length of 1.15 Å (compared to a free CO bond length of 1.21 Å). CO exhibits a tilt with the Mn-C bond deviating about 17 degrees from the surface normal, while the C-O bond deviates about 40 degrees from the surface normal. The Mn-C angle varies by $\pm$ 4° with various vdW corrections.

An experimental study of CO on NiO(100) reports a Ni-C bond deviating 7 degrees from the surface normal, and a C-O bond tilt of 12 degrees [55]. A computational study with DFT+U also reported the tilt of CO on NiO(100) [52]. In that case, CO adsorbs carbon-down onto Ni^{2+}, with DFT+U giving a Ni-C bond that tilts by about 5° away from the surface normal. The authors argued that the Ni-C bond tilting is attributed to an "increased exchange-splitting of the Ni-d states, which largely suppresses the $2\pi^*$-(d_{zx}+d_{zy}) interaction and enables a 1π-d_{z2} hybridization favoring the tilting geometry" as the result of the addition of +U [52]. We see a similar effects on MnO(100): when only PBE is used and the surface reconstruction is suppressed by freezing the substrate atoms in the slab, the Mn-C bond is parallel to the (100) surface normal, whereas in PBE+U the Mn-C bond deviates 17 degrees from the (100) surface normal. The deviation in our +U simulation can be explained by the same effect, given that $3d^5$ and $3d^8$ electronic configurations of Mn^{2+}

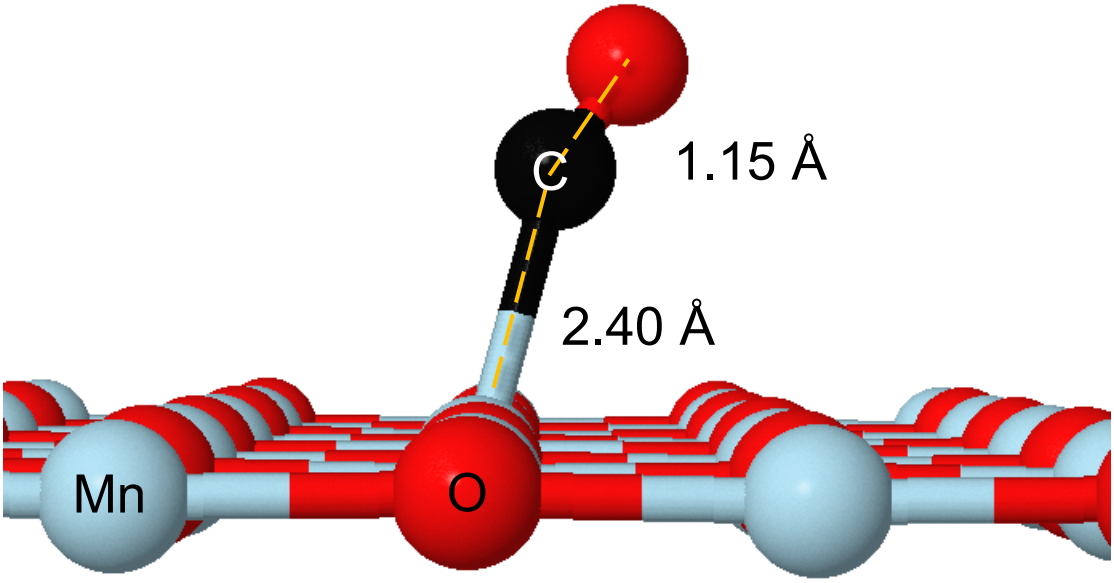

Figure 2-8 The side view of the adsorbed CO on the MnO(100) surface with atoms labeled. The result is obtained using the PBE functional coupled with the +U and DFT-D3 Becke-Johnson. The forces are less than 1×10^{-6} eV/Å. The C-Mn bond length varies by $\pm$ 0.1 Å using various vdW corrections. C-Mn bond tilts away from the surface normal by 17° in figure 8(b).

and Ni^{2+} both possess incompletely-filled d_{z2} orbitals that can hybridize with CO's 1π orbital.

Given that the +U simulation gives a more reasonable structure for this weak adsorption system but underpredicts the adsorption energy, a number of different van der Waals corrections were employed to examine their impact on the predicted adsorption energy. Table 2-1 gives the computed adsorption energy of CO on an MnO(100) terrace in the low coverage limit, with 1 CO per 4×4 surface unit cell. The vdW corrections increase the adsorption energy on average by about 50%, indicating the significant role dispersion forces play in adsorption on terraces. Among these results, PBE+U D3, D3 Becke-Johnson, and dDsC methods give adsorption energies that fall within the $\pm$2.1 kJ/mol experimental error of the measurements. This agreement supports the assignment of the primary experimental desorption feature at 130 K in figure 2-2 (a) to desorption from terrace sites. Overall, the PBE functional with the +U package with a D3-Becke-Johnson dispersion correction provides an excellent prediction (-36.4 kJ/mol), compared to the adsorption energy (-35.6 kJ/mol) obtained experimentally.

Using the structurally and energetically-best case simulation (PBE+U with D3 Becke-Johnson) to examine CO on a Mn^{2+} terrace site gives a stretching frequency of 2087 cm^{-1} compared to a (predicted) gas phase C-O stretching frequency of 2126 cm^{-1}, a decrease of 39 cm^{-1} upon adsorption. Experimentally, the C-O stretching frequency is 2143 cm^{-1} in the gas phase [104] but experiences a blue shift of 47 cm^{-1} upon adsorption onto (presumably) Mn^{2+} sites on a reduced MnO_x powder [65].

2.4.2.2. DFT simulation for CO adsorption on a step defect

The high-temperature tail in the experimental desorption signal is thought to be the result of desorption of CO from defects, so simulations of adsorption on two types of typical defects (steps and oxygen vacancies) has been examined with DFT. The adsorption of CO at a step edge was examined with the PBE+U with D3-Becke-Johnson vdW correction because this combination of methods results in a reasonable structure and an adsorption energy with the smallest deviation from experiment for terrace sites. The structure obtained from the simulation is shown below in figure 2-9. Mn cations and O anions are both four-fold coordinated at the step edge, with one additional degree of coordinative unsaturation compared to a terrace site. CO appears in a bridge-bonded configuration at the step edge on MnO(100). The Mn-C bond length is 2.22 Å, shorter than the Mn-C bond of 2.42 Å on the terrace site. The C-O bond length (oxygen from the step edge) is 1.42 Å, compared to a C-O length of 1.31 Å in a simulated carbonate. Viewing from the side (Figure 2-9 (b)), the CO molecule tilts about 45 degrees with respect to the upper and lower terrace. The predicted adsorption energy is -129.8 kJ/mol, approximately 4 times the calculated adsorption energy on the terrace. The lower (four-fold) coordination of Mn^{2+} and O^{2-} at the step site likely contribute to the rise in adsorption energy and the bridging configuration. A rise in adsorption energy due to under-coordination was also observed with a cluster model study of CO adsorption on MgO(100) [105].

2.4.2.3. DFT simulation of adsorbed CO at an oxygen vacancy

Figure 2-10 shows the predicted structure of CO adsorbed at an oxygen vacancy point defect, again using PBE+U with DFT-D3 Becke-Johnson vdW correction. The CO molecule adsorbs into the vacancy via C where each neighboring Mn^{2+} at the vacancy is initially 4-fold coordinated in the top atomic layer and 5-fold coordinated in the second

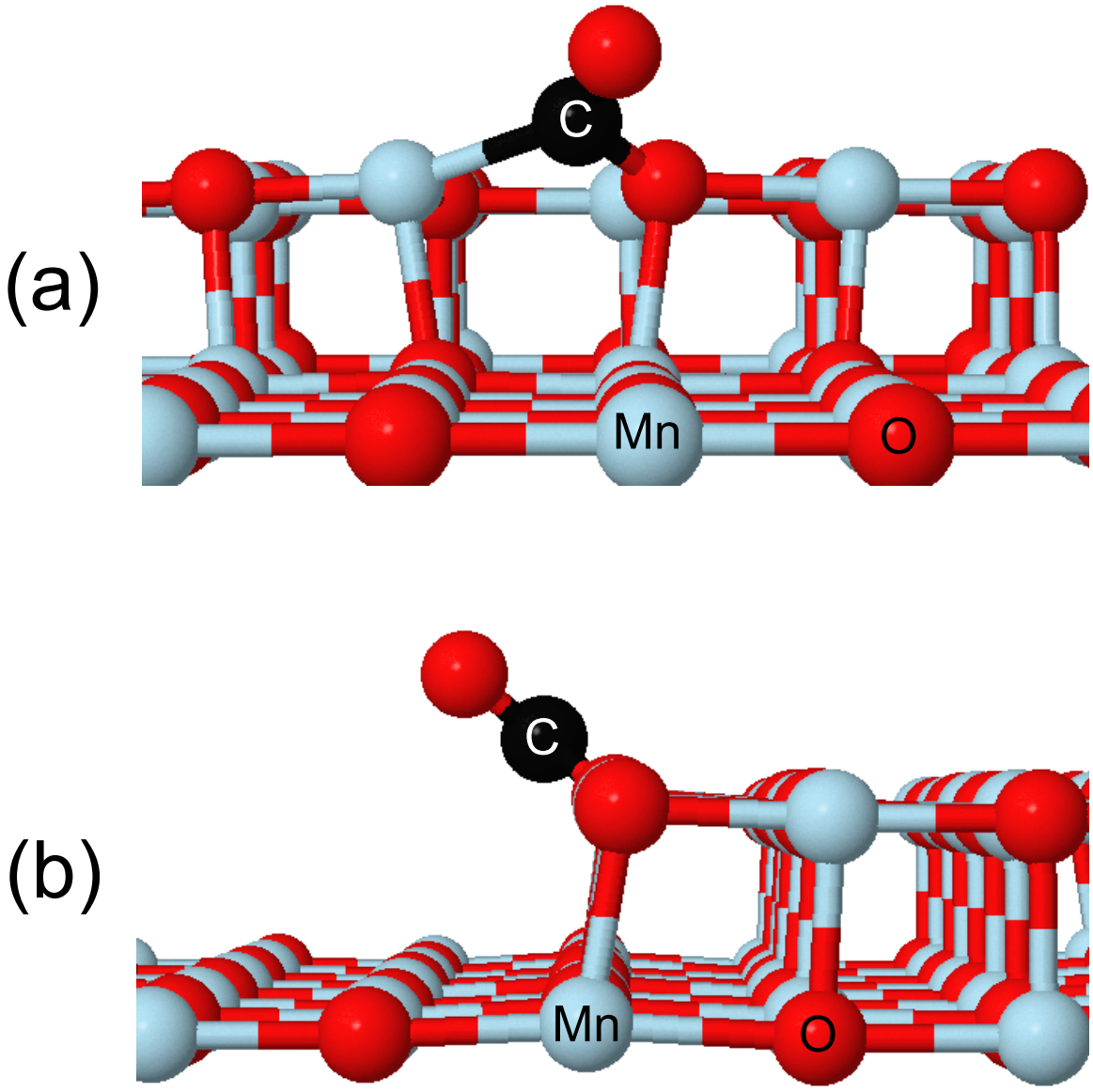

Figure 2-9 The adsorption of CO at the step edge of MnO(100). Only top three layers of MnO(100) are shown. (a) front view (b) side view.

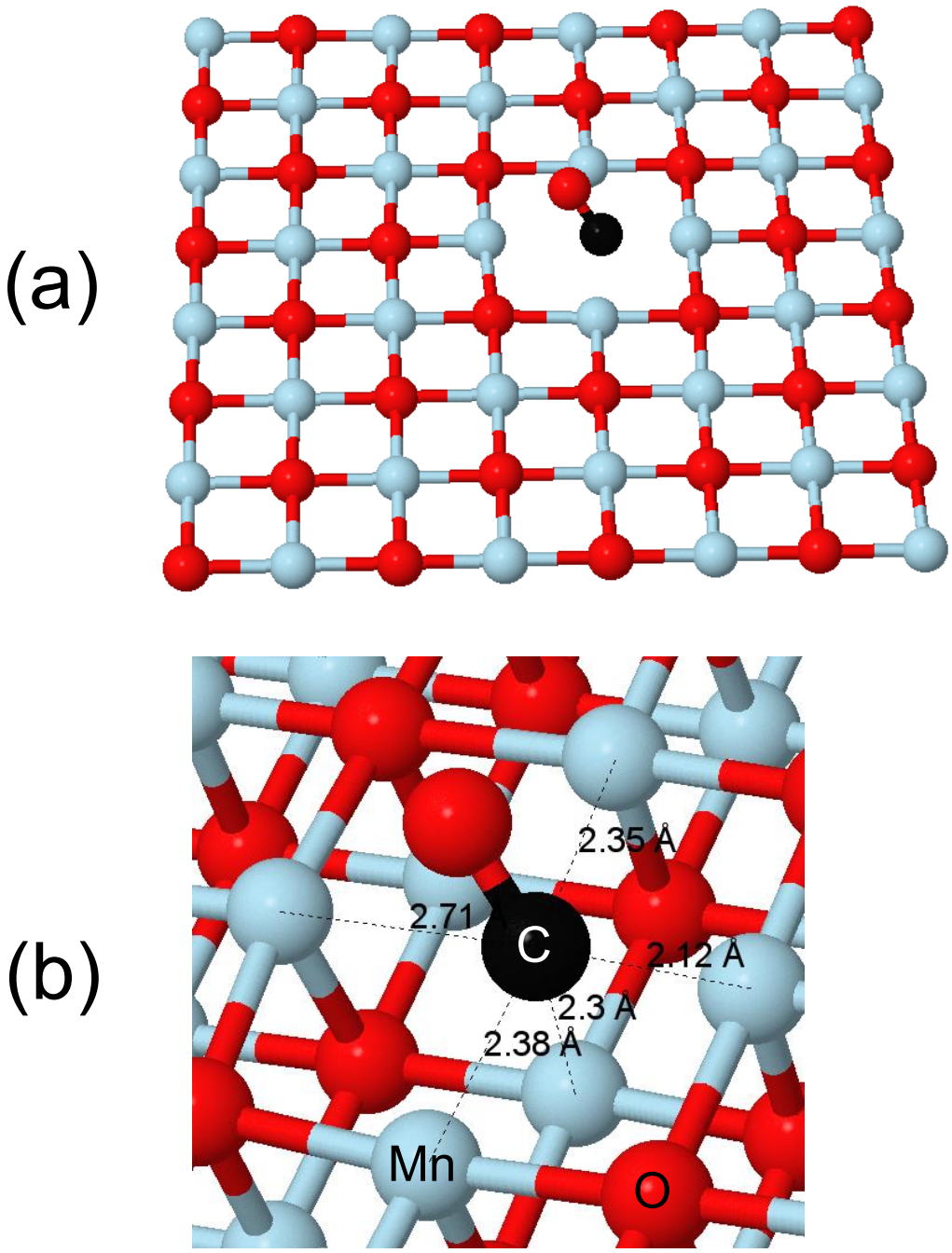

Figure 2-10 (a) CO adsorption at an oxygen vacancy point defect. Only the first layer of MnO(100) is shown. (b) The close-up view of the CO adsorption including second layer atoms with various distances between atoms labeled.

atomic layer. The adsorbed CO molecule tilts in the defect along the diagonal surface lattice direction. The C-O bond length of the adsorbed molecule is 1.32 Å, longer than the 1.15 Å predicted on the terrace. The average distance between carbon and an adjacent Mn atoms is 2.39 Å, shorter than the Mn-C bond length of 2.42 Å on the terrace. The adsorption energy in this case is -108.2 kJ/mol, much larger than found on a terrace site (-36.4 kJ/mol). The decrease in coordination number of the four top-layer Mn^{2+} cations at the vacancy results in stronger binding to CO, and results in the increase in adsorption energy. The carbon atom in this case is 6-fold-coordinated (5 surrounding Mn^{2+} cations and 1 oxygen from the CO molecule), compared to 2-fold-coordinated on a terrace site.

2.4.3. DFT prediction of desorption temperatures from defects

The DFT adsorption energies for CO at a step and oxygen vacancy are -129.8 kJ/mol and -108.2 kJ/mol (using PBE+U and D3-Becke Johnson), respectively, in the low coverage limit. Using equation 3, prefactors for CO desorption from these two sites are estimated as 2×10^{17} s^{-1} and 2×10^{19} s^{-1}, respectively (see supplemental material). These large desorption prefactors stem from entropic gains from the confined adsorbed state at a defect compared to a terrace [81]. Based on these prefactors, the peak desorption temperatures for first-order desorption from these two defects are estimated to be 295 K at an oxygen vacancy and 385 K at a step. These estimates are shown in comparison to the experimental data in Figure 2-11.

As figure 2-11 shows, the peak desorption temperatures predicted by DFT for these two defect sites do not align with the observed 185 K surface defect desorption peak temperature observed experimentally. Several possibilities may explain the lack of agreement with the experimental data. It is possible that the experimental defects are not

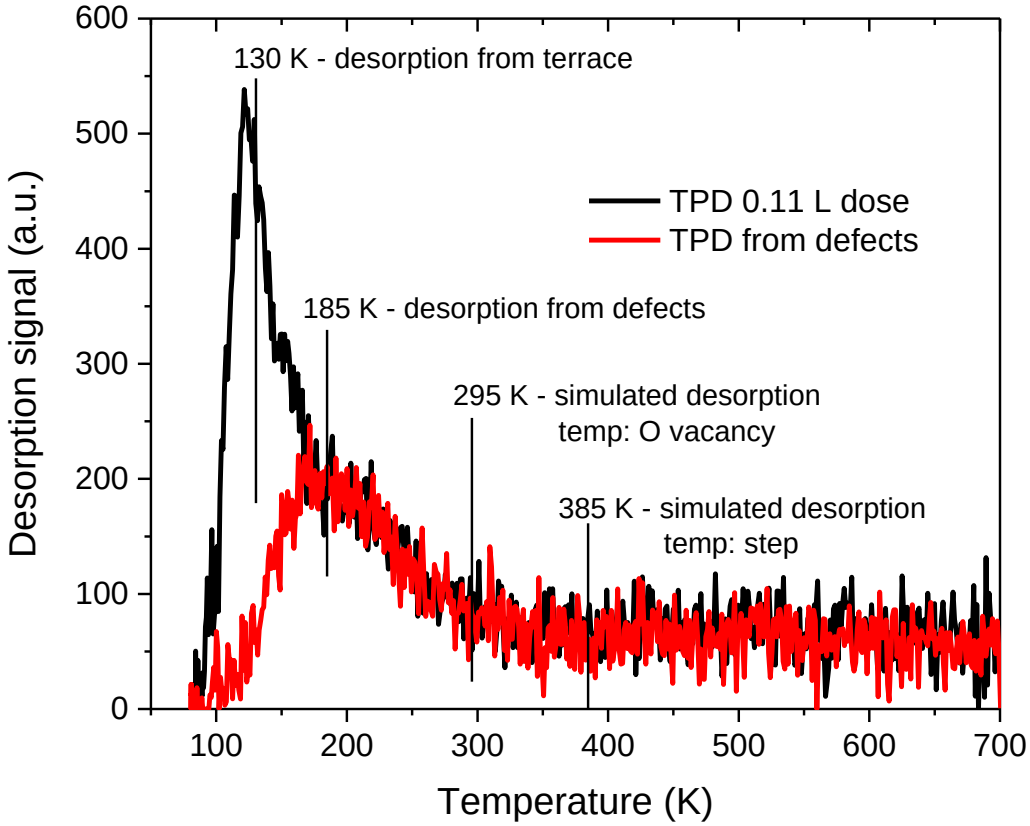

Figure 2-11 The labeled peak desorption temperature for desorption of CO from flat terrace sites, surface defect sites, oxygen point defect vacancy (simulated), and from a step defect site (simulated).

of the simple step or O-vacancy type examined in sections 4.2.2 and 4.2.3. It is also possible that the computational methods do not accurately predict the defect adsorption energies. In particular, the U and J parameters used for the +U simulation (U = 5 eV, J = 1 eV) are optimized based on the bulk heat of formation [90]. They may provide a poor description of the energetics at significantly under-coordinated sites associated with the defects. It is noted that an investigation into an optimal U and J parameter set for surface Mn cations at defects was not conducted.

2.5 Conclusion

A study of CO adsorption on the MnO(100) surface was conducted using TPD and DFT. TPD reveals a primary CO desorption signal at 130 K from MnO(100) in the low coverage limit giving an adsorption energy of -35.6 $\pm$2.1 kJ/mol on terrace sites. PBE+U gives a more reasonable structural result than PBE alone, and the adsorption energy obtained by PBE+U and DFT-D3 Becke-Johnson gives excellent agreement with the experimentally obtained ΔE_{ads} for adsorption at Mn^{2+} terrace sites. The van der Waals dispersion contribution is significant, and accounts for about 50% of the adsorption energy. These simulations suggest a tilted CO adsorption geometry on MnO(100) similar to experimental [55] and computational [52] reports for CO on NiO(100), another transition metal oxide with a highly-correlated electronic structure. PBE+U simulations were less successful in identifying a simple site associated with an experimentally observed desorption feature at 185 K attributed to surface defects.

Acknowledgement

The authors gratefully acknowledge financial support by the Chemical Sciences, Geosciences and Biosciences Division, Office of Basic Energy Sciences, Office of Science, U.S. Department of Energy through Grant DE-FG02-97ER14751. The authors also acknowledge Advanced Research Computing at Virginia Tech for providing computational resources and technical support that have contributed to the results reported within this paper.

2.6 Tables

	Dose *L*	Coverage *ML*	Adsorption energy, E_{ads} *kJ/mol*
TPD trials	0.06-0.11	0.023-0.042	-35.6 ± 2.1
PBE reconstructed (relaxed)		0.031	-31.4
PBE no reconstruction (static)		0.031	-26.5
PBE + U		0.031	-16.7
PBE + U, D2 Grimme		0.031	-31.4
PBE + U, D3 Grimme		0.031	-33.5
PBE + U, D3 Becke-Johnson		0.031	-36.4
PBE + U, TS		0.031	-39.3
PBE + U, TSHP		0.031	-31.4
PBE + U, dDsC		0.031	-33.9

Table 2-1 The comparison between experimentally and computationally obtained adsorption energies of CO on flat terrace sites of MnO(100). The coverages from the TPD experiments are calculated using methods discussed in 2.3, and subtracting the desorption accumulated from the desorption signal tail. The zero point energy corrections have been applied to the calculated adsorption energies. The coverages of 0.02, 0.03 and 0.04 monolayers that corresponds to dosages of 0.06, 0.08, and 0.11 are experimental coverages. All coverages associated with PBE are simulation coverages determined using 1 adsorbate molecule per 4×4 unit cell as basis as figure 2-7 illustrates, assuming only top-layer Mn^{2+} are adsorption sites.

References

[1] W. Kohn, L.J. Sham, Self-consistent equations including exchange and correlation effects, Physical Review, 140 (1965) A1133.

[2] P. Hohenberg, W. Kohn, Inhomogeneous Electron Gas, Physical Review, 136 (1964) B864-B871.

[3] A. Sarmah, Density Functional Theory (DFT): Periodic Advancement and New Challenges, Research Methodology in Chemical Sciences: Experimental and Theoretical Approach, (2017) 219.

[4] C. Franchini, V. Bayer, R. Podloucky, J. Paier, G. Kresse, Density functional theory study of MnO by a hybrid functional approach, Physical Review B, 72 (2005) 045132.

[5] A.J. Cohen, P. Mori-Sánchez, W. Yang, Insights into Current Limitations of Density Functional Theory, Science, 321 (2008) 792-794.

[6] X. Zheng, A.J. Cohen, P. Mori-Sánchez, X. Hu, W. Yang, Improving band gap prediction in density functional theory from molecules to solids, Physical review letters, 107 (2011) 026403.

[7] P. Simons Collaboration on the Many-Electron, M. Motta, D.M. Ceperley, G.K.-L. Chan, J.A. Gomez, E. Gull, S. Guo, C.A. Jiménez-Hoyos, T.N. Lan, J. Li, F. Ma, A.J. Millis, N.V. Prokof'ev, U. Ray, G.E. Scuseria, S. Sorella, E.M. Stoudenmire, Q. Sun, I.S. Tupitsyn, S.R. White, D. Zgid, S. Zhang, Towards the Solution of the Many-Electron Problem in Real Materials: Equation of State of the Hydrogen Chain with State-of-the-Art Many-Body Methods, Physical Review X, 7 (2017) 031059.

[8] E.R. Johnson, A.D. Becke, Communication: DFT treatment of strong correlation in 3d transition-metal diatomics, The Journal of Chemical Physics, 146 (2017) 211105.

[9] C.G. Shull, W.A. Strauser, E.O. Wollan, Neutron Diffraction by Paramagnetic and Antiferromagnetic Substances, Physical Review, 83 (1951) 333-345.

[10] M.E. Lines, E.D. Jones, Antiferromagnetism in the Face-Centered Cubic Lattice. II. Magnetic Properties of MnO, Physical Review, 139 (1965) A1313-A1327.

[11] J. Kolorenč, L. Mitas, structural phase transition in MnO under pressure: Comparison of all-electron and pseudopotential approaches, Physical Review B, 75 (2007) 235118.

[12] V.E. Henrich, P.A. Cox, The Surface Science of Metal Oxides, Cambridge University Press, 1996.

[13] P. Tasker, The stability of ionic crystal surfaces, Journal of Physics C: Solid State Physics, 12 (1979) 4977.

[14] H. Bilz, W. Kress, Phonon Dispersion Relations in Insulators, Springer Science & Business Media, 2012.

[15] J.H. Binks, J.A. Duffy, Chemical bonding in rock salt structured transition metal oxides, Journal of Solid State Chemistry, 87 (1990) 195-201.

[16] J. Heidberg, D. Meine, B. Redlich, CO2 adsorption on the MgO (100) single crystal surface detected by polarization FTIR spectroscopy and SPA-LEED, Journal of Electron Spectroscopy and Related Phenomena, 64 (1993) 599-608.

[17] J. Heidberg, M. Kandel, D. Meine, U. Wildt, The monolayer CO adsorbed on MgO (100) detected by polarization infrared spectroscopy, Surface Science, 331 (1995) 1467-1472.

[18] R. Wichtendahl, M. Rodriguez-Rodrigo, U. Härtel, H. Kuhlenbeck, H.J. Freund, Thermodesorption of CO and NO from Vacuum-Cleaved NiO (100) and MgO (100), Physical Status Solidi A, 173 (1999) 93-100.

[19] S.L. Tait, Z. Dohnálek, C.T. Campbell, B.D. Kay, n-alkanes on MgO (100). I. Coverage-dependent desorption kinetics of n-butane, The Journal of Chemical Physics, 122 (2005) 164707.

[20] M. Stirniman, C. Huang, R. Scott Smith, S. Joyce, B.D. Kay, The adsorption and desorption of water on single crystal MgO (100): The role of surface defects, The Journal of Chemical Physics, 105 (1996) 1295-1298.

[21] Z. Dohnalek, G.A. Kimmel, S.A. Joyce, P. Ayotte, R.S. Smith, B.D. Kay, Physisorption of CO on the MgO (100) Surface, The Journal of Physical Chemistry B, 105 (2001) 3747-3751.

[22] C. Xu, D. Goodman, Structure and geometry of water adsorbed on the MgO (100) surface, Chemical Physics Letters, 265 (1997) 341-346.

[23] K. Jug, B. Heidberg, T. Bredow, Molecular dynamics study of water adsorption structures on the MgO (100) surface, The Journal of Physical Chemistry C, 111 (2007) 6846-6851.

[24] Y. Wang, T.N. Truong, Theoretical study of adsorption of water dimer on the perfect MgO (100) surface: Molecular adsorption versus dissociative chemisorption, The Journal of Physical Chemistry B, 108 (2004) 3289-3294.

[25] Y. Kim, J. Stultz, D. Goodman, Dissociation of water on MgO (100), The Journal of Physical Chemistry B, 106 (2002) 1515-1517.

[26] S. Imad-Uddin Ahmed, S.S. Perry, O. El-Bjeirami, Desorption and reaction of water on MgO (100) studied as a function of surface preparation, The Journal of Physical Chemistry B, 104 (2000) 3343-3348.

[27] J. Günster, G. Liu, J. Stultz, S. Krischok, D. Goodman, Water and methanol adsorption on MgO (100)/Mo (100) studied by electron spectroscopies and thermal programmed desorption, The Journal of Physical Chemistry B, 104 (2000) 5738-5743.

[28] J. Suzanne, V. Panella, D. Ferry, M. Sidoumou, The structure of CO2 monolayers on MgO (100) single crystal surfaces, Surface Science, 293 (1993) L912-L916.

[29] J. Heidberg, D. Meine, Polarized infrared spectra of CO2 adsorbed on the MgO (100) single crystal surface, Surface Science Letters, 279 (1992) L175-L179.

[30] A. Chakradhar, U. Burghaus, Carbon dioxide adsorption on MgO (001)–CO2 kinetics and dynamics, Surface Science, 616 (2013) 171-177.

[31] G. Pacchioni, Physisorbed and chemisorbed CO2 at surface and step sites of the MgO (100) surface, Surface Science, 281 (1993) 207-219.

[32] D. Meixner, D. Arthur, S. George, Kinetics of desorption, adsorption, and surface diffusion of CO2 on MgO (100), Surface Science, 261 (1992) 141-154.

[33] H. Onishi, C. Egawa, T. Aruga, Y. Iwasawa, Adsorption of Na atoms and oxygen-containing molecules on MgO (100) and (111) surfaces, Surface Science, 191 (1987) 479-491.

[34] G. Pacchioni, J.M. Ricart, F. Illas, Ab initio cluster model calculations on the chemisorption of CO2 and SO2 probe molecules on MgO and CaO (100) surfaces. A theoretical measure of oxide basicity, Journal of the American Chemical Society, 116 (1994) 10152-10158.

[35] E. Kadossov, U. Burghaus, Adsorption kinetics and dynamics of CO, NO, and CO2 on reduced CaO (100), The Journal of Physical Chemistry C, 112 (2008) 7390-7400.

[36] X. Feng, D.F. Cox, Na Deposition on MnO (100), Surface Science, 645 (2016) 23-29.

[37] M. Langell, C. Hutchings, G. Carson, M. Nassir, High resolution electron energy loss spectroscopy of MnO (100) and oxidized MnO (100), Journal of Vacuum Science & Technology A, 14 (1996) 1656-1661.

[38] G. Kugel, C. Carabatos, B. Hennion, B. Prevot, A. Revcolevschi, D. Tocchetti, Lattice dynamics of wustite (FeO), Physical Review B, 16 (1977) 378.

[39] R. Felton, M. Prutton, S. Tear, M. Welton-Cook, A LEED analysis of the CoO (100) surface, Surface Science, 88 (1979) 474-478.

[40] W. Buyers, G. Dolling, J. Sakurai, R. Cowley, Magnetic Excitations in Cobaltous Oxide, in: Neutron Inelastic Scattering Vol. II. Proceedings of a Symposium on Neutron Inelastic Scattering, 1968.

[41] S.M. Vesecky, X. Xu, D.W. Goodman, Infrared study of CO on NiO (100), Journal of Vacuum Science & Technology A: Vacuum, Surfaces, and Films, 12 (1994) 2114-2118.

[42] R. Wichtendahl, M. Rodriguez-Rodrigo, U. Härtel, H. Kuhlenbeck, H.-J. Freund, TDS study of the bonding of CO and NO to vacuum-cleaved NiO (100), Surface Science, 423 (1999) 90-98.

[43] D. Cappus, J. Klinkmann, H. Kuhlenbeck, H.-J. Freund, CO on NiO (100): orientation and bonding, Surface Science, 325 (1995) L421-L427.

[44] M. Kittel, J.T. Hoeft, S. Bao, M. Polcik, R.L. Toomes, J.-H. Kang, D.P. Woodruff, M. Pascal, C.L. Lamont, The local adsorption geometry of CO and NH3 on NiO (1 0 0) determined by scanned-energy mode photoelectron diffraction, Surface Science, 499 (2002) 1-14.

[45] M. Schulze, R. Reissner, Adsorption of water on epitactic NiO (1 0 0), Surface Science, 482 (2001) 285-293.

[46] R. Reissner, M. Schulze, Multilayer adsorption of water on NiO (100) at 120 and 143K, Surface Science, 454 (2000) 183-190.

[47] R. Reissner, U. Radke, M. Schulze, E. Umbach, Water coadsorbed with oxygen and potassium on thin NiO (100) films, Surface Science, 402 (1998) 71-75.

[48] K. Rieder, R. Migoni, B. Renker, Lattice dynamics of strontium oxide, Physical Review B, 12 (1975) 3374.

[49] S. Chang, C. Tompson, E. Gürmen, L. Muhlestein, Lattice dynamics of BaO, Journal of Physics and Chemistry of Solids, 36 (1975) 769-773.

[50] G. Pacchioni, T. Minerva, P.S. Bagus, Chemisorption of CO on defect sites of MgO, Surface Science, 275 (1992) 450-458.

[51] S. Briquez, C. Girardet, J. Goniakowski, C. Noguera, Molecular adsorption on unrelaxed and relaxed ionic steps. Application to Ar, CO, CO_2, and NH_3 adsorbed on MgO (001), The Journal of Chemical Physics, 105 (1996) 678-685.

[52] A. Rohrbach, J. Hafner, G. Kresse, Molecular adsorption on the surface of strongly correlated transition-metal oxides: A case study for CO/NiO (100), Physical Review B, 69 (2004) 075413.

[53] R. Hammaker, S. Francis, R. Eischens, Infrared study of intermolecular interactions for carbon monoxide chemisorbed on platinum, Spectrochimica Acta, 21 (1965) 1295-1309.

[54] P. Deshlahra, J. Conway, E.E. Wolf, W.F. Schneider, Influence of dipole–dipole interactions on coverage-dependent adsorption: CO and NO on Pt (111), Langmuir, 28 (2012) 8408-8417.

[55] J.T. Hoeft, M. Kittel, M. Polcik, S. Bao, R.L. Toomes, J.H. Kang, D.P. Woodruff, M. Pascal, C.L. Lamont, Molecular adsorption bond lengths at metal oxide surfaces: failure of current theoretical methods, Physical Review Letter, 87 (2001) 086101.

[56] V. Allen, W. Jones, P. Pacey, A molecular orbital study of carbon monoxide adsorption on a MnO surface, Surface Science, 199 (1988) 309-319.

[57] V. Iablokov, K. Frey, O. Geszti, N. Kruse, High catalytic activity in CO oxidation over MnO x nanocrystals, Catalysis Letters, 134 (2010) 210-216.

[58] S. Liang, F. Teng, G. Bulgan, R. Zong, Y. Zhu, Effect of phase structure of MnO2 nanorod catalyst on the activity for CO oxidation, The Journal of Physical Chemistry C, 112 (2008) 5307-5315.

[59] S. Imamura, Y. Tsuji, Y. Miyake, T. Ito, Cooperative action of palladium and manganese (III) oxide in the oxidation of carbon monoxide, Journal of Catalysis, 151 (1995) 279-284.

[60] A.C. Gluhoi, S.D. Lin, B.E. Nieuwenhuys, The beneficial effect of the addition of base metal oxides to gold catalysts on reactions relevant to air pollution abatement, Catalysis Today, 90 (2004) 175-181.

[61] K. Ramesh, L. Chen, F. Chen, Y. Liu, Z. Wang, Y.-F. Han, Re-investigating the CO oxidation mechanism over unsupported MnO, Mn2O3 and MnO2 catalysts, Catalysis Today, 131 (2008) 477-482.

[62] S. Royer, D. Duprez, Catalytic oxidation of carbon monoxide over transition metal oxides, ChemCatChem, 3 (2011) 24-65.

[63] M. Kantcheva, M.U. Kucukkal, S. Suzer, Spectroscopic investigation of species arising from CO chemisorption on titania-supported manganese, Journal of Catalysis, 190 (2000) 144-156.

[64] P. Angevaare, J. Aarden, J. Linn, A. Zuur, V. Ponec, Infrared spectroscopic characterization of the α-Mn3O4 surface by adsorption of carbon monoxide, Journal of Electron Spectroscopy and Related Phenomena, 54 (1990) 795-804.

[65] R. Craciun, B. Nentwick, K. Hadjiivanov, H. Knözinger, Structure and redox properties of MnOx/Yttrium-stabilized zirconia (YSZ) catalyst and its used in CO and CH4 oxidation, Applied Catalysis A: General, 243 (2003) 67-79.

[66] J.R.A. Patterson, C. M.; Jackson, D. D.; Weir, S. T.; Baker, P. A.; Vohra, Y. K., Electrical Resistance Measurements on the Mott Insulator MnO at Megabar Pressures, American Physical Society, (2004).

[67] D.R. Huffman, R. Wild, M. Shinmei, Optical Absorption Spectra of Crystal‐Field Transitions in MnO, The Journal of Chemical Physics, 50 (1969) 4092-4094.

[68] V.I. Anisimov, M. Korotin, E. Kurmaev, Band-structure description of mott insulators (NiO, MnO, FeO, CoO), Journal of Physics: Condensed Matter, 2 (1990) 3973.

[69] J. Wu, J. Cao, W.-Q. Han, A. Janotti, H.-C. Kim, Functional metal oxide nanostructures, Springer Science & Business Media, 2011.

[70] J. Van Elp, R. Potze, H. Eskes, R. Berger, G. Sawatzky, Electronic structure of MnO, Physical Review B, 44 (1991) 1530.

[71] W. Roth, Magnetic structures of MnO, FeO, CoO, and NiO, Physical Review, 110 (1958) 1333.

[72] P.A. Redhead, Thermal Desorption of Gases, Vacuum, (1962) 9.

[73] W. Brown, R. Kose, D. King, Femtomole adsorption calorimetry on single-crystal surfaces, Chemical Reviews, 98 (1998) 797-832.

[74] J. Wellendorff, T.L. Silbaugh, D. Garcia-Pintos, J.K. Nørskov, T. Bligaard, F. Studt, C.T. Campbell, A benchmark database for adsorption bond energies to transition metal surfaces and comparison to selected DFT functionals, Surface Science, 640 (2015) 36-44.

[75] J.D. Brooks, Q. Ma, D.F. Cox, Reactions of ethyl groups on a model chromia surface: Ethyl chloride on stoichiometric α-Cr_2O_3 (101¯2), Surface Science, 603 (2009) 523-528.

[76] S. Haydar, C. Moreno-Castilla, M. Ferro-Garcıa, F. Carrasco-Marın, J. Rivera-Utrilla, A. Perrard, J. Joly, Regularities in the temperature-programmed desorption spectra of CO2 and CO from activated carbons, Carbon, 38 (2000) 1297-1308.

[77] Z. Liang, T. Li, M. Kim, A. Asthagiri, J.F. Weaver, Low-temperature activation of methane on the IrO_2 (110) surface, Science, 356 (2017) 299-303.

[78] C.T. Campbell, J.R.V. Sellers, Enthalpies and Entropies of Adsorption on Well-Defined Oxide Surfaces: Experimental Measurements, Chemical Reviews, 113 (2013) 4106-4135.

[79] C. T. Campbell, J. Sellers, Correction to Enthalpies and Entropies of Adsorption on Well-Defined Oxide Surfaces: Experimental Measurements, 2017.

[80] J. Fair, R.J. Madix, Low and high coverage determinations of the rate of carbon monoxide adsorption and desorption from Pt (110), The Journal of Chemical Physics, 73 (1980) 3480-3485.

[81] C. Rettner, D. Bethune, E. Schweizer, Measurement of Xe desorption rates from Pt (111): Rates for an ideal surface and in the defect-dominated regime, The Journal of Chemical Physics, 92 (1990) 1442-1457.

[82] D.E. Starr, C.T. Campbell, Large entropy difference between terrace and step sites on surfaces, Journal of the American Chemical Society, 130 (2008) 7321-7327.

[83] P.E. Blöchl, Projector augmented-wave method, Physical Review B, 50 (1994) 17953-17979.

[84] G. Kresse, D. Joubert, From ultrasoft pseudopotentials to the projector augmented-wave method, Physical Review B, 59 (1999) 1758-1775.

[85] G. Kresse, Comput. Mater. Sci., 6 (1996) 15.

[86] G. Kresse, J. Furthmüller, Efficient iterative schemes for ab initio total-energy calculations using a plane-wave basis set, Physical Review B, 54 (1996) 11169.

[87] G. Kresse, J. Hafner, Ab initio molecular dynamics for liquid metals, Physical Review B, 47 (1993) 558.

[88] J.P. Perdew, K. Burke, M. Ernzerhof, Generalized Gradient Approximation Made Simple, Physical Review Letters, 77 (1996) 3865-3868.

[89] H.J. Monkhorst, J.D. Pack, Special points for Brillouin-zone integrations, Physical Review B, 13 (1976) 5188.

[90] C. Franchini, R. Podloucky, J. Paier, M. Marsman, G. Kresse, Ground-state properties of multivalent manganese oxides: Density functional and hybrid density functional calculations, Physical Review B, 75 (2007) 195128.

[91] X. Wu, D. Vanderbilt, D. Hamann, Systematic treatment of displacements, strains, and electric fields in density-functional perturbation theory, Physical Review B, 72 (2005) 035105.

[92] Y. Le Page, P. Saxe, Symmetry-general least-squares extraction of elastic data for strained materials from ab initio calculations of stress, Physical Review B, 65 (2002) 104104.

[93] S. Dudarev, G. Botton, S. Savrasov, C. Humphreys, A. Sutton, Electron-energy-loss spectra and the structural stability of nickel oxide: An LSDA+ U study, Physical Review B, 57 (1998) 1505.

[94] S. Grimme, Semiempirical GGA-type density functional constructed with a long-range dispersion correction, Journal of Computational Chemistry, 27 (2006) 1787-1799.

[95] S. Grimme, J. Antony, S. Ehrlich, H. Krieg, A consistent and accurate ab initio parametrization of density functional dispersion correction (DFT-D) for the 94 elements H-Pu, The Journal of Chemical Physics, 132 (2010) 154104.

[96] E.R. Johnson, A.D. Becke, A post-Hartree-Fock model of intermolecular interactions: Inclusion of higher-order corrections, The Journal of Chemical Physics, 124 (2006) 174104.

[97] A. Tkatchenko, M. Scheffler, Accurate molecular van der Waals interactions from ground-state electron density and free-atom reference data, Physical Review Letters, 102 (2009) 073005.

[98] P. Bultinck, C. Van Alsenoy, P.W. Ayers, R. Carbó-Dorca, Critical analysis and extension of the Hirshfeld atoms in molecules, The Journal of Chemical Physics, 126 (2007) 144111.

[99] S.N. Steinmann, C. Corminboeuf, A generalized-gradient approximation exchange hole model for dispersion coefficients, The Journal of Chemical Physics, 134 (2011) 044117.

[100] S.N. Steinmann, C. Corminboeuf, Comprehensive benchmarking of a density-dependent dispersion correction, Journal of Chemical Theory and Computation, 7 (2011) 3567-3577.

[101] K.K. Irikura, Experimental vibrational zero-point energies: Diatomic molecules, Journal of Physical and Chemical Reference Data, 36 (2007) 389-397.

[102] A.M. de Jong, J.W. Niemantsverdriet, Thermal desorption analysis: Comparative test of ten commonly applied procedures, Surface Science, 233 (1990) 355-365.

[103] T.A.D. D.P. Woodruff, Modern Techniques of Surface Science - Second Edition, Cambridge University Press, Cambridge, 1994.

[104] N. Mina-Camilde, C.I. Manzanares, J.F. Caballero, Molecular constants of carbon monoxide at $v = 0$, 1, 2, and 3: A vibrational spectroscopy experiment in physical chemistry, Journal of Chemical Education, 73 (1996) 804.

[105] K.M. Neyman, N. Rösch, Bonding and vibration of CO molecules adsorbed on low-coordinated surface sites of MgO: a LCGTO-LDF cluster investigation, Surface Science, 297 (1993) 223-234.

2.8 Supplemental document for chapter 1

2.8.1. Prefactors for terrace sites using Campbell and Seller's empirical entropic scaling relation.

The prefactor ν for adsorbates on flat terrace sites can be calculated using the empirical entropic scaling relation [1, 2]:

$$\nu = \frac{k_B T}{h} \exp\left\{0.30\,\frac{S^o_{gas}}{R} + 3.3 \; - \; \frac{1}{3}\left\{18.6 \; + \; \ln\left[\left(\frac{m}{m_{Ar}}\right)^{1.5}\left(\frac{T}{298\ K}\right)^{2.5}\right]\right\}\right\}$$

in which the variables are:

- k_B is the Boltzmann constant,
- h is the Planck constant,
- R is the ideal gas constant,
- T is the temperature of the adsorbate gas molecule, the desorption peak temperature from TPD, 130 K for CO in the low coverage limit,
- S_{gas}^o is the standard entropy of the gas molecule (CO) at measurement temperature T. At 130 K, S_{gas}^o is approximately 20.9 R [3].
- $\frac{m}{m_{Ar}}$ is the ratio between the adsorbate mass, and the mass of argon, which for a CO adsorbate is $\frac{28}{40} = 0.7$.

which gives $\nu = \mathbf{1.9 \times 10^{14}\ s^{-1}}$

2.8.2. Desorption temperature and prefactor estimates from DFT adsorption energies on defect sites

DFT estimates of adsorption energy and predictions for desorption temperatures from defect sites using the proposed scaling relationship in Equation 3,

a) $\nu_{defect} \approx \frac{\nu_{defect,TST}}{\nu_{terrace,TST}} \nu_{terrace,S_o}$

are related through three other equations and the temperature-dependent transition state expressions for the two TST prefactors. The first of these three additional equations is the first-order Redhead equation [4], the second equation is the relationship between activation energy for desorption and adsorption energy (combining equations 1 and 2 from section 2.2), and the third is the Campbell and Seller's empirical entropic scaling relation for $\nu_{terrace,S_o}$:

b) $\frac{E_a}{R\,T_p^2} = \frac{\nu_{defect}}{\beta} * \exp\left(-\frac{E_a}{R\,T_p}\right)$

c) $\Delta E_{ads} = -E_a + 0.5\,R\,T_p$

d) $\nu_{terrace,S_o} = \frac{k_B T}{h} \exp\left\{0.30\frac{S^o_{gas}}{R} + 3.3 - \frac{1}{3}\left\{18.6 + \ln\left[\left(\frac{m}{m_{Ar}}\right)^{1.5}\left(\frac{T}{298\,K}\right)^{2.5}\right]\right\}\right\}$

Solution requires a self-consistent determination of E_a, T_p, ν_{defect}, $\nu_{terrace,S_o}$, and the two temperature-dependent TST prefactors associated with defects and terraces. This system of highly-nonlinear equations was solved numerically using the SciPy package [5] (Python code available upon request). Two methods based on different starting assumptions were examined for estimating the desorption temperatures.

2.8.2.1. Method 1: The experimentally observed desorption peak temperature from terrace sites in the low coverage limit (130 K) was used to estimate the prefactors for terrace sites ($\nu_{terrace,TST}$ and $\nu_{terrace,\,S_o}$) leaving only the temperature dependence of $\nu_{defect,TST}$ in eqtn. 3 for estimating E_a, T_p, and ν_{defect} from equations a)-d) and the appropriate TST expressions for the different defects sites.

For step sites with the TST prefactors written in terms of the partition functions:

$$\nu_{step} \approx \frac{\frac{k_B\,T_p}{h}\kappa\,\frac{[q^{\neq}_{trans}(T_p)]^2\;q^{\neq}_{rot}(T_p)\;q^{\neq}_{vib}(T_p)}{q^{\text{step}}_{trans}(T_p)\;q^{\text{step}}_{vib}(T_p)}}{\frac{k_B\,(130\,K)}{h}\kappa\,\frac{[q^{\neq}_{trans}(130\,K)]^2\,q^{\neq}_{rot}(130\,K)\,q^{\neq}_{vib}(130\,K)}{[q^{terrace}_{trans}(130\,K)]^2\,q^{\text{terrace}}_{vib}(130\,K)}} * \nu_{terrace,\,S_o}(130K)$$

Note that all translational partition functions (q_{trans}) are 1-D partition functions, with only one degree of translational freedom attributed to step sites. ΔE_{ads} is the adsorption energy for CO on the step defect obtained from DFT simulation using PBE +U, along with DFT-D3 Becke-Johnson vdW correction, corrected for zero-point energy using harmonic approximation based on calculated vibrational frequencies. The DFT value of ΔE_{ads} for CO adsorption at a step defect is -129.8 kJ/mol.

For an oxygen vacancy point defect, the equation a is similar, but assumes zero degrees of translational freedom for the adsorbate at the point defect:

$$\nu_{OV} \approx \frac{\frac{k_B\,T_p}{h}\kappa\,\frac{[q^{\neq}_{trans}(T_p)]^2\,q^{\neq}_{rot}(T_p)\;q^{\neq}_{vib}(T_p)}{q^{\text{OV}}_{vib}(T_p)}}{\frac{k_B\,(130\,K)}{h}\kappa\,\frac{[q^{\neq}_{trans}(130\,K)]^2\;q^{\neq}_{rot}(130\,K)\;\;q^{\neq}_{vib}(130\,K)}{[q^{terrace}_{trans}(130\,K)]^2\;\;q^{\text{terrace}}_{vib}(130\,K)}} * \nu_{terrace,\,S_o}(130K)$$

where ΔE_{ads} is now the zero-point corrected DFT adsorption energy for CO in an oxygen vacancy point defect, -108.2 kJ/mol.

2.8.2.2. Method 2: For the second method, no temperature was assumed for the prefactors for terrace sites, and all prefactors were determined self consistently along with E_a and T_p. This route to a solution result in the complete cancellation of the transition state partition functions since the temperature used for all partition functions are identical. In addition to equations a)-d) the expressions for prefactors for step sites (one degree of translational freedom) and oxygen vacancy point defects (zero degrees of translational freedom) reduce to:

$$\nu_{step} \approx \frac{[q_{trans}^{terrace}(T_p)]^2 \; q_{vib}^{\text{terrace}}(T_p)}{q_{trans}^{\text{step}}(T_p) \; q_{vib}^{\text{step}}(T_p)} * \; \nu_{terrace,\, S_o}(T_p)$$

and

$$\nu_{OV} \approx \frac{[q_{trans}^{terrace}(T_p)]^2 \; q_{vib}^{\text{terrace}}(T_p)}{q_{vib}^{\text{OV}}(T_p)} * \; \nu_{terrace,\, S_o}(T_p)$$

For all cases, the temperature dependence of $S_{gas}{}^{o}$ in Campbell and Seller's correlation was calculated using Shomate equation [3].

2.8.2.3. Results and Comparisons

The two different methods for estimating the desorption temperature and prefactors from the DFT adsorption energies yield very similar results, both in terms of the predicted prefactors and the predicted desorption temperatures.

	Method 1	Method 2
ν_{step}	1.61×10^{17} sec^{-1}	2.17×10^{17} sec^{-1}
ν_{OV}	1.18×10^{19} sec^{-1}	1.60×10^{19} sec^{-1}
T_p (step)	386 K	384 K

T_p (OV)	297 K	296 K

2.8.3. Order plots from desorption isotherms

Order plots are generated from desorption isotherms that yield the desorption order, n, at a given temperature, T_n, from a linearized form of the desorption rate equation.

$$\ln(r) = \ln(k) + nln(\theta)$$

where r is the desorption rate at some temperature T_n, k is the desorption rate constant, and θ is the coverage at T_n. From a set of desorption traces at different initial coverages, the desorption rate and fractional coverage at a given temperature T_n are given by the intensity of the desorption signal at T_n and the area under the desorption trace for $T \geq T_n$, respectively. The desorption order n for a given temperature T_n is given by the slope of a plot of ln(r) vs ln(θ) extracted from traces at different initial coverages at T_n. The analysis assumes the desorption rate constant is nominally independent of coverage at a given temperature. This analysis generally works best on the low-coverage side of the trace [6], above 130 K for our traces in figure 2-2, as shown by the sample linearized desorption isotherms in figure 2-12.

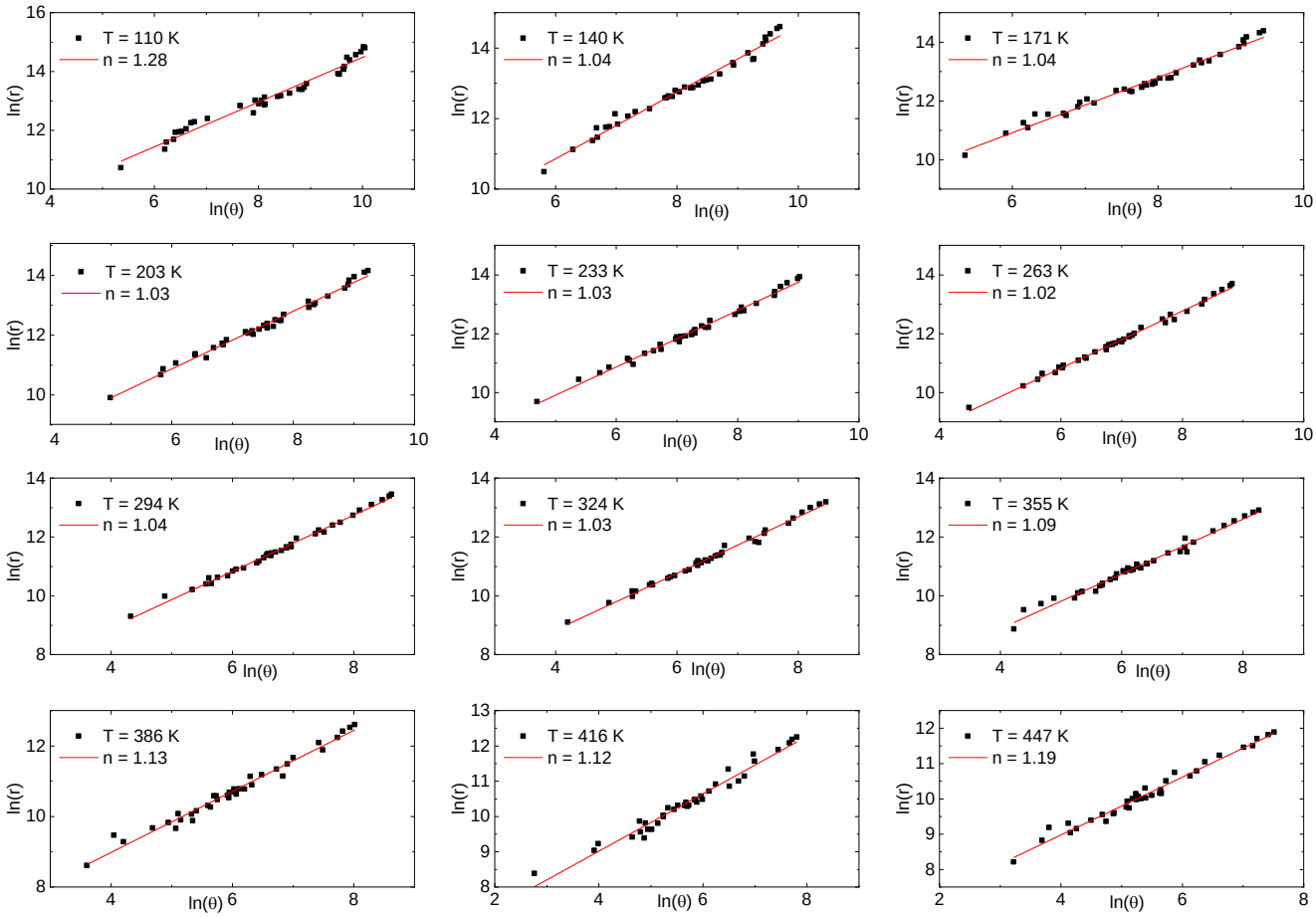

Figure 2-12 The desorption isotherms from sets of TPD traces at various temperatures. The slope of each plot is *n*, the desorption order at the given temperature.

References

[1] C.T. Campbell, J.R.V. Sellers, Enthalpies and Entropies of Adsorption on Well-Defined Oxide Surfaces: Experimental Measurements, Chemical Reviews, 113 (2013) 4106-4135.

[2] C.T. Campbell, J.R.V. Sellers, Correction to Enthalpies and Entropies of Adsorption on Well-Defined Oxide Surfaces: Experimental Results, Chemical Reviews, 113 (2013) 6902-6902.

[3] M. Chase Jr, NIST-JANAF thermochemical tables fourth edition, J. Phys. Chem. Ref. Data, Monograph, 9 (1998).

[4] P.A. Redhead, Thermal Desorption of Gases, Vacuum, (1962) 9.

[5] P. Virtanen, R. Gommers, T.E. Oliphant, M. Haberland, T. Reddy, D. Cournapeau, E. Burovski, P. Peterson, W. Weckesser, J. Bright, SciPy 1.0: fundamental algorithms for scientific computing in Python, Nature Methods, (2020) 1-12.

[6] A.M. de Jong, J.W. Niemantsverdriet, Thermal desorption analysis: Comparative test of ten commonly applied procedures, Surface Science, 233 (1990) 355-365.

Chapter 3

NH_3 adsorption on MnO(100): Experimental benchmarks compared to DFT

3.1 Introduction

Applications of DFT to problems in surface chemistry and catalysis have become ubiquitous, however, calculations involving transition metal oxides with highly-correlated electronic structure remain problematic [1, 2]. Despite some progress [3-6], the lack of quality experimental benchmarks is still an issue. Here we provide a benchmark study of NH_3 on MnO(100), where MnO is a transition metal oxide with highly-correlated electronic structure [7]. NH_3 has long been one of the standard molecules for probing surface acidic sites for oxides. One common method of probing surface acidity with NH_3 is through temperature-programmed desorption (TPD) [8]. Ammonia TPD can differentiate between energetically-different adsorption sites [9], provide a measure of adsorption energy and the amount adsorbed [10]. It can probe both Lewis-acid sites [11], and Brønsted acid site [12]. This work seeks to provide an experimental benchmark for NH_3/MnO(100) using TPD, along with density functional theory [13, 14] (DFT) calculations for this system to compliment a previous study of CO/MnO(100) [15].

Experimental TPD studies of NH_3 on single-crystal oxides surfaces are still uncommon. A notable study in recent years was the chemisorption of NH_3 on SnO_2 (110) [11], which reveals that in-plane oxygen vacancies unexpectedly reduce the Lewis acidity of nearby cations. In a studying involving laser-induced thermal desorption (LITD), Arthur et al. [16] observed repulsive lateral interactions between the adsorbate NH_3 molecules on MgO(100) and determined that the activation energy of desorption is inversely proportional to the square root of the relative coverage. Another study of NH_3 adsorption

on anatase TiO_2 (101) [17] showed a first-order activation energy of desorption of 119 kJ/mol in the low-coverage limit, and of 27 kJ/mol at higher coverages, which indicates repulsive lateral interactions between the adsorbate molecules with increasing coverage. Studies of the NH_3/NiO(100) adsorption system [18] and NH_3/Ru(001) [19] also suggest that the adsorption of NH_3 exhibits repulsive lateral interactions, with the apparent activation energy of desorption decreasing as coverage increases. Beyond the adsorbate/surface interactions, molecular dipole-dipole attractive interactions can lead to multilayers of NH_3 at low temperatures, with reported multilayer desorption temperatures ranging from 100 to 160 K [20, 21] in ultra-high vacuum.

In the absence of surface protons, NH_3 probes surface Lewis acid sites, with a nitrogen-down adsorption geometry on planar metal single-crystal surfaces [19, 22, 23], and onto surface cation site for metal oxide surfaces [16-18]. On NiO(100), a study of local symmetry by scanned-energy mode photoelectron diffraction [24] revealed that NH_3 binds to the surface Ni^{2+} sites through its lone pair electrons, but the Ni-N bond deviates from the surface normal by about 7 degrees.

To accompany the experimental studies, computational tools can be used to gain a deeper understanding of NH_3 adsorption onto well-defined metal oxide surfaces. For rocksalt (100) surfaces, the NH_3/MgO(100) system is the most studied [25-32] and is analogous structurally to to NH_3/MnO(100) system since MgO and MnO both have the rocksalt structure [27, 33]. Computational NH_3/MgO(100) adsorption studies agree on the general adsorption geometry being nitrogen down at a Mg cation, however, they reach different conclusions regarding the molecular axial tilt. A density-functional study [32] indicates a non-bonded, physisorption interaction with the molecular axis being vertical. A

semi-empirical potential energy surface study concurs with this conclusion [26]. A Car-Parrinello simulation predicts an axial tilt of 5-22 degrees away from the surface normal [27]. The adsorption geometry, including a possible axial tilt of the molecule, is a point of interest in investigating NH_3/MnO(100) adsorption system.

This work makes use of TPD to establish an adsorption energy benchmark for NH_3 on single-crystal MnO(100) for comparison to computational results. Mn^{2+} cations like those found on the MnO(100) surface are typically classified as hard acids [34], making NH_3 an ideal candidate as a probe. Also included are DFT calculations for NH_3 adsorption on terrace sites and two common defect sites: step edges, and oxygen vacancy point defects.

3.2 MnO(100)

MnO has a rocksalt structure [33] and is an insulator at room temperature [35] with a bandgap of 3.6 – 3.8 eV [36, 37]. MnO(100) is non-polar and thermodynamically stable [38, 39]. A ball model illustration of the ideal MnO(100) surface structure is shown in figure 3-1. Each Mn^{2+} cation and O^{2-} anion in the top atomic layer are five-fold-coordinated with one degree of coordinative unsaturation relative to the bulk. Each Mn^{2+} cation has a d^5, high-spin electronic configuration [40]. As a result, MnO has a highly correlated electronic structure. It is anti-ferromagnetic with an AFM-II ordering of the magnetic moments [7]. The arrangement of spin magnetic moments within a (100) plane is shown in figure 3-1 (a), with parallel spins along [011] [7, 41].

3.3 Methods

3.3.1. Experimental Methods

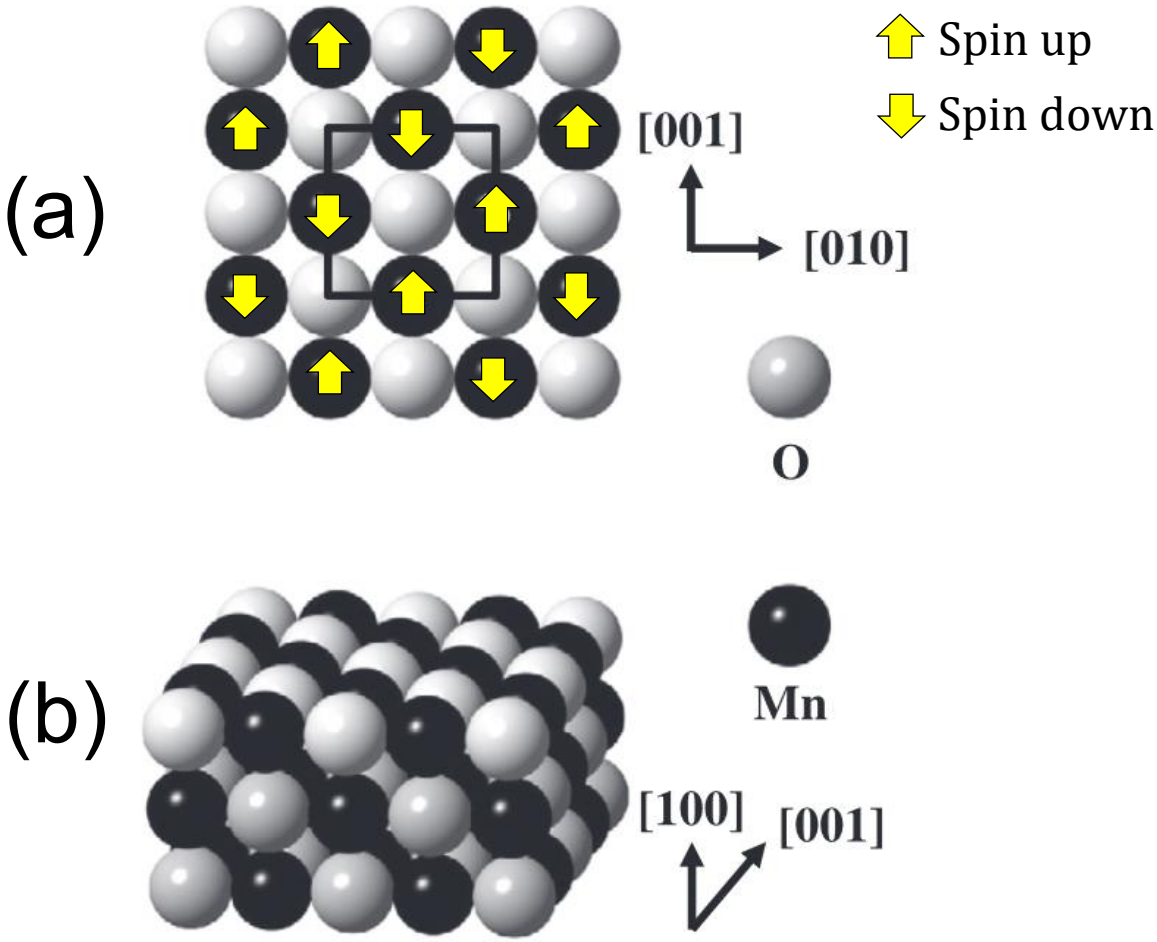

Figure 3-1 Ball model illustration of the ideal stoichiometric MnO(100) surface. (a) Top view of one layer of the MnO(100) surface looking down the [100] surface normal. The black spheres represent Mn^{2+} cations, white spheres represent O^{2-} cations. A unit cell on the surface of MnO(100) is labeled in black solid lines. The opposing magnetic moments related to (111) planes are illustrated with yellow arrows. (b) Cross-section view along the [001] direction. Adapted from Feng, Cox, (2016).

Temperature-programmed desorption (TPD) experiments were conducted in a stainless steel, ion-pumped, ultra-high vacuum system. The sample heating rate was limited to 2.5 K/sec because of the possibility of breakage due to thermal shock of our ceramic MnO(100) sample. The MnO(100) sample is dosed with ammonia after cooling to 85 K, with small exposures done with a variable leak valve, and larger exposures with a doser that provides an estimated enhancement factor of 3.3 [42]. The chamber contains an Inficon Quadrex 200 mass spectrometer for TPD experiments and is equipped with a glass skimmer that covers the ionization zone. The Matheson NH_3 (99.99%) gas is used as received. All doses have been corrected for ion gauge sensitivity, which was taken as 1.3 [43]. The chamber also contains a set of Princeton Research Instruments reverse view low-energy electron diffraction (LEED) optics. A Perkin-Elmer Phi 15-155 single-pass cylindrical mirror analyzer is used for Auger electron spectroscopy to examine surface cleanliness and composition. The chamber has a base pressure of 1×10^{-10} Torr.

The MnO(100) single crystal was purchased from SurfaceNet GmbH with an EPI polish and mounted on a tantalum sample holder connected to a manipulator via liquid-nitrogen-cooled copper rods. The sample temperature is measured by a type K thermocouple glued to the back of the sample with Aremco 569 ceramic cement through a hole in the tantalum sample holder. Before TPD experiments, the MnO(100) single-crystal surface is cleaned by bombardment with 2 keV Ar^+ ions, then heated to 1000 K for 10 min to establish an ordered surface with a (1×1) LEED periodicity. LEED observations are made at a temperature of 500 K where there is sufficient conductivity to prevent surface charging. This procedure yields a clean, ordered, nearly-stoichiometric MnO(100) surface as per previous work [44].

3.3.1.1. Obtaining adsorption energies from TPD

The activation energy for desorption, Ea, can be determined from TPD data via a Redhead analysis [45]. The experimental adsorption energy, ΔE_{ads}, can then be determined following equation 1 and 2:

$$\Delta H^{\circ}_{ads} = -(E_a + 0.5\, R\, T_p) \quad (1)$$

$$\Delta E_{ads} = \Delta H^{\circ}_{ads} + R\, T_p \quad (2)$$

where ΔH°_{ads} is the adsorption enthalpy, T_p the desorption peak temperature determined from the TPD experiment, and ΔE_{ads} is the adsorption energy. The first equation is derived by assuming equilibrium between adsorption and desorption rates and a temperature-independent prefactor and activation energy for desorption [46]. The second equation accounts for the ideal gas $\Delta(PV)$ contribution to enthalpy [47].

3.3.2. Computational methods

All simulations were performed using the projector-augmented-wave method [48, 49] within the Vienna Ab-initio Simulation Package (VASP) [50-52]. The Perdue-Burke-Ernzerhof (PBE) [53] approximation was used to account for exchange and correlation via a standard generalized gradient approximation (GGA). All DFT simulations were performed using a MnO cell that consists of 4-layers, 256 atom in accordance of our previous computational study [15]. In each simulation, one NH_3 molecule is placed on a (4×4) surface cell and geometry-optimized. This approach gives an equivalent coverage of 0.03 ML, with one ML defined as one NH_3 molecule per surface Mn^{2+} site. +U simulations using the method of Dudarev [54] were used to also provide another estimate of the adsorption energy because of the highly correlated electronic structure of MnO. A U-J value

of 4.0 eV yields the best energy of formation for bulk MnO [55], and is used in all +U calculations. In addition, a range of van der Waals (vdW) dispersion corrections [56-62]were used.

Calculations involving a single-atomic step defect and an oxygen vacancy point defect were also conducted. The step defect was created by removing half of the atoms in the top atomic layer to produce a step that runs along [010]. An oxygen vacancy defect was created by removing one top-layer lattice oxygen from the (4×4) surface unit cell. Both types of defective surfaces were geometry-optimized prior to the examination of NH_3 adsorption.

The ground state adsorption energy is defined as the difference between the internal energy of the adsorbed state (E_{ads}), where a molecule is adsorbed on the surface, and the internal energy of the initial state, where the internal energy of a gas molecule (E_{gas}) and the clean, geometry-optimized surface ($E_{surface}$) are calculated separately. Equation 3 below defines the adsorption energy, ΔE_{ads} [63]. Zero-point energy corrections, ΔZPE, have been included for all calculations, and are determined from the vibrational frequencies within the harmonic oscillator approximation that are obtained via a dynamical matrix calculations [64, 65] in VASP:

$$\Delta E_{ads} = E_{ads} - \left(E_{gas} + E_{surface}\right) + \Delta ZPE \qquad (3)$$

where the ΔZPE is calculated per equation 4 [66]:

$$\Delta ZPE \approx \sum_i \frac{h\,\nu_i^{ads}}{2} - \sum_i \frac{h\,\nu_i^{gas}}{2} \qquad (4)$$

where h is the Plank's constant and ν_i^{ads} and ν_i^{gas} are the frequencies of the vibrational modes of the molecules in the adsorbed state and in the free-molecule initial state.

3.4 Results

3.4.1. Experimental Results

3.4.1.1. TPD Results

TPD traces for NH_3 desorption from MnO(100) in the low dose range were accomplished by back filling the chamber with a variable leak valve, and are shown in figure 3-2. At the smallest dose of 0.02 L (figure 3-2 (a), 1 L = 1×10^{-6} Torr·sec), a small, symmetric desorption feature appears at 330 K. As the doses increase to 0.06 L and 0.08 L, the desorption feature grows and broadens to lower temperatures, where a second distinct desorption feature is first observed at 235 K. This second desorption feature further shifts down in temperature but merges with the higher temperature feature at higher coverages. A larger dose of 0.12 L sees the desorption feature shifting down in temperature to about 210 K, and at 0.56 L to about 170 K (figure 3-2 (b)). For doses from 0.06 L to 0.56 L as shown in figure 3-2 (b), a high-temperature desorption tail extends to about 500 K. For doses larger than 0.6 L with a leak valve, a desorption feature from the sample holder (not shown) appears at around 300 K, necessitating the use of a doser for larger exposures. Additionally, primary mass numbers for possible dissociation products, such as hydrazine, nitrogen and hydrogen, were monitored during the desorption process. No signs of these decomposition products were detected.

Figure 3-3 shows the desorption order versus temperature of NH_3 desorption from MnO(100) in the temperature range between 200 K and 500 K. The plot indicates that the desorption order, with some variations, is close to one. This order plot is determined using isotherms at various temperatures that are derived using TPD traces from figure 3-2 (b), a

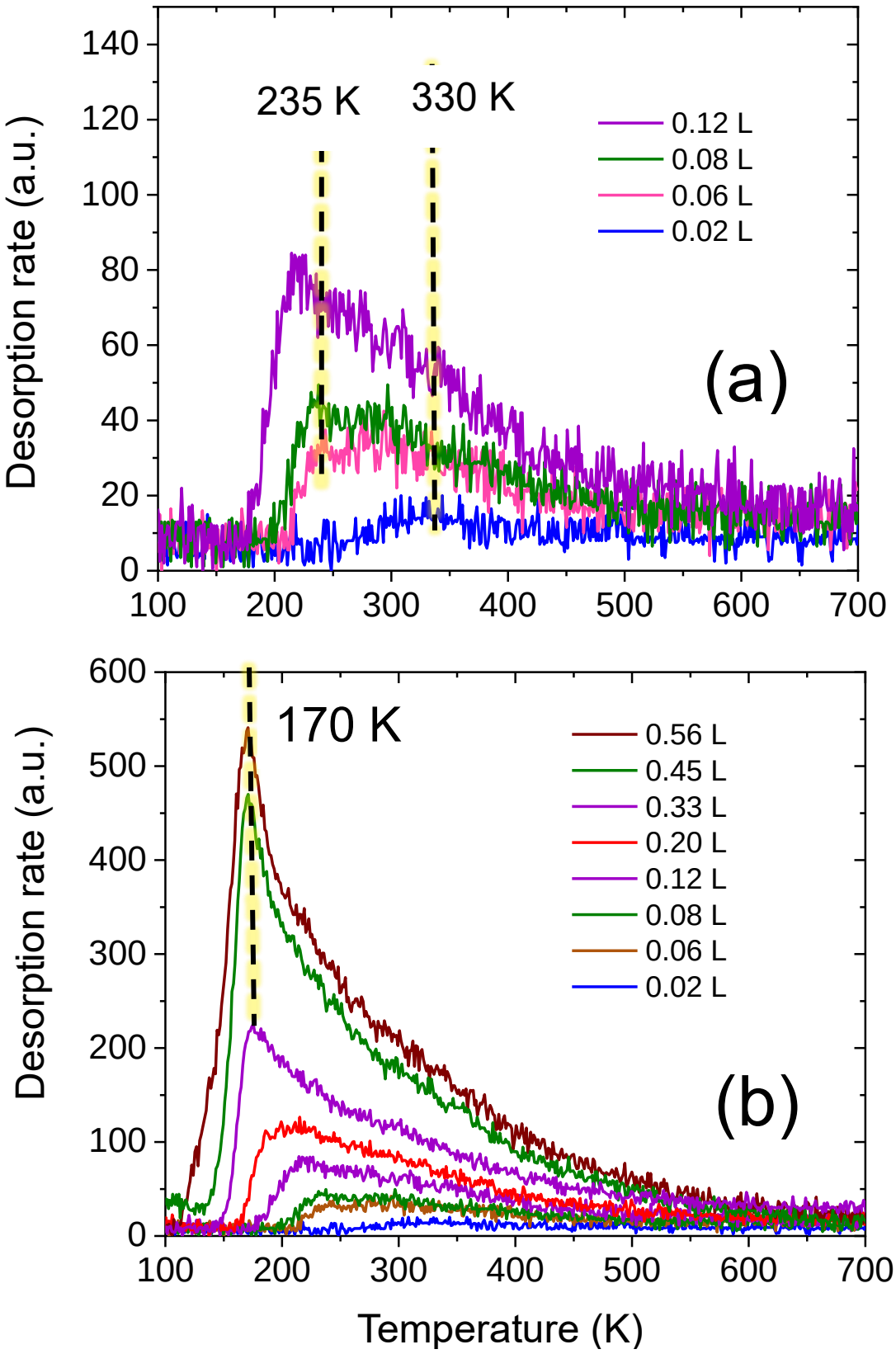

Figure 3-2 TPD traces of NH_3 desorption from MnO(100). The exposures range from 0.02 to 0.56 L. (a) smaller doses. (b) all doses.

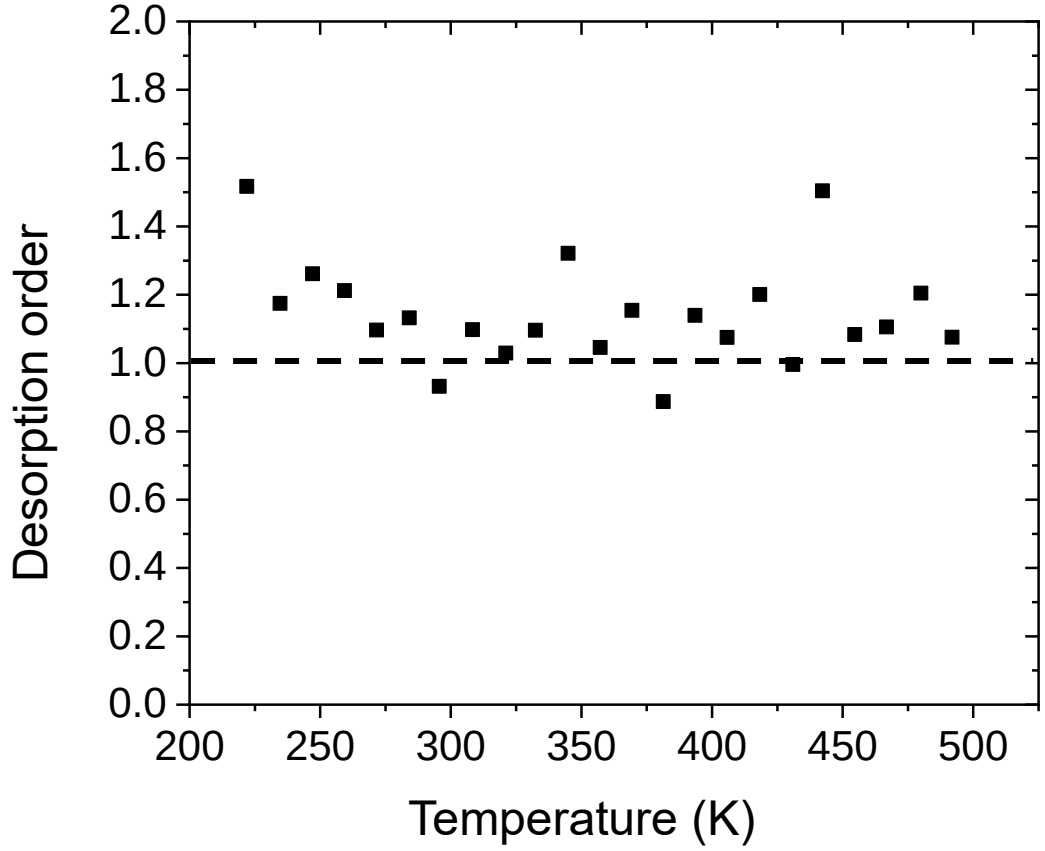

Figure 3-3 The aggregated order plot of NH_3 desorption from MnO(100) surface, in the temperature range of 200 to 500 Kelvin.

method that was also used in our previous work [15] (see supplemental materials for a more complete description). In general however, symmetric desorption peaks with a downward shift in peak temperatures with increasing coverages indicate second-order desorption [67, 68]. The desorption traces in figure 3-2 (b) show the downward shift in peaks, albeit with a tail to higher temperatures. This shift is also observed with NH_3 on rutile TiO_2(110)-1×1 [20], on anatase-TiO_2(101) [17], and also on MgO(100) where a similar tail to higher temperatures is observed [16]. This long tail is likely due to the difficulty of pumping NH_3 as the molecule has strong interaction with the chamber wall. In all three cases, the order of the desorption traces was determined to be first-order, with the downward shift in desorption temperature attributed to a coverage-dependent activation energy of desorption [16, 17, 20]. The observations of first-order desorption kinetics of NH_3 on other surfaces, and the indication of predominantly first-order desorption from the order plot both suggest the first-order kinetics. The desorption of NH_3 from MnO(100) is therefore attributed to a first-order desorption process with a coverage dependent activation energy of desorption. The axial alignment of the adsorbate NH_3 molecules gives rise to the repulsive dipole-dipole lateral interactions [63], which is the likely cause for the coverage-dependency.

The symmetric desorption feature at 330 K for a 0.02 L dose is likely the result of desorption from surface defects, with the broadening of the features for 0.06 and 0.08 L due to the presence of more than one adsorption site, with the weakest binding at about 235 K and the strongest binding at around 330 K. The 235 K peak is attributed to desorption from surface terrace sites, and the 330 K desorption from defect sites. The

dominant low-temperature features for doses above 0.08 L are also attributed to desorption from terraces.

Having established the first-order nature of the desorption, the experimental activation energy of desorption, E_a, can be readily determined from the first-order Redhead analysis [45]. Due to the possibility of a thermal shock, the use of a variable heating rate method in TPD for experimentally determining the desorption prefactor (υ), cannot be applied. Alternatively, υ is commonly assigned a value of 1×10^{13} sec^{-1} in ammonia TPD studies on various single-crystal metal oxide surfaces [16, 17, 20, 69]. An alternative approach using transition state theory [63, 70], while taking into account the entropic difference between gas phase and adsorbate phase NH_3. An entropic difference of 5.7R was determined experimentally in the low-coverage regime for the NH_3/MgO(100) smoke adsorption system [71], and is reasonably applicable here. This leads to an approximate prefactor value of 5.5×10^{12} sec^{-1}. Using this prefactor, and a desorption temperature of 235 K $\pm$5 K at the low-coverage limit from the terrace sites, an activation energy of desorption, E_a, of 59.7 $\pm$ 1.0 kJ/mol is determined, and a corresponding adsorption energy, ΔE_{ads}, of -58.7 $\pm$ 1.0 kJ/mol is determined for the low-coverage limit of terrace sites. The 1.0 kJ/mol margins of error arise from the propagation of errors including a $\pm$ 5 K temperature measurement error and the variations in the prefactor from 5.5×10^{12} sec^{-1} to 1.0×10^{13} sec^{-1}. The commonly-used prefactor of 1.0×10^{13} sec^{-1} leads to similar values of E_a (60.8 kJ/mol $\pm$ 1.0 kJ/mol), and an adsorption energy of -59.9 kJ/mol $\pm$ 1.0 kJ/mol.

It is assumed in this work that desorption is first-order at the defect, and thus the first-order Redhead analysis [45] can still be used. The desorption prefactors are generally larger at defects sites compared to those at terrace sites due to the loss of translational

degrees of freedom [63]. A molecule adsorbed at a step edge is unlikely to move freely beyond the step, and can be considered a 1-D gas with the loss of 1 degree of translational freedom compared to their counterpart at a terrace [72]. For an adsorbate molecule localized at a point defect, all translational motion is lost [73]. Adhering to this principle and utilizing methods of calculations outlined in our previous work [15], we estimate that the desorption prefactor should be 8.14×10^{13} sec^{-1} for NH_3 at a step edge, and 1.64×10^{15} sec^{-1} at an oxygen vacancy point defect, which are 15 and 300 times the prefactor at the terrace site, respectively.

3.4.1.2 TPD Results for higher doses

Figure 3-4 shows three TPD traces of NH_3 for higher exposures using a doser. The doser delivers higher effective pressures at the sample surface and minimizes the uptake on the sample holder. For the 1.5 L and 2.9 L exposures shown in figure 3-4, a temperature ramp of 2.5 K/sec was initiated immediately after the dose. For the 3.0 L exposure, the sample was allowed to sit in the vacuum for 3.5 minutes after the dose before initiation of the temperature ramp. For the 1.5 L trace, two distinct desorption peaks can be seen. A low-temperature desorption feature appears at 110 K, and a high temperature desorption feature at 155 K. From 1.5 to 2.9 L, the low-temperature peak increases in size while shifting upward to 115 K (typical for multi-layer desorption with zero-order kinetics [74]), while the other low-temperature desorption feature at 155 K appears to saturate. After substantial elapsed time in vacuum prior to the TPD, the third trace for a 3.0L dose closely follows the desorption feature at 155 K of the previous two traces, while showing only a minor shoulder near 115 K.

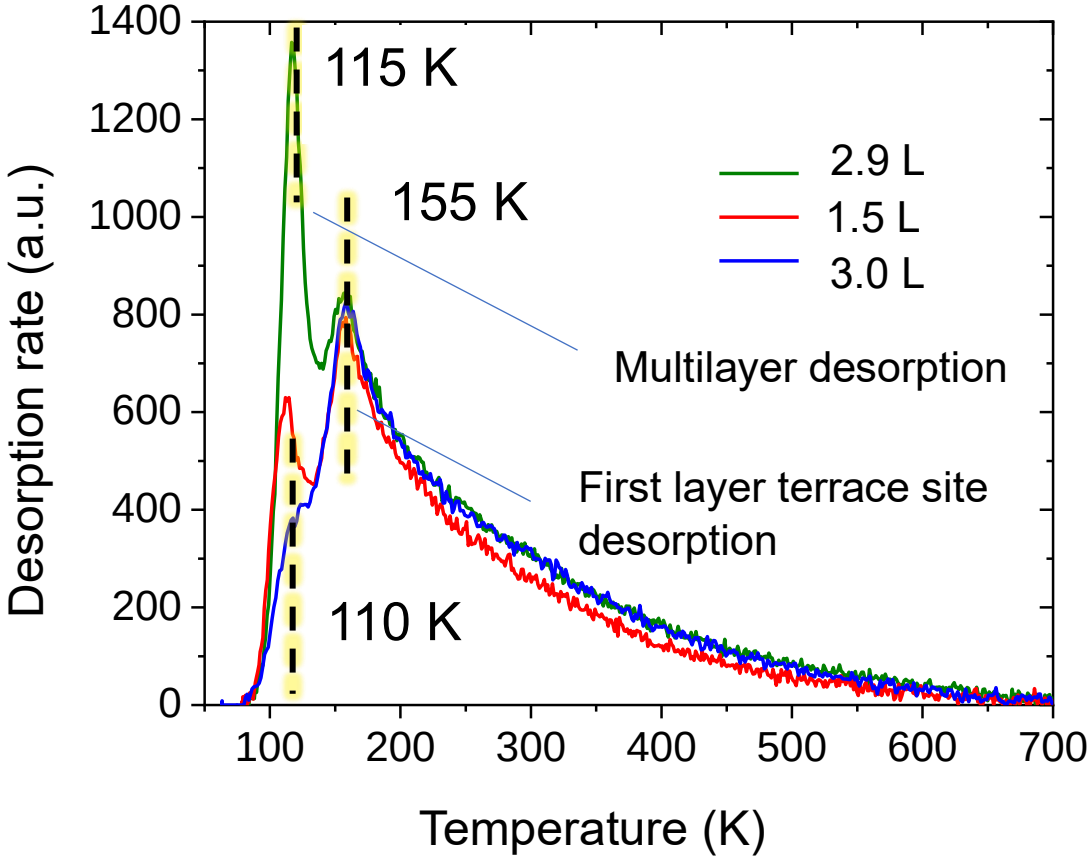

Figure 3-4 The TPD traces for larger NH_3 doses on MnO(100). The dosages are 2.9, 1.5, and 3.0 L. The 3.0 L trace experienced a 3.5-minute time delay before the temperature ramp. Lower desorption temperature feature is attributed to multilayer desorption. A higher, and saturated desorption temperature feature is attributed to desorption from the first layer terrace site desorption. The 3.0 L trace with time delay represents the saturation coverage of NH_3 on MnO(100).

The twin desorption features in figure 3-4 are also seen on anatase-TiO_2(101) [17], on TiO_2(110) [20], on graphite [75], and on Ag(111) [74]. On Ag(111), a multilayer desorption temperature of 104 K is reported [74], and on graphite, a multilayer desorption temperature of 94 K is reported [75]. These findings suggest that the desorption feature at 115 K observed in figure 3-4 can be attributed to multilayer desorption. The higher temperature desorption peak at 155 K is due to the desorption from surface terrace sites at saturation coverage. Without the higher effective pressure at the sample when using the doser, the multilayer desorption feature largely disappears under vacuum as demonstrated by the 3.0 L dose with a 3.5 min time-delay. The remaining trace of the 3.0 L dose represents a stable first-layer on the surface at the dosing temperature of 85 K, and is regarded as the saturation coverage of NH_3 in the first layer on MnO(100).

3.4.1.3 Coverage vs. dose

Figure 3-5 shows a plot of coverage vs. dose for the TPD traces shown in figure 3-2 (b), with integrated areas shown on the left axis and corresponding upper limit estimates of NH_3 coverage in monolayers (ML) on the right axis. An upper limit estimate of NH_3 coverage as a function of the dose was made using the kinetic theory of gases [76] to estimate the number of NH_3 collisions with the surface for a given dose, and assuming the sticking coefficient is unity at low coverage, where one ML is defined as one NH_3 molecule per surface Mn^{2+} site on a terrace. Also labeled in the dashed line in figure 3-5 is the saturation coverage of the NH_3 on MnO(100), which corresponds to 0.32 ML and is derived the integrated saturation coverage from the 3.0 L dose (figure 3-4). In the low dose regime, a unity sticking coefficient for NH_3 is reported for MgO (100) at 130 K [16], therefore the

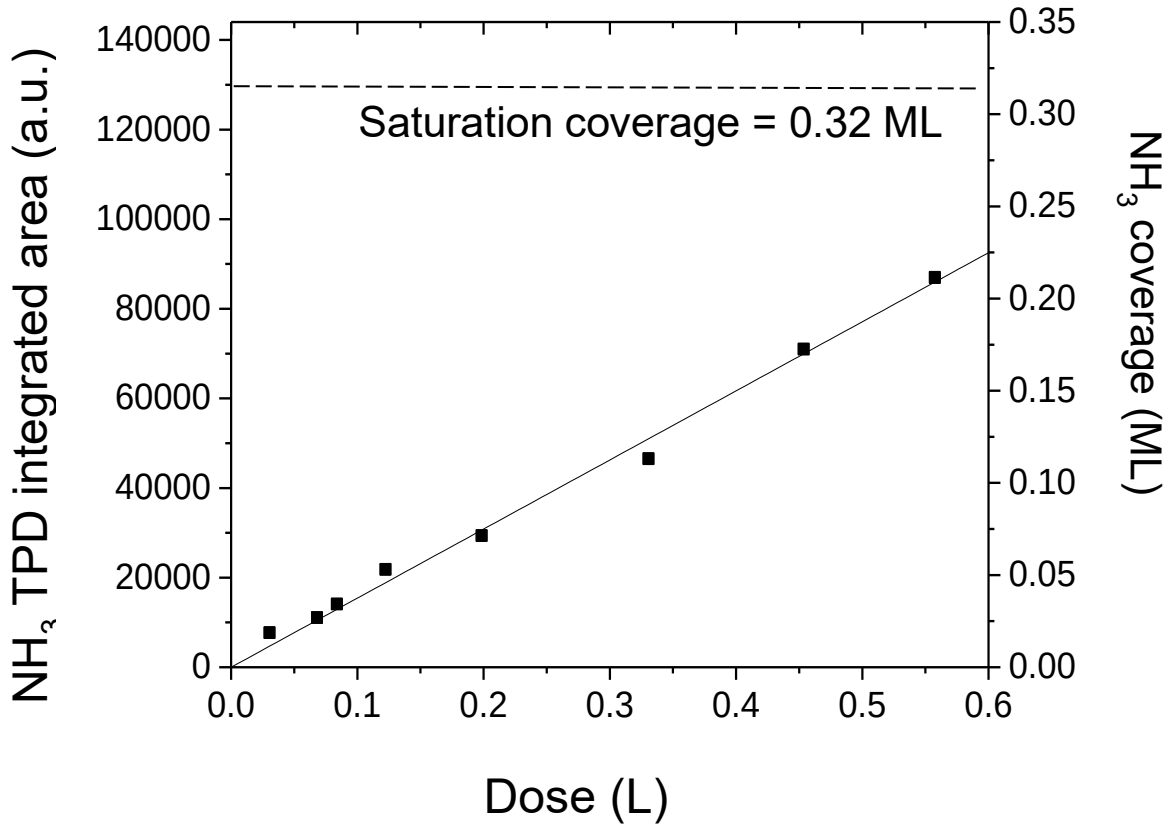

Figure 3-5 The coverage vs. dose plot of NH_3 on MnO(100), using background-dosing. The coverage is shown in two types of y-axis. The linear growth of coverage with respect to dose implies that the sticking coefficient is unity. The saturation coverage achieved using doser is shown in the dashed line.

assumption of an initial sticking coefficient of unity on MnO(100) at 85 K seems reasonable.

We believe that the maximum coverage at surface defects is achieved near 0.08 L, as evidenced by the disappearing prominence of the defect desorption feature at 330 K peak at higher doses. Additionally, a scaling factor of 2.8 applied to the 0.02 L trace accounts for the majority of the 0.08 L desorption trace with the exception of the portion of the signal near 235 K. While the low signal-to-noise ratio of the original traces gives rise to a very noisy difference trace (not shown), the results suggest an equivalent "defect coverage" on the order of about 0.04 ML.

Similar saturation coverages of NH_3 for the first-layer are reported in the literature. For example, on Pt(111), a saturation coverage of 0.25 NH_3 per Pt surface atom is observed [77]. On Ni(111) surface, a saturation coverage of 0.14 NH_3 per Ni surface atoms [78] is observed. These values indicate that the adsorbate dipole-dipole NH_3 repulsion is substantial. The saturation coverage of 0.32 ML observed on MnO(100) is higher than these two observed on metal surfaces. It is suggested that this can be explained by the presence of lattice oxygens on the surface, which spaces out the cation adsorption sites and subsequently lowers the repulsions between NH_3 molecules on adjacent cation sites.

3.4.2. Simulation Results

To gain better insight into the adsorption behavior of NH_3 on a MnO(100) for comparison to the experimental benchmarks, DFT simulations of NH_3 on a terrace, and on two common defects (step defect, and oxygen vacancy point defect) are simulated using PBE and PBE+U to gain insight into the adsorption geometry and calculate adsorption

energies. Various van der Waals corrections are also studied to determine their impact on the adsorption energy.

3.4.2.1. PBE simulations of NH_3 on a MnO(100) terrace

Simulations for NH_3 on a MnO(100) terrace using the PBE functional (Figure 3-6 a) yield an adsorption energy, ΔE_{ads}, of -49.5 kJ/mol for an equivalent coverage of 0.03 ML (1 adsorbate molecule per (4×4) surface cell). The simulation gives a tilted NH_3 that adsorbs N-down on a surface Mn cation, but also gives rise to a (2×2) surface reconstruction of the top atomic layer. With the addition of van der Waals corrections, the reconstruction persists. Because of the insulating nature of MnO and the low temperature (235 K) onset of desorption from terrace sites, the structure cannot be examined experimentally with LEED. We note that PBE simulations of Na adatoms on MnO(100) [44] and of CO adsorption on MnO(100) [15] predict a similar reconstruction. In the case of Na adatoms, no reconstruction is observed experimentally[44]. In the case of CO, it was argued that the adsorption is weak and unlikely to drive a surface reconstruction. Similarly, it is believed that the strength of the NH_3 surface interaction is not sufficient to drive a surface reconstruction (with an adsorption energy of -61.9 $\pm$ 1.0 kJ/mol).

3.4.2.2. PBE+U simulations of NH_3 on a MnO(100) terrace

More simulations was performed using PBE+U along with van der Waals corrections. The +U package is used for the strongly correlated electronic structure of MnO [41, 55]. NH_3 adsorbs nitrogen-down at a surface Mn^{2+} site, in a slightly tilted geometry of 5 degrees from the surface normal (figure 3-6b, 3-7a and 3-7b). The predicted

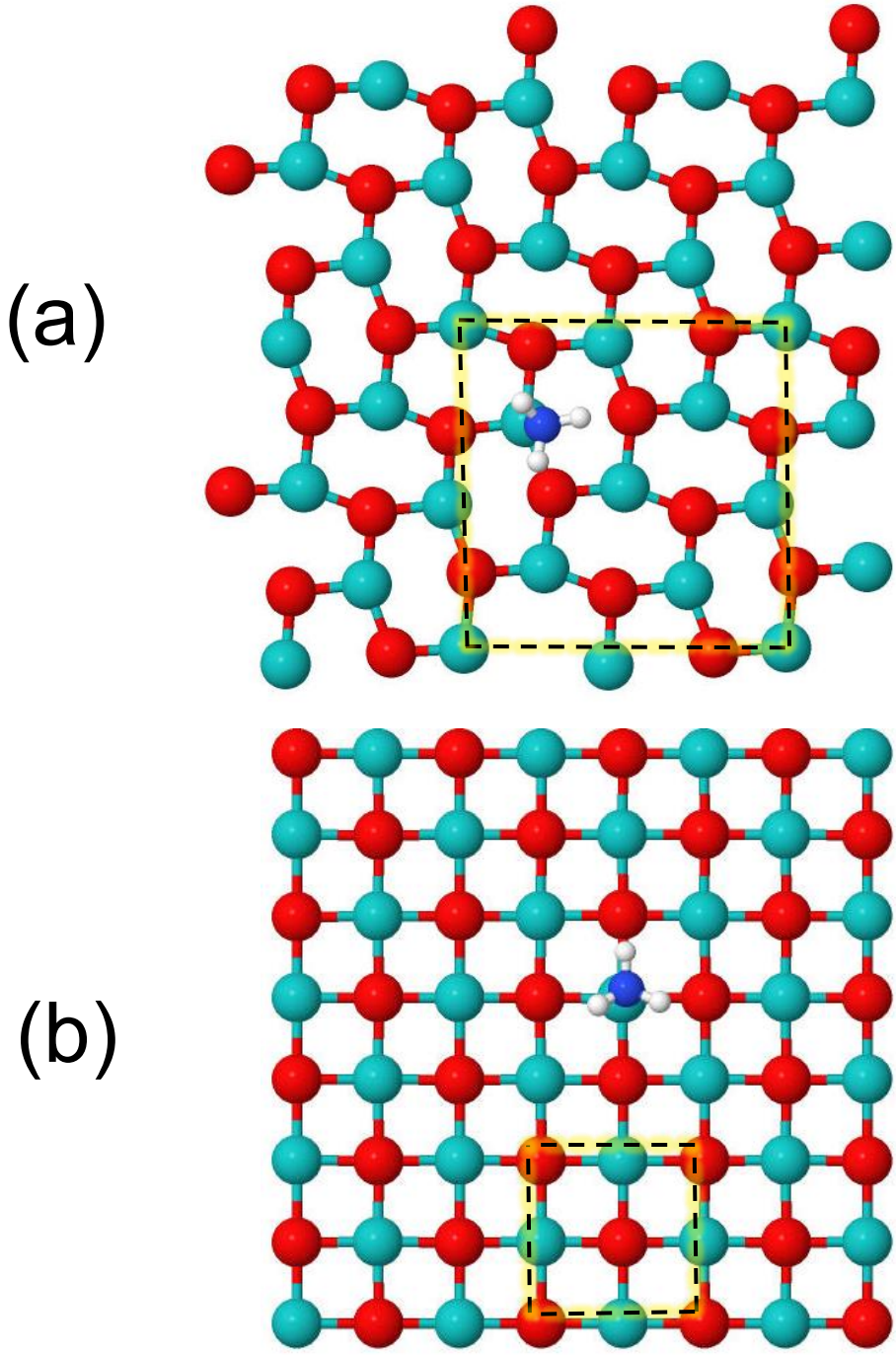

Figure 3-6 (a) A top view of the surface reconstruction caused by the adsorption of a NH_3 molecule on the MnO(100) surface using the PBE functional alone. Only the top layer of MnO(100) is shown. The (2×2) reconstruction pattern is shown with dashed lines. (b) A top view of the surface with NH_3 adsorption using PBE+U as the method. A surface unit cell is labeled in dashed lines. No surface reconstruction is present when PBE+U is used.

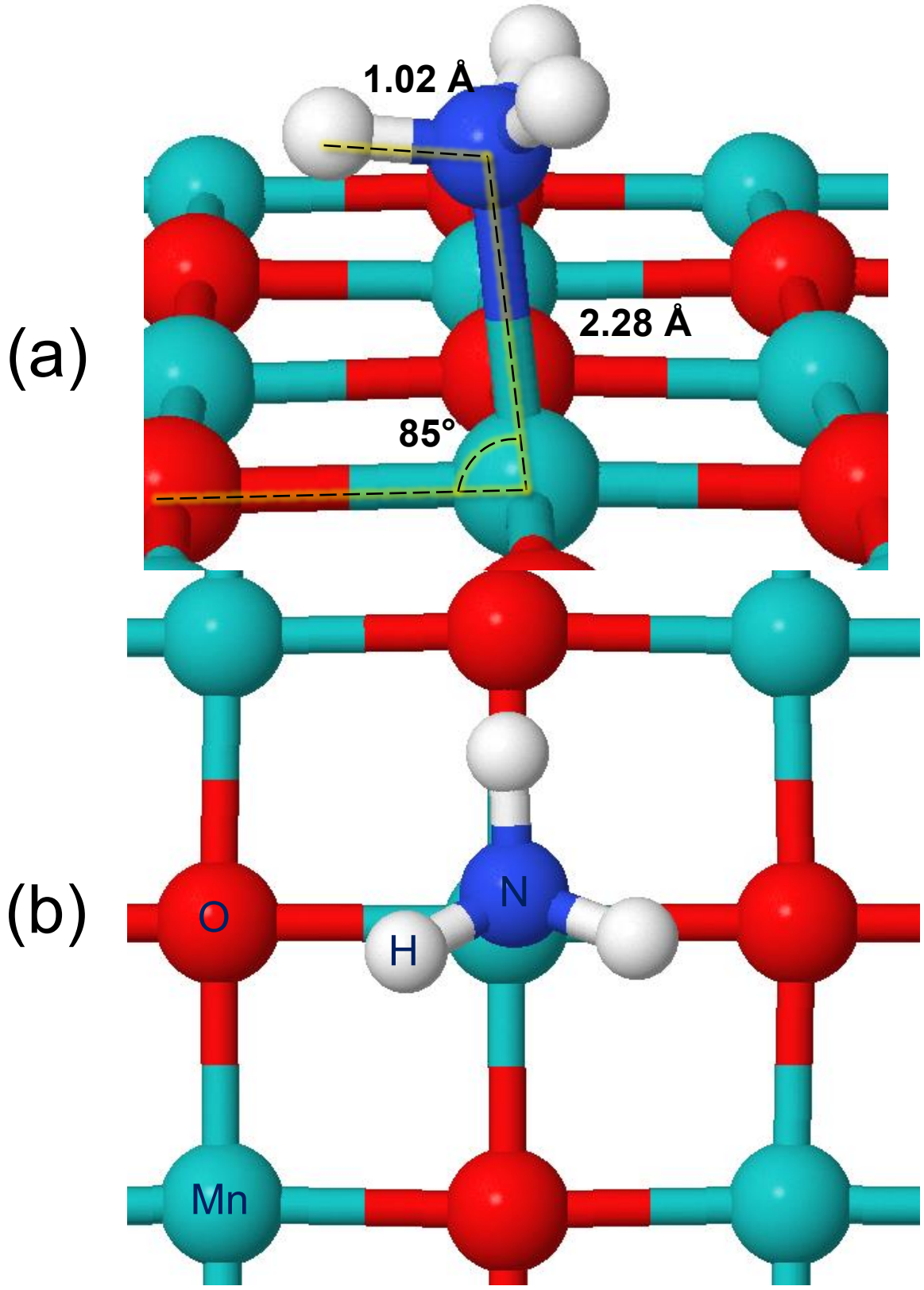

Figure 3-7 The NH_3 adsorbing onto MnO(100) terrace sites, with side (a) and top (b) viewing angles. Types of atoms are labeled in (b).

Mn-N bond is 2.28 Å, H-N bonds have a length of 1.02 Å (identical to a N-H bond length of a free molecule). No surface reconstruction appears with simulations using PBE+U. A pre-dissociated NH_3 (NH_2- and H- on adjacent cations and anions, respectively) recombines to adsorbed NH_3 in the simulation, demonstrating the expected propensity to molecular rather than dissociative adsorption. Using PBE+U without vdW corrections gives an adsorption energy, ΔE_{ads}, of -41.4 kJ/mol. The simulations with vdW corrections do not predict significant differences in the adsorption geometry, but the ΔE_{ads} vary in the low coverage limit as shown in table 3-1, where 1 NH_3 per 4×4 surface unit cell is simulated. Among all the approaches, PBE+U with a vdW correction based on the Tkatchenko-Scheffler method with iterative Hirshfeld partitioning predicts an ΔE_{ads} (-58.9 kJ/mol) that falls within the experimental error for the measured ΔE_{ads} (-58.7 $\pm$ 1.0 kJ/mol).

3.4.2.3. DFT Simulations of NH_3 on a step edge defect

In section 3.1, NH_3 desorption from a defect site was identified with a desorption feature at 330 K. For comparison, PBE+U simulations are used to examine two types of common defects (steps and oxygen vacancies). The structure of a NH_3 at a step defect is shown in figure 3-8. NH_3 adsorbs molecularly onto an Mn^{2+} cation on the step edge, with one hydrogen aligned toward an adjacent O^{2-} on the step. The effects of the hydrogen bond are clearly present as the attracted hydrogen has a slightly lengthened N-H bond (1.06 Å, compared to a free NH_3 N-H bond 1.02 Å). The Mn-N bond is 2.17 Å. The O-H bond length is 1.79 Å (in comparison, H_2O dissociates at the step edge as predicted by PBE+U). Figure 3-8 also shows that the adsorbate NH_3 introduced structural distortions at the adsorption site, lengthening the Mn-O distance at the adsorption site from 2.28 Angstroms to 3.66

(a)

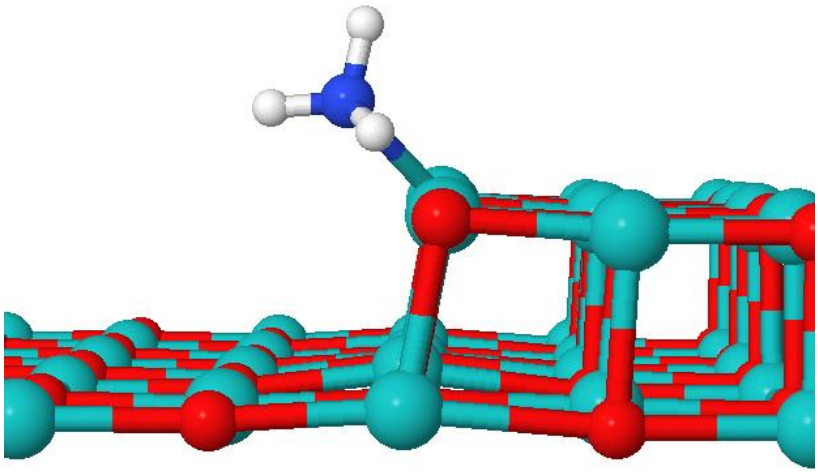

(b)

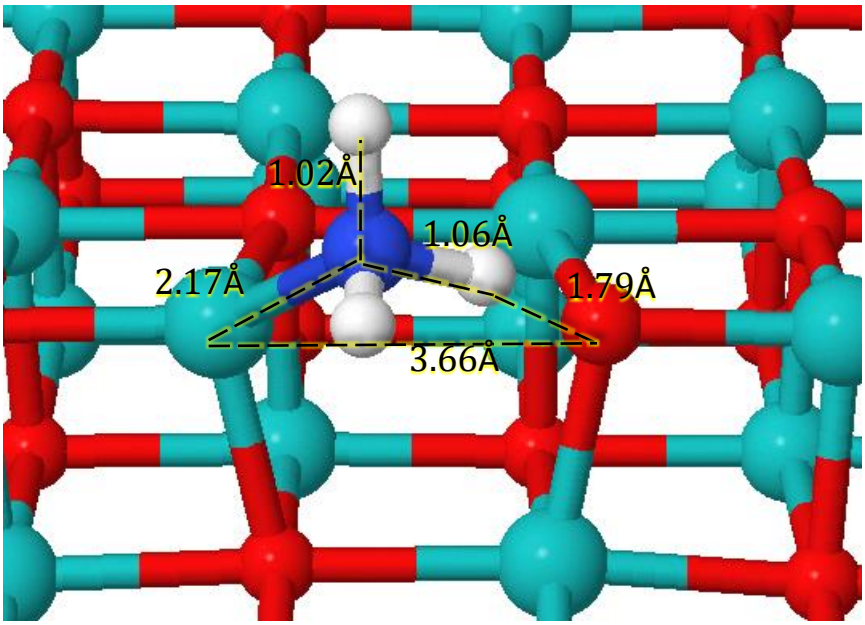

Figure 3-8 The NH_3 adsorbing onto MnO(100) step defect, from two viewing angles.

Angstroms. PBE+U predicts an adsorption energy of NH_3 at a step defect site to be -140.7 kJ/mol. Using this value, the prefactor for step sites, and the method described in our previous work [15], an estimated desorption temperature for NH_3 from the simulated step edge is found to be 505 K.

3.4.2.4. DFT Simulations of NH_3 at an oxygen vacancy

Simulations were used to investigate NH_3 adsorption at an oxygen vacancy point defect with PBE+U. Initially, one lattice oxygen on the top layer of MnO(100) is removed from the cell, and a NH_3 molecule replaces the missing oxygen, N-down. As the surface geometry relaxes, the adsorbate molecule moves to the side, and eventually adsorbs on a cation adjacent to the vacancy as shown in figure 3-9. Compared to adsorption on a terrace site, the molecular bond length varied little. The Mn-N bond deviates more from the surface normal (14° compared to 5° of deviation at a terrace site). The adsorption energy for NH_3 near an oxygen vacancy point defect is -67.5 kJ/mol, and the predicted desorption temperature for NH_3 from the simulated oxygen vacancy is at 230 K.

3.4.2.5. Discussion of simulation results

For simulations of NH_3 on terrace sites, PBE+U with the Tkatchenko-Scheffler method with iterative Hirshfeld partitioning (hereby abbreviated as PBE+U with TSHP) yields an ΔE_{ads} value (-58.9 kJ/mol) that falls within the experimental error. It is notable that, even though PBE+U with TSHP gives the best prediction in the case of NH_3 adsorption on the terrace, our previous work on CO/MnO(100) benchmark study [15] determined that PBE+U with D3 Becke-Johnson gives the most accurate ΔE_{ads} instead. The difference between D3 Becke-Johnson, and TSHP in accounting for vdW dispersion contribution,

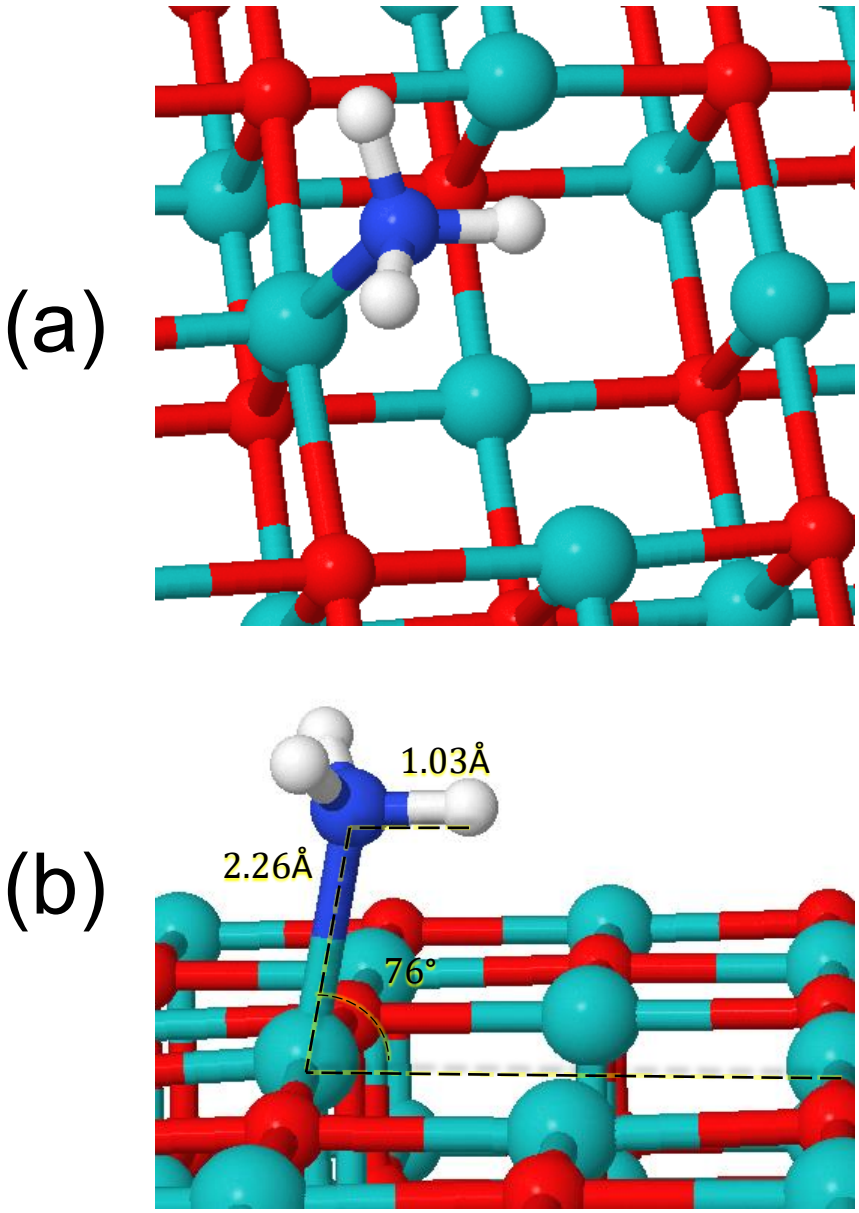

Figure 3-9 The NH_3 adsorbing onto MnO(100) a cation, next to the oxygen vacancy point defect, from two viewing angles.

despite the common origin of D2 method of Grimme [56], is the way the dispersion coefficients are calculated, which scale the dispersion energies. For D3 Becke-Johnson, the dispersion coefficients depend on the coordination number [58], whereas for TSHP, the coefficients depend on charge density at a given atom [60]. As demonstrated, the approach on vdW corrections by focusing on the charge density (PBE+U with TSHP) is superior to the approach by focusing on coordination number (PBE+U with D3 Becke-Johnson) in the case of NH_3/MnO(100) adsorption system.

A scanned-energy mode photoelectron diffraction experiment [24] revealed that NH_3 adsorbs onto the structurally-similar NiO(100) surface in a tilted-geometry, deviating $7 \pm 6°$ from the surface normal similar to NH_3 on MnO(100). The likely cause for the tilt is the hydrogen bond attraction between the hydrogen and an adjacent lattice oxygen [79]. The PBE+U predict a similar tilt on MnO(100).

In contrast to the good predictions on the adsorption of NH_3 on MnO(100) terrace sites, the simulation did not adequately explain the experimental observations for NH_3 desorption from the surface defect sites. The simulation results suggest that NH_3 from a step edge would lead to a desorption temperature at about 500 K, and NH_3 from an oxygen vacancy point defect at about 230 K. Neither temperature aligns with the experimentally observed desorption temperature of 330 K from surface defect sites. It is possible that the nature of the defects is neither of a step edge nor of an oxygen vacancy point defect. Another possibility is that the methods do not adequately describe the adsorption chemistry at the defect site. Similarly, our previous work with CO on MnO(100) also fails to explain the desorption from surface defect sites via simulating CO adsorption at the step defect and oxygen vacancy defect [15]. In both our previous work and in this work, the

DFT-predicted desorption temperature at the step edge were higher than the experimentally observed desorption temperature from the surface defect. For adsorption at an oxygen vacancy defect, DFT over-predicted the desorption temperature for the surface defect site in the case of CO [15], while under-predicting in the case of NH_3.

3.5. Conclusion

We conducted a TPD study of NH_3 adsorption on MnO(100) with complimentary DFT simulations. NH_3 TPD and its subsequent analysis revealed that adsorption energy on MnO(100) is coverage-dependent, and can be divided into adsorption at surface terrace sites, and at surface defect sites. In the low-coverage limit, the adsorption energy on terraces is -58.7$\pm$ 1.0 kJ/mol. A higher effective pressure for NH_3 introduced by a doser results in the formation of a transient NH_3 multilayers. The result also revealed that the saturation coverage of the first layer is 0.32 ML.

The PBE functional alone predicts an unreasonable reconstruction at the surface upon NH_3 adsorption. For a terrace site, PBE+U predicts a more realistic surface adsorbate geometry with NH_3 adsorbing N-down at a surface cation in slightly tilted geometry, which is also observed experimentally on other single-crystal rocksalt surfaces. PBE+U with Tkatchenko-Scheffler method with iterative Hirshfeld partitioning provides the best prediction on the adsorption energy. The simulations of NH_3 at a step site and oxygen vacancy did not adequately represent the experimental features attributed to desorption from defects.

3.6 Tables

	Coverage *ML*	Adsorption energy, E_{ads} *kJ/mol*
TPD trials (terrace sites)	0.034	-58.7 $\pm$ 1.0
PBE + U	0.031	-41.4
PBE + U, D2 Grimme	0.031	-61.6
PBE + U, D3 Grimme	0.031	-65.3
PBE + U, D3 Becke-Johnson	0.031	-62.5
PBE + U, TS	0.031	-70.1
PBE + U, TSHP	0.031	-58.9
PBE + U, dDsC	0.031	-60.7

Table 3-1 The comparison between experimentally and computationally obtained adsorption energies of NH_3 on flat terrace sites of MnO(100) at the low-coverage limit. The coverages from the TPD experiments are calculated using methods discussed in 3.4.1.3. The zero-point energy corrections have been applied to the calculated adsorption energies. All coverages associated with PBE are simulation coverages determined using 1 adsorbate molecule per 4×4 unit cell as basis as figure 3-6 illustrates, assuming only top-layer Mn^{2+} are adsorption sites.

References

[1] C. Franchini, V. Bayer, R. Podloucky, J. Paier, G. Kresse, Density functional theory study of MnO by a hybrid functional approach, Physical Review B, 72 (2005) 045132.

[2] A.J. Cohen, P. Mori-Sánchez, W. Yang, Insights into Current Limitations of Density Functional Theory, Science, 321 (2008) 792-794.

[3] J.D. Brooks, Q. Ma, D.F. Cox, Reactions of ethyl groups on a model chromia surface: Ethyl chloride on stoichiometric α-Cr_2O_3 (101¯2), Surface Science, 603 (2009) 523-528.

[4] Y. Dong, J.D. Brooks, T.-L. Chen, D.R. Mullins, D.F. Cox, Methylene migration and coupling on a non-reducible metal oxide: The reaction of dichloromethane on stoichiometric α-Cr_2O_3(0001), Surface Science, 632 (2015) 28-38.

[5] C. Zhang, H. Cao, C. Wang, M. He, W. Zhan, Y. Guo, Catalytic mechanism and pathways of 1, 2-dichloropropane oxidation over $LaMnO_3$ perovskite: An experimental and DFT study, Journal of Hazardous Materials, 402 (2020) 123473.

[6] Q.T. Trinh, K. Bhola, P.N. Amaniampong, F.o. Jérôme, S.H. Mushrif, Synergistic application of XPS and DFT to investigate metal oxide surface catalysis, The Journal of Physical Chemistry C, 122 (2018) 22397-22406.

[7] W. Roth, Magnetic structures of MnO, FeO, CoO, and NiO, Physical Review, 110 (1958) 1333.

[8] P.C. Stair, The concept of Lewis acids and bases applied to surfaces, Journal of the American Chemical Society, 104 (1982) 4044-4052.

[9] P.J. Barrie, Analysis of temperature programmed desorption (TPD) data for the characterisation of catalysts containing a distribution of adsorption sites, Physical Chemistry Chemical Physics, 10 (2008) 1688-1696.

[10] A. Santra, B.K. Min, C. Yi, K. Luo, T. Choudhary, D. Goodman, Decomposition of NH_3 on Ir (100): A Temperature Programmed Desorption Study, The Journal of Physical Chemistry B, 106 (2002) 340-344.

[11] M.W. Abee, D.F. Cox, NH_3 chemisorption on stoichiometric and oxygen-deficient SnO_2(110) surfaces, Surface Science, 520 (2002) 65-77.

[12] G. Martins, G. Berlier, C. Bisio, S. Coluccia, H. Pastore, L. Marchese, Quantification of Brønsted acid sites in microporous catalysts by a combined FTIR and NH_3-TPD study, The Journal of Physical Chemistry C, 112 (2008) 7193-7200.

[13] W. Kohn, L.J. Sham, Self-consistent equations including exchange and correlation effects, Physical Review, 140 (1965) A1133.

[14] P. Hohenberg, W. Kohn, Inhomogeneous Electron Gas, Physical Review, 136 (1964) B864-B871.

[15] H. Chen, D.F. Cox, CO adsorption on MnO (100): experimental benchmarks compared to DFT, Surface Science, (2021) 121808.

[16] D. Arthur, D. Meixner, M. Boudart, S. George, Adsorption, desorption, and surface diffusion kinetics of NH_3 on MgO (100), The Journal of Chemical Physics, 95 (1991) 8521-8531.

[17] S. Koust, K.C. Adamsen, E.L. Kolsbjerg, Z. Li, B. Hammer, S. Wendt, J.V. Lauritsen, NH_3 adsorption on anatase-TiO_2 (101), The Journal of Chemical Physics, 148 (2018) 124704.

[18] M.C. Wu, C.M. Truong, D.W. Goodman, Interactions of ammonia with a nickel oxide (100) surface studied by high-resolution electron energy loss spectroscopy and temperature programmed desorption spectroscopy, The Journal of Physical Chemistry, 97 (1993) 4182-4186.

[19] C. Benndorf, T.E. Madey, Adsorption and orientation of NH_3 on Ru (001), Surface Science, 135 (1983) 164-183.

[20] B. Kim, Z. Li, B.D. Kay, Z. Dohnálek, Y.K. Kim, The effect of oxygen vacancies on the binding interactions of NH3 with rutile TiO 2 (110)-1× 1, Physical Chemistry Chemical Physics, 14 (2012) 15060-15065.

[21] D. Thornburg, R. Madix, Cleavage of NH bonds by active oxygen on Ag (110): I. Ammonia, Surface Science, 220 (1989) 268-294.

[22] D. Chrysostomou, J. Flowers, F. Zaera, The thermal chemistry of ammonia on Ni (110), Surface Science, 439 (1999) 34-48.

[23] J.L. Gland, B.A. Sexton, G.E. Mitchell, Ammonia adsorption on the Ag (110) surface, Surface Science, 115 (1982) 623-632.

[24] M. Kittel, J.T. Hoeft, S. Bao, M. Polcik, R.L. Toomes, J.-H. Kang, D.P. Woodruff, M. Pascal, C.L. Lamont, The local adsorption geometry of CO and NH3 on NiO (1 0 0) determined by scanned-energy mode photoelectron diffraction, Surface Science, 499 (2002) 1-14.

[25] S. Picaud, A. Lakhlifi, C. Girardet, NH3 physisorption on MgO (100) substrate. Potential calculations revisited, The Journal of chemical physics, 98 (1993) 3488-3495.

[26] A. Lakhlifi, C. Girardet, Potential surfaces and adsorption energy of Xe, CH_4, N2, CO, NH_3 and CH_3F molecules on a MgO substrate, Surface science, 241 (1991) 400-415.

[27] W. Langel, Car-Parrinello simulation of NH3 adsorbed on the MgO (100) surface, Chemical physics letters, 259 (1996) 7-14.

[28] A. Lakhlifi, S. Picaud, C. Girardet, A. Allouche, Vibrational infrared spectrum of NH3 adsorbed on MgO (100). II. Interatomic potential calculations, Chemical physics, 201 (1995) 73-85.

[29] A. Allouche, F. Cora, C. Girardet, Vibrational infrared spectrum of NH_3 adsorbed on MgO (100). I. Ab initio calculations, Chemical physics, 201 (1995) 59-71.

[30] M. Havighorst, M. Prager, G. Coddens, NH_3 on the MgO {100} surface: spectroscopic evidence of coupled internal and centre of mass quantum rotation, Chemical Physics Letters, 259 (1996) 1-6.

[31] Y. Nakajima, D. Doren, Ammonia adsorption on MgO (100): A density functional theory study, The Journal of Chemical Physics, 105 (1996) 7753-7762.

[32] S. Pugh, M. Gillan, The energetics of NH_3 adsorption at the MgO (001) surface, Surface Science, 320 (1994) 331-343.

[33] J. Kolorenč, L. Mitas, structural phase transition in MnO under pressure: Comparison of all-electron and pseudopotential approaches, Physical Review B, 75 (2007) 235118.

[34] R.D. Hancock, A.E. Martell, Hard and soft acid-base behavior in aqueous solution: Steric effects make some metal ions hard: A quantitative scale of hardness-softness for acids and bases, Journal of Chemical Education, 73 (1996) 654.

[35] J. Patterson, C. Aracne, D. Jackson, V. Malba, S. Weir, P. Baker, Y. Vohra, Pressure-induced metallization of the Mott insulator MnO, Physical Review B, 69 (2004) 220101.

[36] D.R. Huffman, R. Wild, M. Shinmei, Optical Absorption Spectra of Crystal-Field Transitions in MnO, The Journal of Chemical Physics, 50 (1969) 4092-4094.

[37] V.I. Anisimov, M. Korotin, E. Kurmaev, Band-structure description of mott insulators (NiO, MnO, FeO, CoO), Journal of Physics: Condensed Matter, 2 (1990) 3973.

[38] J. Wu, J. Cao, W.-Q. Han, A. Janotti, H.-C. Kim, Functional metal oxide nanostructures, Springer Science & Business Media, 2011.

[39] P. Tasker, The stability of ionic crystal surfaces, Journal of Physics C: Solid State Physics, 12 (1979) 4977.

[40] J. Van Elp, R. Potze, H. Eskes, R. Berger, G. Sawatzky, Electronic structure of MnO, Physical Review B, 44 (1991) 1530.

[41] C.G. Shull, W.A. Strauser, E.O. Wollan, Neutron Diffraction by Paramagnetic and Antiferromagnetic Substances, Physical Review, 83 (1951) 333-345.

[42] C.T. Campbell, S.M. Valone, Design considerations for simple gas dosers in surface science applications, Journal of Vacuum Science & Technology A: Vacuum, Surfaces, and Films, 3 (1985) 408-411.

[43] Quadrex 200 Technical Manual, Quadrex 200 Technical Manual, Inficon Leybold-Heraeus.

[44] X. Feng, D.F. Cox, Na Deposition on MnO (100), Surface Science, 645 (2016) 23-29.

[45] P.A. Redhead, Thermal Desorption of Gases, Vacuum, (1962) 9.

[46] W. Brown, R. Kose, D. King, Femtomole adsorption calorimetry on single-crystal surfaces, Chemical Reviews, 98 (1998) 797-832.

[47] J. Wellendorff, T.L. Silbaugh, D. Garcia-Pintos, J.K. Nørskov, T. Bligaard, F. Studt, C.T. Campbell, A benchmark database for adsorption bond energies to transition metal surfaces and comparison to selected DFT functionals, Surface Science, 640 (2015) 36-44.

[48] P.E. Blöchl, Projector augmented-wave method, Physical Review B, 50 (1994) 17953-17979.

[49] G. Kresse, D. Joubert, From ultrasoft pseudopotentials to the projector augmented-wave method, Physical Review B, 59 (1999) 1758-1775.

[50] G. Kresse, Efficiency of ab-initio total energy calculations for metals and semiconductors using a plane-wave basis set, Computational Material Science, 6 (1996) 15.

[51] G. Kresse, J. Furthmüller, Efficient iterative schemes for ab initio total-energy calculations using a plane-wave basis set, Physical Review B, 54 (1996) 11169.

[52] G. Kresse, J. Hafner, Ab initio molecular dynamics for liquid metals, Physical Review B, 47 (1993) 558.

[53] J.P. Perdew, K. Burke, M. Ernzerhof, Generalized Gradient Approximation Made Simple, Physical Review Letters, 77 (1996) 3865-3868.

[54] S. Dudarev, G. Botton, S. Savrasov, C. Humphreys, A. Sutton, Electron-energy-loss spectra and the structural stability of nickel oxide: An LSDA+ U study, Physical Review B, 57 (1998) 1505.

[55] C. Franchini, R. Podloucky, J. Paier, M. Marsman, G. Kresse, Ground-state properties of multivalent manganese oxides: Density functional and hybrid density functional calculations, Physical Review B, 75 (2007) 195128.

[56] S. Grimme, Semiempirical GGA-type density functional constructed with a long-range dispersion correction, Journal of Computational Chemistry, 27 (2006) 1787-1799.

[57] S. Grimme, J. Antony, S. Ehrlich, H. Krieg, A consistent and accurate ab initio parametrization of density functional dispersion correction (DFT-D) for the 94 elements H-Pu, The Journal of Chemical Physics, 132 (2010) 154104.

[58] E.R. Johnson, A.D. Becke, A post-Hartree-Fock model of intermolecular interactions: Inclusion of higher-order corrections, The Journal of Chemical Physics, 124 (2006) 174104.

[59] A. Tkatchenko, M. Scheffler, Accurate molecular van der Waals interactions from ground-state electron density and free-atom reference data, Physical Review Letters, 102 (2009) 073005.

[60] P. Bultinck, C. Van Alsenoy, P.W. Ayers, R. Carbó-Dorca, Critical analysis and extension of the Hirshfeld atoms in molecules, The Journal of Chemical Physics, 126 (2007) 144111.

[61] S.N. Steinmann, C. Corminboeuf, A generalized-gradient approximation exchange hole model for dispersion coefficients, The Journal of Chemical Physics, 134 (2011) 044117.

[62] S.N. Steinmann, C. Corminboeuf, Comprehensive benchmarking of a density-dependent dispersion correction, Journal of Chemical Theory and Computation, 7 (2011) 3567-3577.

[63] C.T. Campbell, J.R.V. Sellers, Enthalpies and Entropies of Adsorption on Well-Defined Oxide Surfaces: Experimental Measurements, Chemical Reviews, 113 (2013) 4106-4135.

[64] X. Wu, D. Vanderbilt, D. Hamann, Systematic treatment of displacements, strains, and electric fields in density-functional perturbation theory, Physical Review B, 72 (2005) 035105.

[65] Y. Le Page, P. Saxe, Symmetry-general least-squares extraction of elastic data for strained materials from ab initio calculations of stress, Physical Review B, 65 (2002) 104104.

[66] K.K. Irikura, Experimental vibrational zero-point energies: Diatomic molecules, Journal of Physical and Chemical Reference Data, 36 (2007) 389-397.

[67] Y. Lilach, I. Danziger, M. Asscher, Second order isothermal desorption kinetics, Catalysis Letters, 76 (2001) 35-39.

[68] J.T. Yates Jr, T.E. Madey, Interactions between Chemisorbed Species: H_2 and CO on (100) Tungsten, The Journal of Chemical Physics, 54 (1971) 4969-4978.

[69] E. Farfan-Arribas, R.J. Madix, Characterization of the acid− base properties of the TiO_2 (110) surface by adsorption of amines, The Journal of Physical Chemistry B, 107 (2003) 3225-3233.

[70] P. Atkins, J.d. Paula, Physical chemistry, in, WH Freeman and Company New York, 2006.

[71] M. Sidoumou, V. Panella, J. Suzanne, Interaction of ammonia molecules with the MgO (100) surface: application to the measure of the effective ionic surface charge, The Journal of Chemical Physics, 101 (1994) 6338-6343.

[72] D.E. Starr, C.T. Campbell, Large entropy difference between terrace and step sites on surfaces, Journal of the American Chemical Society, 130 (2008) 7321-7327.

[73] C. Rettner, D. Bethune, E. Schweizer, Measurement of Xe desorption rates from Pt (111): Rates for an ideal surface and in the defect-dominated regime, The Journal of Chemical Physics, 92 (1990) 1442-1457.

[74] G. Szulczewski, J. White, Infrared spectroscopy and photodesorption of condensed phase ammonia, Surface Science, 406 (1998) 194-205.

[75] A. Bolina, W. Brown, Studies of physisorbed ammonia overlayers adsorbed on graphite, Surface Science, 598 (2005) 45-56.

[76] T.A.D. D.P. Woodruff, Modern Techniques of Surface Science - Second Edition, Cambridge University Press, Cambridge, 1994.

[77] G.B. Fisher, The electronic structure of two forms of molecular ammonia adsorbed on Pt (111), Chemical Physics Letters, 79 (1981) 452-458.

[78] M.J. Dresser, A.-M. Lanzillotto, M.D. Alvey, J.T. Yates Jr, Interaction between NH_3 and CO on the Ni (111) and (110) surfaces: A study by ESDIAD, Surface Science, 191 (1987) 1-14.

[79] A.A. Tsyganenko, D.V. Pozdnyakov, V. Filimonov, Infrared study of surface species arising from ammonia adsorption on oxide surfaces, Journal of Molecular Structure, 29 (1975) 299-318.

Chapter 4

Reaction Chemistry of CH_3I on α-$Cr_2O_3(10\bar{1}2)$[2]

4.1 Introduction

The dehydrogenation of methane has garnered a lot of research interests in the catalysis field as it allows for the utilization of abundant natural gas to mass-produce various other hydrocarbons. However, the initial dehydrogenation step of methane is slow and it occurs at a much slower rate than the desorption of CH_4 under vacuum [1-3]. Halogenated hydrocarbons are helpful as they can readily undergo dissociative adsorption, breaking carbon-halogen bonds, even at low temperatures [4-8], which bypasses the slow initial dehydrogenation of CH_4 and gives access to surface methyl groups for reaction studies. One good candidate is CH_3I [5]. UHV is a particularly good environment for studying the decomposition reaction pathways because x-ray photoelectron spectroscopy (XPS) and temperature-programmed desorption (TPD) can potentially identify both the surface binding sites and the elementary surface reaction steps. Within this study is the experimental examination of the decomposition of methyl groups on α-$Cr_2O_3(10\bar{1}2)$ surface using TPD and synchrotron-based XPS, along with the computational examination of the reaction process.

Methyl fragments readily undergo various reactions on metal catalysts. A simple dehydrogenation of the methyl groups to methylene can lead to the production of ethylene (CH_2CH_2) as reported on Cu(110) [9, 10] and Pd(100) [11] through methylene coupling, or on Cu(100) [12] and on Ag(111) [13] through methylene insertion into a methyl group,

[2] TPD data from the PhD dissertation of C.M. Byrd, Reaction chemistry of C_1 hydrocarbon fragments and oxygenates on Cr_2O_3 $(10\bar{1}2)$, Chemical Engineering, Virginia Tech, 2003. XPS data from M. A. Minton and D. F. Cox, unpublished

followed by beta-hydrogen elimination. It has been reported that further dehydrogenation is possible to form acetylene (C_2H_2) on Ni(111) and Al(111) surfaces [14, 15]. If methylene is formed on an oxygenated metal surface, oxygenated hydrocarbons may be synthesized. On oxygen-covered Rh(111) [16] and Pt(111) [17], which have been shown by DFT to have similar bonding with adsorbed oxygen [18], formaldehyde (CH_2O) can be formed by introducing methylene fragments. Further oxidation of the methylene to CO, CO_2, and water is also possible on metal surfaces, such as Pd(100), Pt(100), Ru(111), and Ru(001) [11, 17, 19, 20].

Methyl fragments can also lead to a range of products on metal-oxide surfaces. For example, CO, CO_2, CH_3OH, and CH_2O can be formed on V_2O_5 through a methoxide intermediate [21]. Similar reaction products can be produced on TiO_2(110) [22]. The reaction of methyl groups was also investigated on α-Cr_2O_3(0001), where methyl fragments undergo dehydrogenation, and form ethylene either through direct coupling of methylene or through methylene insertion into a surface methyl group to form an ethyl group, followed by β-hydride elimination to produce ethylene [5].

The reaction mechanism involving methylene on the $(10\bar{1}2)$ surface were also studied by Byrd [23] using TPD, revealing that after the dissociative adsorption of CH_2I_2, producing CH_2= on the surface, reaction products CH_2=CH_2 and CH_4 are formed. The reaction-limited desorption of CH_2=CH_2, which is the result of the surface diffusion and coupling of the CH_2= groups, is observed at 390 K during TPD[23]. Synchrotron XPS clearly identifies the binding site of CH_2= to be surface cations on the $(10\bar{1}2)$ surface [24].

4.2 $Cr_2O_3(10\bar{1}2)$

α-Cr_2O_3 has the corundum structure and is an insulator with a band gap of 3.4 eV [25, 26]. The crystal structure is predicated on "a hexagonal close packed array of O^{2-} ions, with two-thirds of the interstitial octahedral sites filled by Cr^{3+} ions" [27]. The bulk electronic structure is antiferromagnetic, with ferromagnetic Cr^{3+} sheets having alternating net spins in the direction perpendicular to the $(10\bar{1}2)$ surface [28].

A previous study characterizing α-$Cr_2O_3(10\bar{1}2)$ [29] using XPS, Auger electron spectroscopy (AES), and low-energy electron diffraction (LEED) established that after ion bombardment followed by annealing in ultra-high vacuum at 900 K, a nearly-stoichiometric (1×1) surface can be prepared that is characteristic of a simple termination of the bulk structure. The ideal surface is illustrated in figure 4-1. The $(10\bar{1}2)$ surface has a rectangular periodicity ($a:b = 0.94$) [29] and is the most thermodynamically stable of all the low-index surfaces [30]. Previous work by Tasker [31] suggest that a stable surface is terminated with a repeating unit of layers that is both neutral in dipole moments and in charge. For α-$Cr_2O_3(10\bar{1}2)$, the repeat unit perpendicular to the surface is arranged as [O^{2-}, Cr^{3+}, O^{2-}, Cr^{3+}, O^{2-}]. The O^{2-} anions in the top atomic layer are three-fold coordinated, while the second layer Cr^{3+} cations five-fold coordinated, resulting in one degree of coordinative unsaturation with respect to the bulk [32]. As figure 4-1 (b) shows, the top layer anions appear in zig-zag rows in the $[02\bar{2}1]$ direction, separated by troughs exposing fully-coordinated lattice oxygens in the third atomic layer.

4.3 Methods

4.3.1. Experimental methods

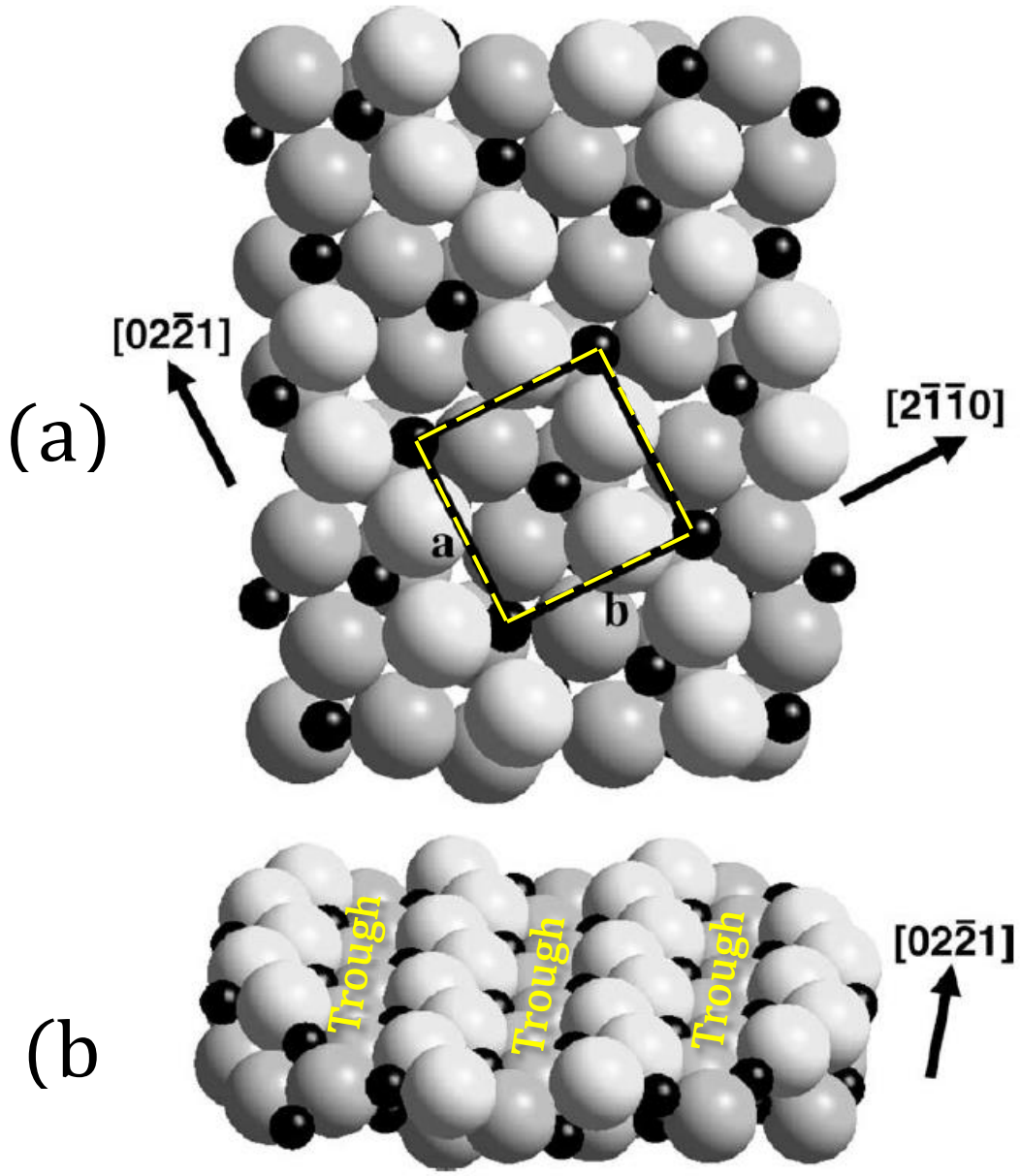

Figure 4-1 A ball model representation of the α-Cr_2O_3 (10$\bar{1}$2). Figure (a) is the top view, showing the (10$\bar{1}$2) surface parallel to the plane of the page. Surface periodicity is illustrated with a surface unit cell drawn in yellow dashed line. a:b = 0.94. Figure (b) shows a slanted view of one stoichiometric repeating layer. Small, black spheres represent Cr^{3+} cations, large, light spheres represent O^{2-} anions. Figure adapted with permission from Brooks, et al. (2009).

All TPD experiments were carried out in an ultra-high vacuum chamber with an ion pump that maintains a base pressure of 1×10^{-10} torr. The chamber includes a Physical Electronics model 15-555 single-pass CMA for Auger electron spectroscopy, and an Inficon Quadrex 200 mass spectrometer for TPD. The chamber is also equipped with Princeton Research Instruments model RVL 8-120 reverse-view LEED optics. AES is used to establish the cleanliness of the surface, and to examine the relative amount of the post-reaction halogen residuals on the surface. LEED was used to confirm the (1×1) periodicity characteristic of a simple termination of the bulk. The sample preparation procedure includes 2000 eV argon ion bombardment, followed by a period of annealing at 900 K which produces a nearly-stoichiometric surface [29].

Iodomethane (CH_3I, Aldrich, 99.5% and CD_3I, Aldrich, 99.5%) was purified by flash distillation. All doses are corrected for ion gauge sensitivity, and mass spectrometer sensitivity factors were determined experimentally.[3] A glass skimmer on the mass spectrometer is used to minimize signal collection from non-sample surfaces. A linear temperature ramp of 2.5 K/s is used for TPD. The heating rate is limited to this low value as the sample is ceramic and susceptible to thermal shock. The relative amounts of products were determined through the comparison of the integrated areas of the TPD traces.

Soft x-ray photoelectron spectroscopy (XPS) spectra were obtained at the U12a beamline at the National Synchrotron Light Source, Brookhaven National Laboratory. Photoemission spectra were collected at an instrumental resolution of 0.5 eV, and all spectra are referenced to a Cr $2p_{3/2}$ binding energy of 576.9 eV [29, 33]. Compensation for

[3] An ion gauge sensitivities of 9.48 used for methyl iodide was calculated using a correlation by S. George reported in R. L. Brainard and R. J. Madix, *J. Am. Chem. Soc.*, 111 (1989) 3826. Mass spectrometer sensitivity factors for ethylene (m/z=27 and 28), formaldehyde (m/z=30), methane (m/z=16), hydrogen (m/z=2), water (m/z=18), formic acid (m/z=46), carbon dioxide (m/z=44), CH_3I (m/z=142) and CD_3I (m/z=145) were 0.64, 1.04, 0.64, 1.53, 1.91, 0.56, 0.057, 1.22, 0.045 and 0.16, respectively.

surface charging during the XPS was accomplished using 0.5 eV electrons generated by a Gammadata Scienta FG-300 flood gun. The operating base pressure for the system was 1×10^{-10} torr.

The orientation of the α-Cr_2O_3 crystal was set to within 1° of the $(10\bar{1}2)$ surface using Laue back-reflection. It was then polished to a final mirror finish with 0.25 μm diamond paste. In both chambers, the sample was held in place through mechanical clamps onto a tantalum stage. The stage was fastened to LN_2-cooled copper electrical conductors to serve as the heating platform for the sample. To allow for temperature measurements, a type K thermocouple was attached to the back of the sample through the hole in the tantalum support using Aremco #569 ceramic cement.

4.3.2. Computational methods

Simulations were performed using the projector-augmented-wave method [34, 35] in the Vienna Ab-initio Simulation Package (VASP)[36-38]. PBE functionals which utilize a standard generalized gradient approximation (GGA), were used to treat the exchange and correlation in the electronic system [39]. An 80-atom slab, which consists of two stoichiometric units along $[10\bar{1}2]$, is used, exposing a (2×2) surface mesh. A vacuum gap of 15 Å is used to separate the slabs. For all calculations, the k-point sampling was generated using a Monkhorst-Pack scheme [40]. A $3\times1\times3$ mesh was used for all calculations. The atoms in the lower repeat unit were fixed in their bulk positions, while the atoms in the upper five atomic layers were free to move during the geometric relaxation. For geometric relaxations, forces were required to be less than 0.01 eV/Å upon convergence. The initial magnetic moments are set per the known antiferromagnetic ordering in α-Cr_2O_3 [28]. In DFT, this ordering is also the ground-state magnetic ordering [41]. The minimum energy

pathway (MEP) for methyl dehydrogenation was investigated using the climbing-image nudged elastic band method (CI-NEB) [42-44]. The reaction prefactors are calculated by dividing the product of the all the normal frequencies for the initial state by that of the transition state, excluding the one imaginary frequency [45]. The zero-point energy correction for each activation barrier is calculated by assuming the harmonic oscillator approximation [46], which is done by first acquiring the difference between the sum of the real frequencies of the transition state and the sum of all frequencies of the initial states, and then multiplying by one half of the Planck's constant [45]. For frequency calculations, the forces are less than 0.0005 eV/ Å, and are done using a mass of 2 atomic mass unit (amu) for hydrogen in accordance with the experimental use of deuterated reactants.

The prediction of electronic properties of strongly-correlated transition metal oxide such as α-Cr_2O_3 is widely-known to be problematic for DFT [41]. One approach to address this problem that has found significant use in the literature is the inclusion of an on-site Coulomb repulsion, i.e., the +U method [47, 48]. A set of parameter values ($U = 5.0$ and $J = 1.0$) are used to strike a balance between the bulk structural properties and the electronic properties, although this does not guarantee optimal results for surface properties [41]. The DFT+U method used was developed by Dudarev et al. [48].

4.4 Results and discussion

The reaction of CD_3I on the α-$Cr_2O_3(10\bar{1}2)$ surface leads to the production of two major gas-phase, carbon-containing products, CD_4 and $CD_2{=}CD_2$, in addition to residual surface iodine adatoms. Several m/z signals were monitored simultaneously during the TPD experiment, and then compared to the established mass spectrometer fragmentation

patterns for the identification of the supposed product molecules. For the reactant CD_3I, a m/z signal of 142 was used to track the desorption of the dosed CD_3I molecule. m/z = 32, 30, and 28 were used for track $CD_2{=}CD_2$, and m/z = 20 and 18 for CD_4. Contributions from the reactant CD_3I in the product signals were eliminated by subtracting the m/z=142 signal, using the established fragmentation pattern of the reactant CD_3I. Other possible products were excluded by examining the m/z values in the range between 2-200 on the mass spectrometer. No production of CD_3-CD_3, CO, CO_2, or gas phase I_2 was observed. The absence of the oxygenated species, such as CO and CO_2, confirms the non-reducibility of the surface, as previous characterization work has shown [29].

4.4.1. Thermal Desorption on $Cr_2O_3(10\bar{1}2)$ surface

Figure 4-2 shows the desorption traces after a small dose of 0.1 L (1 L ≡1×10^{-6} Torr·sec) of CD_3I on a clean, freshly prepared, nearly-stoichiometric α-Cr_2O_3 $(10\bar{1}2)$ surface at 100 K. The small dose size of 0.1 L was intentionally selected not only to minimize the potential effect of the adsorbed iodine on the reaction, but also to reduce the contribution of the fragmentation signal from unreacted CD_3I during the TPD experiments.

Desorption products CD_4, $CD_2{=}CD_2$, and D_2 are detected in a high temperature envelope extending from about 400 to 600 K. The primary desorption feature of CD_4 is asymmetric, peaks at 518 K and tails to the lower temperature side. A small desorption feature of CD_4 is also seen at 120 K, and is due to the desorption of physisorbed methane from the uptake of background CD_4 formed in the ion pump. The desorption feature for $CD_2{=}CD_2$ is symmetric, and peaks at 518 K. The desorption feature of D_2 peaks at a slightly higher temperature of 540 K and is also asymmetric that tails to lower temperatures with a small shoulder at 420 K, and. The desorption of the molecular reactant CD_3I is seen at 300

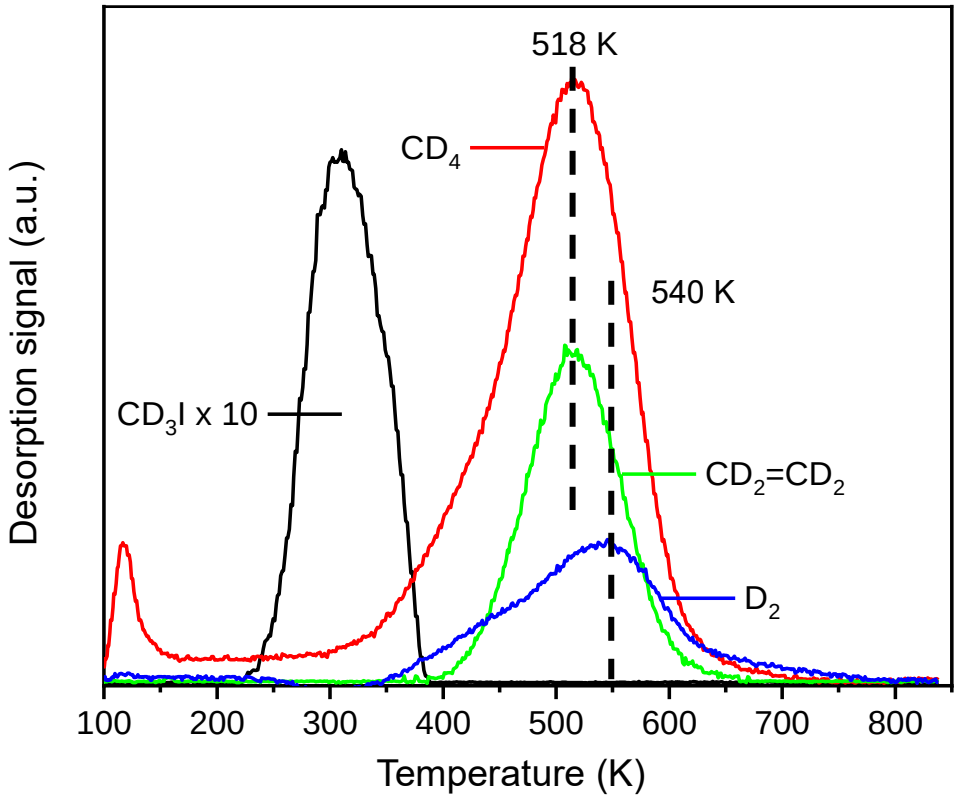

Figure 4-2 The temperature-programmed desorption traces for a 0.1 L CD_3I on the nearly-stoichiometric surface.

K. The selectivity on the C_1 basis is 57±5% for CD_4 and 43±5% for CD_2=CD_2. Separate TPD experiment shows that multilayer iodomethane desorption occurs at 140 K for large doses (not shown). Other TPD experiment with varying initial coverages of CD_3I shows that the 518 K peak of the CD_4 desorption feature is invariant with coverage. Post-reaction AES could not determine the amount of residual iodine on the surface, as the I AES signal overlaps with Cr LMM feature from the substrate. The presence of residual iodine is observed in the XPS and is discussed below.

The distinct asymmetry of the desorption feature for CD_4 with a peak at 518 K and the invariance of the peak desorption temperature with coverage are both indicative of a first-order process [49] Taking into account that dosed molecular D_2, and CD_2=CD_2 are observed to desorb from the stoichiometric surface at near 285 K in separate TPD experiments [23], we conclude that the desorption features for D_2, CD_2=CD_2, and CD_4 that peak above 500 K are all surface reaction limited. Desorption of all three products fall within the same temperature envelope which indicates they originate from a common surface intermediate with the same rate-limit step. Further, because the diffusion and coupling of surface methylene groups are observed with a desorption peak temperature of 390 K [23], lower than the that of the products observed in figure 4-2, the rate-limiting step for ethylene formation is not the surface diffusion and coupling of methylene. Given the product slate, the observed chemistry is readily described by the first-order dehydrogenation of surface methyl groups as the rate-limiting elementary reaction step. In the first step (1), the surface methyl group undergoes α-hydrogen elimination in the rate-limiting step (RLS). This is followed by the coupling of the two migratory methylene groups

to form $CD_2{=}CD_2$ (2). Alternatively, the cleaved hydrogen can combine with remaining methyl groups to recombinatively form CD_4 gas (3).

$$\text{-}CD_{3\,(ads)} \rightarrow {=}CD_{2\,(ads)} + \text{-}D_{\,(ads)} \quad \text{(RLS) (1)}$$

$$2\ \text{-}CD_{2(ads)} \rightarrow CD_2{=}CD_{2\,(gas)} \quad (2)$$

$$\text{-}D_{(ads)} + \text{-}CD_{3\,(ads)} \rightarrow CD_{4\,(g)} \quad (3)$$

The desorption feature at 518 K translates to an activation barrier of 135 ± 2 kJ/mol for the rate-limiting step using a Redhead first-order analysis [49] and assuming a reaction prefactor of $1{\times}10^{13}$ sec^{-1}. The errors arise from an accuracy of ± 5 K in the experimental temperature measurements. The lack of production of CD_3-CD_3 indicates that the coupling of methyl groups does not occur. This observation implies that the surface mobility of -CD_3 is poor, and that the reaction barrier for the migration and coupling of -CD_3 is higher than that for the dehydrogenation of -CD_3 groups. Also implied is that the formation of CD_4 on the surface is the likely the result of surface migration of -D to couple with -CD_3 groups, and not vice versa.

Figure 4-3 shows the integrated areas for various desorption species with consecutive 0.1 L CD_3I dose. As the cumulative (total) dose of CD_3I increases, a dramatic decrease in the integrated areas for the reaction products is observed. The products drop off rapidly for cumulative doses up to 0.5 L. CD_3I desorption steadily increases by about 3.4 times the initial amount as the surface deactivates. The "total" amount in figure 4-3 is the summation of integrated desorption signal for all hydrocarbon species on a C_1 basis. The deactivation of the surface (as indicated by a drop in product formation) is due to the accumulation of the iodine on the surface, as its deposition is a result of the dissociation of methyl iodide (see XPS below). The decrease in the total carbon evolved as gas phase

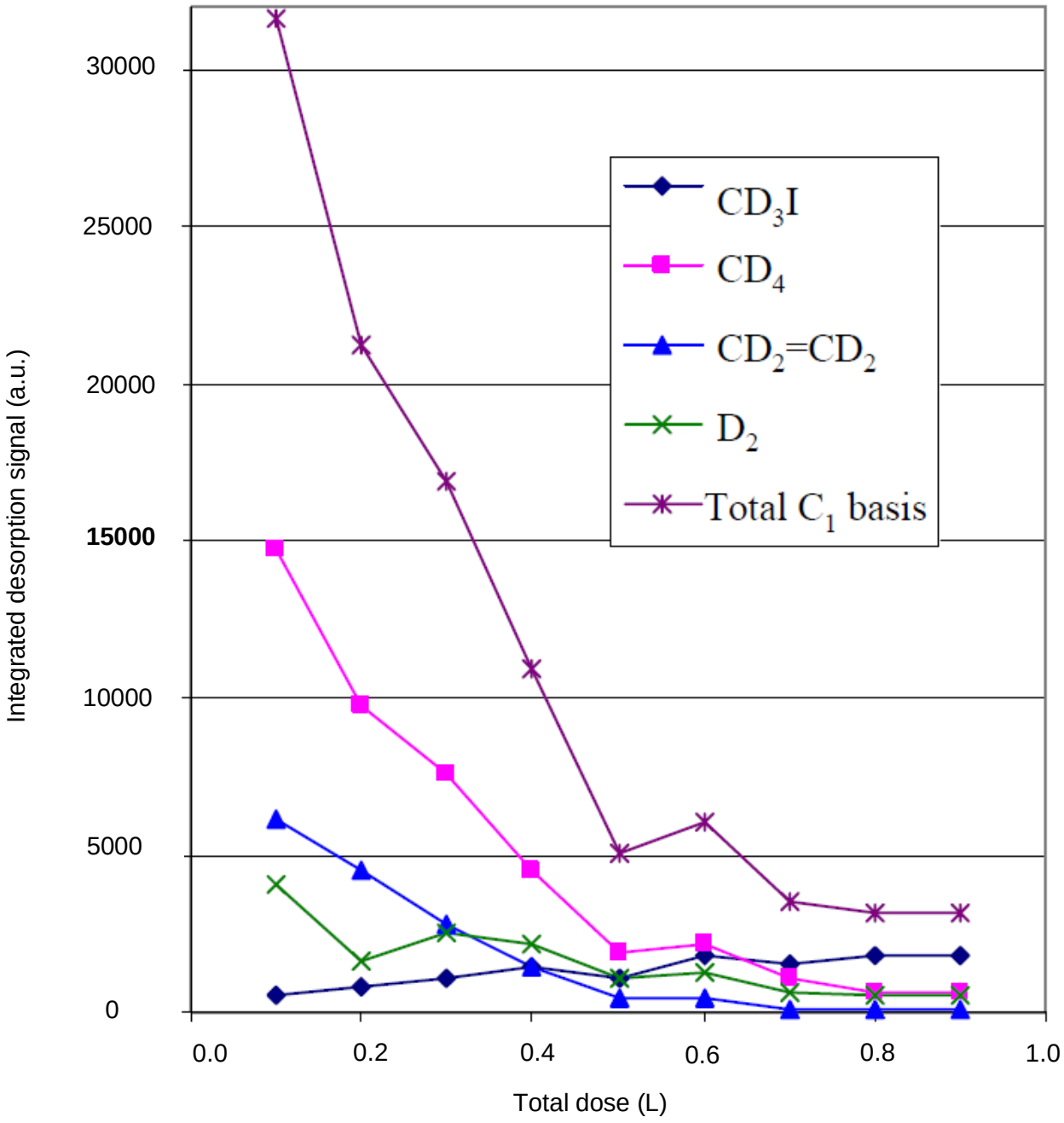

Figure 4-3 Integrated area of the desorption traces for consecutive 0.1 L CD_3I doses on the nearly-stoichiometric surface. The total is the sum of all carbon species on a C_1 basis.

products with consecutive dose indicates a decrease in the methyl iodide sticking coefficient as I coverage increases.

Figure 4-4 shows the change in selectivity for CD_4 and $CD_2{=}CD_2$ on a C_1 basis with consecutive 0.1 L CD_3I doses. The selectivity for CD_4 increases from 57% to 80% as cumulative doses (and consequently, iodine coverage) increases. In comparison, the production of $CD_2{=}CD_2$ is reduced to 20%. The phenomenon of the decreasing reactivity and a shift to higher selectivity for CD_4 suggests that the while iodine deposition tends to deactivate the surface, it more effectively hinders the diffusion of the methylene groups than the diffusion of surface deuterium, resulting in higher selectivity to CD_4 for higher cumulative doses.

Similar reaction energetics and mechanism have been reported on the $Cr_2O_3(0001)$ surface, where the rate-limiting step of α-hydrogen elimination is also identified [5]. On the (0001) surface, the rate-limiting methyl dehydrogenation process peaks at a temperature of 490 K for an activation barrier of 129 kJ/mol [5] (which is slightly less than 135 kJ/mol) and indicative of a lack of structure sensitivity in the activation energy. For product selectivity, the selectivity for $CD_2{=}CD_2$ over CD_4 decreases with increasing cumulative doses increases on the $(10\bar{1}2)$ surface, but remains relatively constant on (0001) surface [5].

4.4.2. Synchrotron XPS

Figure 4-5 shows C 1s synchrotron photoemission results ($h\nu = 350$ eV) for a nearly-stoichiometric surface after a 30 L dose of CH_3I. To obtain the XPS spectrum, the

sample is dosed at 120 K, then annealed at the respective temperature for 60 seconds, and allowed to

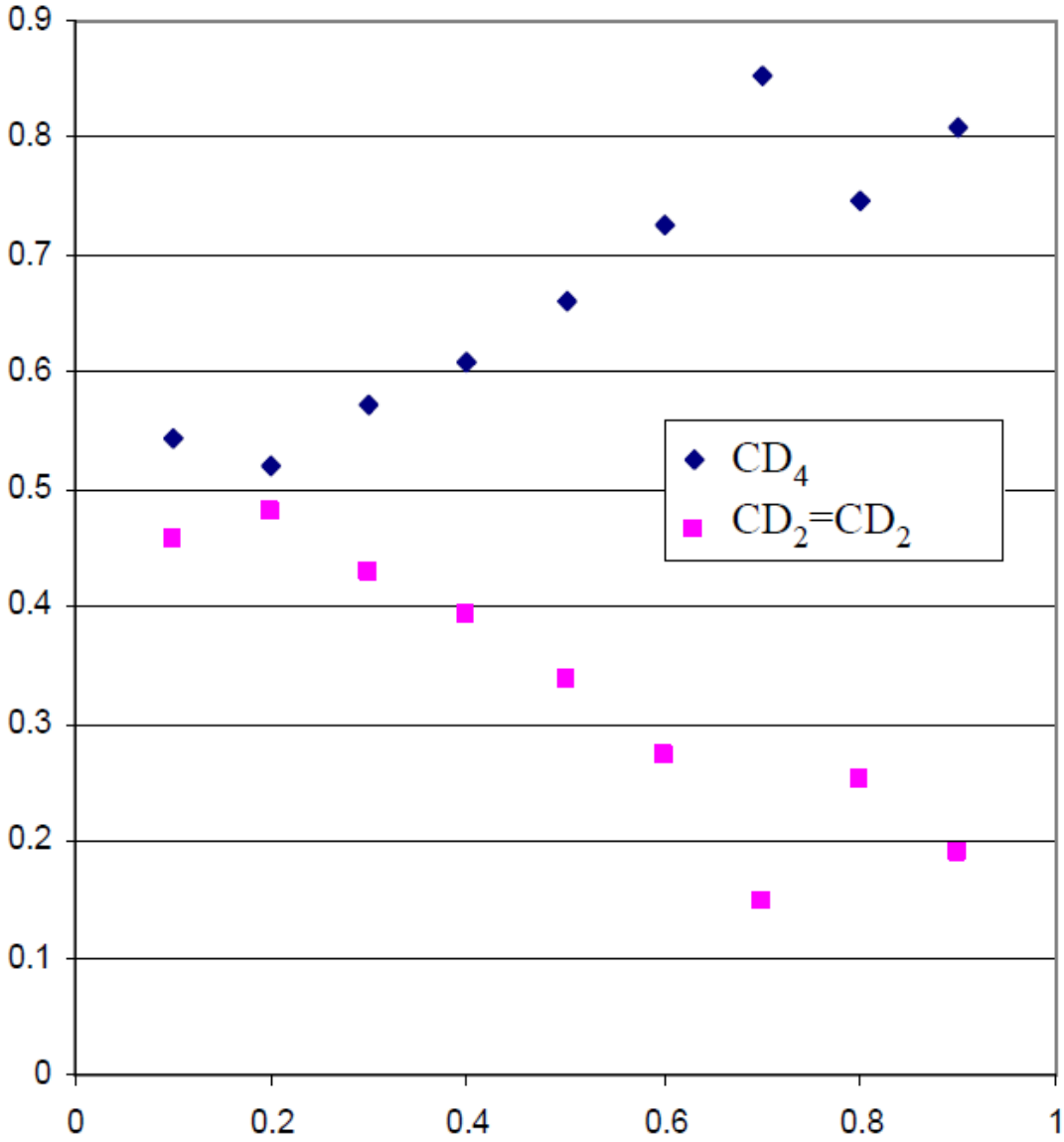

Figure 4-4 Selectivity of desorption products on a C_1 basis for consecutive 0.1 L CD_3I doses on the nearly-stoichiometric surface.

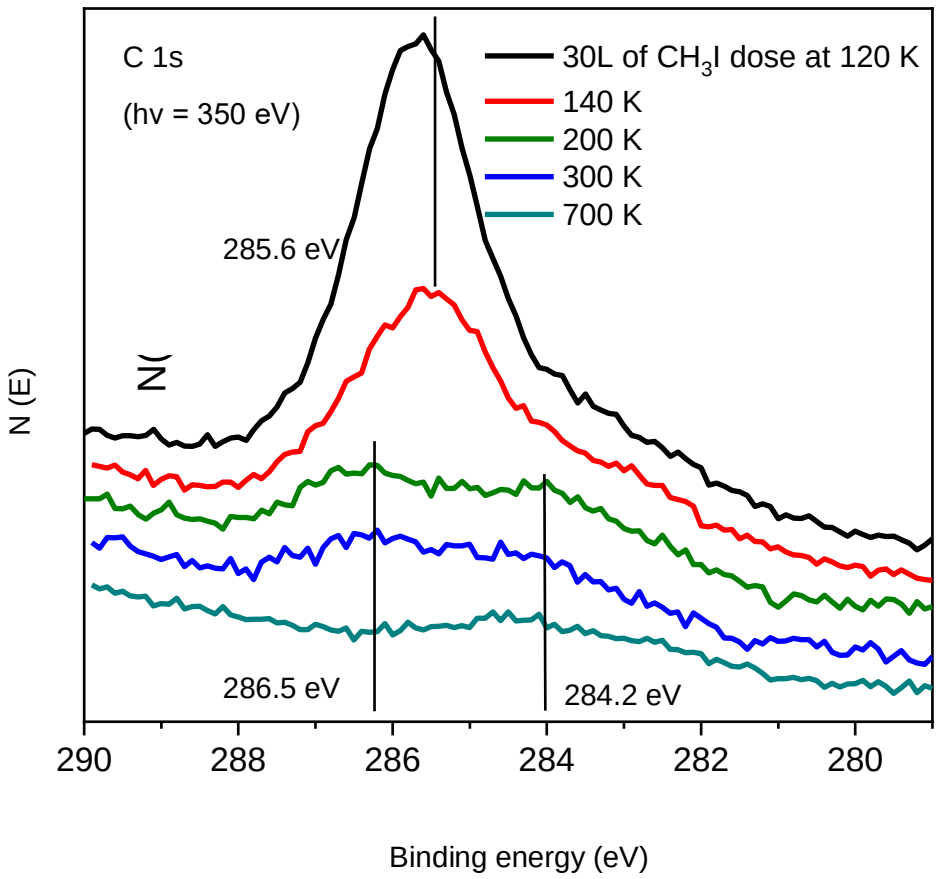

Figure 4-5 Synchrotron XPS photoemission of the C 1s spectra after a saturation dose of CH_3I and then annealing at various temperatures. 120 K is the dosing temperature. Temperatures shown in the legend for each spectrum is the annealing temperature applied before the XPS spectrum is collected. The 286.5 eV signal is attributed to C 1s signal on oxygen site, and the 284.2 eV signal is attributed to C 1s signal at metal site.

cool to 120 K before collecting photoemission spectra. The TPD experiments have shown that dosing 30 L of CH_3I at 120 K results in multilayer coverage, and thus provides a spectrum with characteristics of molecular methyl iodide.

Shown as a black line is the spectrum collected directly after the sample is dosed with 30 L of iodomethane at 120 K. This spectrum shows a primary feature with a binding energy of 285.6 eV. As the annealing temperature is raised to 140 K, the multilayer desorbs and the intensity of the primary feature attenuates, while showing a small shoulder to the low binding energy side. When the annealing temperature is raised further to 200 K, the primary feature at 285.6 eV splits into two separate and smaller features at 286.5 eV and 284.2 eV. At the annealing temperature of 300 K (the desorption peak temperature for molecular CH_3I in figure 4-2), the two features persist. At 700 K (a temperature above all product peaks in TPD experiments), the 286.5 eV feature disappears, leaving only a broad feature around 284 eV.

The primary feature at 285.6 eV at lower temperatures is attributed to the iodized C 1s signal of the molecular CH_3I. This assignment is supported by the similar observations of binding energy in the literature: at 285.0 eV for molecular CH_3I on $Cr_2O_3(0001)$ [5], and 285.6 eV for CD_3I on $TiO_2(110)$ [50]. The attenuation of the primary signal at 285.6 eV and the splitting into two features at 200 K suggest that the multilayer has desorbed, revealing two different adsorption configurations of methyl on the surface, following C-I bond scission (see iodine XPS discussion below). The 286.5 feature is attributed to the binding of methyl fragments at a surface oxygen site, as binding energies above 286.0 eV are usually associated with methoxy (CH_3-O-) groups [51, 52]. In comparison, the 284.2 eV feature is assigned to the cation-bound methyl groups [53]. Increasing the annealing temperature to

300 K removes all molecular species (figure 4-2), and the two peaks remain largely unchanged (to 286.5 eV and 284.4 eV), indicating that surface methyl is stable in this temperature range at both binding sites. This is also affirmed by our finding from the TPD experiments, as the dehydrogenation of methyl groups occurs at higher temperatures. At an annealing temperature of 700 K, the 286.5 eV peak feature disappears, and a broad low binding energy feature remains, indicating that some trace residual carbon is left at the surface cation sites.

Figure 4-6 shows the spectra of I $3d_{5/2}$ using a photon energy of 750 eV. A feature at 621.4 eV is observed following adsorption at 120 K, characteristic of molecular methyl iodide with an intact C-I bond, along with a small shoulder at 619.9 eV. As the annealing temperature is raised to 140 K, the primary feature decreases in intensity, and a feature at 619.5 eV becomes more apparent. As the annealing temperature increases to 200 K, the molecular feature at 621.4 eV is nearly completely removed, while the 619.5 eV peak remains.

In figure 4-6, the primary peak of 621.4 eV at 120 K is assigned to the I $d_{5/2}$ signal from the molecular CH_3I with an intact C-I bond. This assignment is consistent with reported binding energies at around 620 eV [5, 54-56]. The peak with lower binding energy (619.6 eV) is characteristic of a metal iodide [5, 56], and indicates the residual surface I binds at cation sites and poisons the surface reaction. From the I $3d_{5/2}$ feature, it is clear that C-I bond breaking is nearly complete by 200 K, leaving I adatoms and methyl intermediates on the surface.

4.5 Computational results and discussion

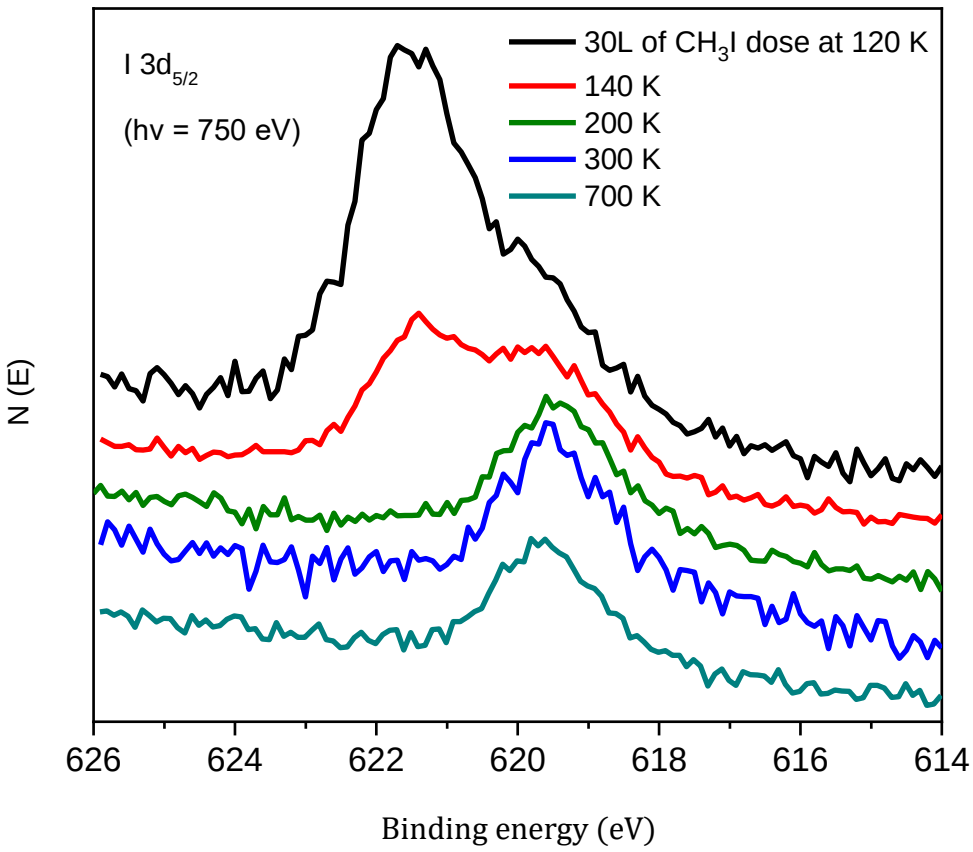

Figure 4-6 Synchrotron XPS photoemission (hν = 750 eV) of the I 3d spectra after a 30L dose of CH_3I and then annealing applied at various temperatures. 120 K is the dosing temperature. Temperatures shown in the legend for each spectrum is the annealing temperature applied before the XPS spectrum is collected.

DFT is used to examine both the binding sites of the different surface intermediates for comparison to the experimental XPS results, and to examine the energetics of the rate-limiting, elementary, methyl dehydrogenation (α-hydrogen elimination) step observed in TPD. DFT (PBE) and DFT+U (PBE+U) is used and compared in all cases. Additionally, the energetics of the rate-limiting elementary surface reaction step has been examined in the presence and in the absence of I adatoms. TPD experiments show that the activation barrier for the reaction is insensitive to the surface coverage of iodine adatoms, therefore the reaction of isolated methyl fragments in the absence of iodine has been considered as a base case. However, it is noted that the use of methyl iodide as a reactant precludes an iodine-free experimental situation, since the dissociative adsorption of methyl iodide is expected to yield a methyl group and an iodine adatom on neighboring sites. Hence, both situations (with and without I) have been examined to provide insight into the role of surface iodine adatoms in the simulations.

4.5.1. DFT-predicted binding sites for methyl and methylene intermediates

Geometry optimization of the CH_3- and CH_2= were done on various sites in the 80-atom unit cell of $(10\bar{1}2)$ surface using PBE and PBE+U to explore the binding sites of these intermediates. The PBE simulations show stable minima for CH_3- binding at both cation and anion sites, with binding at surface cations being the most stable, but only by a small energy difference of 0.2 eV. The PBE+U simulation shows that CH_3- binding is more stable at a surface anion than a cation site by 1.0 eV.

In comparison to the experimental results, PBE provides the more reasonable prediction because the small energy difference between binding at cation and anion sites is consistent with the experimental observation of both sites by XPS. The difference of 0.2 eV predicted by PBE is small enough to reasonably explain the co-existence of CH_3- at both sites. In contrast, PBE+U predicts a stronger adsorption of CH_3- at an anion site by 1.0 eV, which would likely lead to methyl species bound primarily at anion sites (methoxy species), which is inconsistent with the XPS observations.

Simulations of methylene (CH_2=) binding, both with PBE and PBE+U, predicts a minimum energy sp^3 binding configuration of CH_2= bridging between a surface cation and a coordinately-unsaturated nearest-neighbor anion (see below) rather than the expected sp^2 configuration for a cation-bound methylene seen experimentally in XPS. PBE slightly favors the bridged sp^3 configuration (by 0.6 eV), while it is strongly favored by PBE+U by 1.7 eV. Since XPS gives a clear indication that CH_2= binds at surface cations on the $(10\bar{1}2)$ surface, both PBE and PBE+U predicted the wrong binding configuration for methylene fragments on the surface.

Considering the disagreement between the XPS results and the DFT predictions regarding the binding configurations of CH_3- and CH_2=, we separate our results and discussion on DFT reaction energetics into two parts. Section 4.5.2 examines the DFT predictions for reaction energetics using the experimentally determined binding sites as a basis for the simulation, while section 4.5.3 and 4.5.4 feature the DFT reaction energetics using the binding sites predicted by PBE and PBE+U, respectively.

4.5.2. DFT reaction energetics with experimentally observed binding sites for the methyl and methylene intermediates

The dehydrogenation of methyl groups in accordance with the experimentally observed binding sites for the carbon-containing intermediates was examined using the climbing-image nudged elastic band (cNEB) method [42-44, 57] for the case with no I adatoms. The minimum energy pathways (MEPs) for the dehydrogenation reaction and the transition state were determined using the cNEB implementation in VASP after geometrically optimizing a cation-bound CH_3- on the 80-atom slab for the initial state, and a cation-bound CH_2= with a hydrogen adatom on the adjacent anion as the final state in accordance with the experimental XPS results. The initial and final states are illustrated in Figure 4-7. Note that the initial state binding of methyl is consistent with the minimum energy configuration predicted by PBE, and matches the experimental binding site. The final state binding site for methylene, while consistent with experiment is **not** the minimum energy binding configuration in PBE. The geometries of the same basic initial and final states used for PBE+U are shown in figure 4-8. Note that neither the methyl or methylene binding sites in figure 4-8 are the minimum energy configurations for PBE+U, although these sites are used to mimic the binding sites determined experimentally. No noticeable geometric differences are observed between the PBE and PBE+U initial and final states using the experimentally determined binding sites.

Figure 4-9 (a) to (d) shows the geometries of the transition state determined by PBE and PBE+U, using the initial and final states shown in figure 4-7 and figure 4-8. The corresponding minimum energy pathways (MEPs) are shown in figure 4-9 (e) and (f) for PBE and PBE+U, respectively. As figures 4-9 (a) and (c) show, PBE predicts that in the

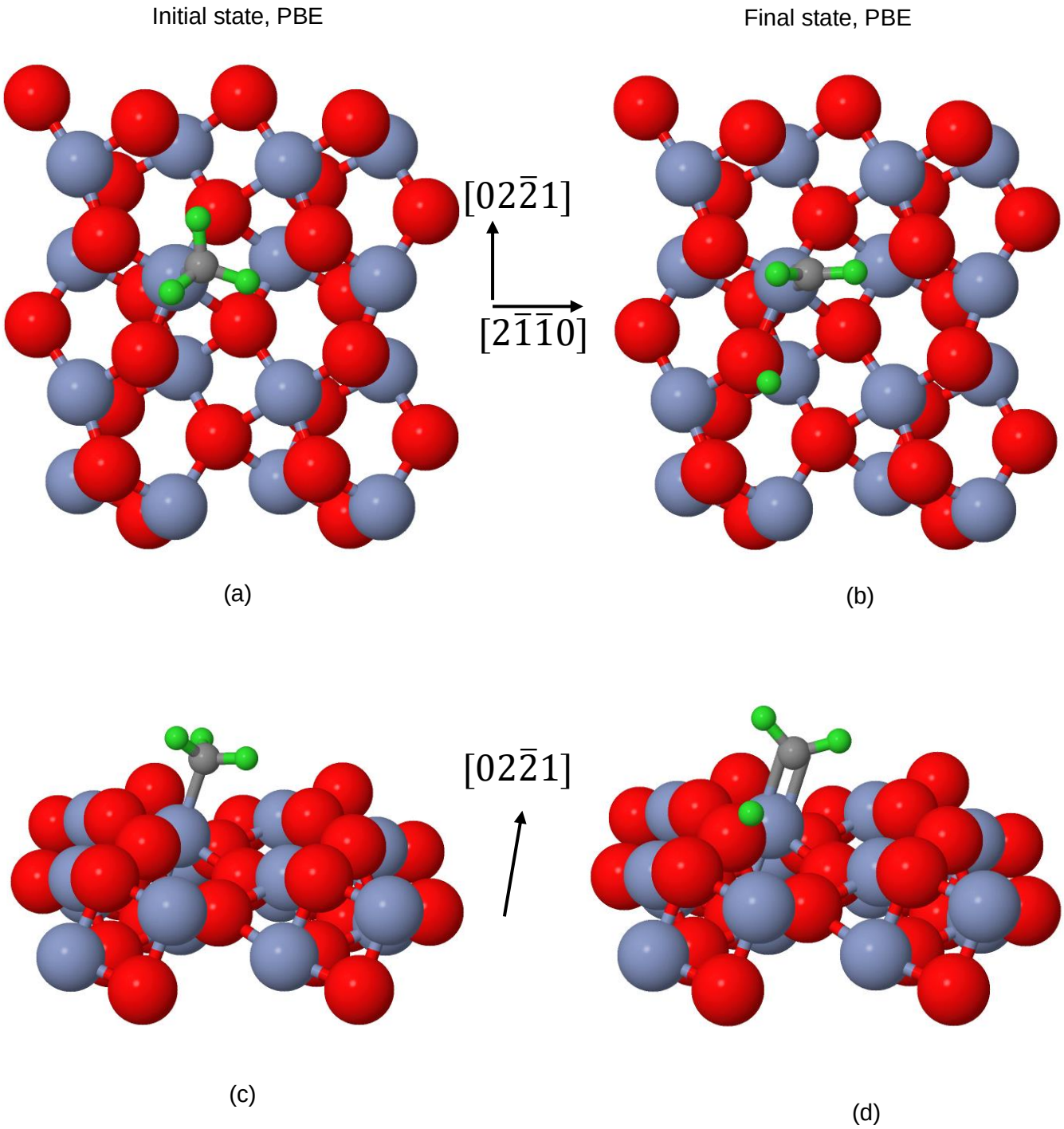

Figure 4-7 The images of initial state (a and c) viewed in two direction, and final state (b and d) viewed in two directions of the α-hydrogen elimination step of CH_3- on (10$\bar{1}$2) surface, as predicted by PBE functional using experimentally observed adsorption sites for carbon species. (a) and (b) are in top view while (c) and (d) are in a slanted view of the surface. Chromium cations are in light blue, oxygen atoms are in red, carbon atom is in grey, hydrogen in green. Surface directions are also labeled.

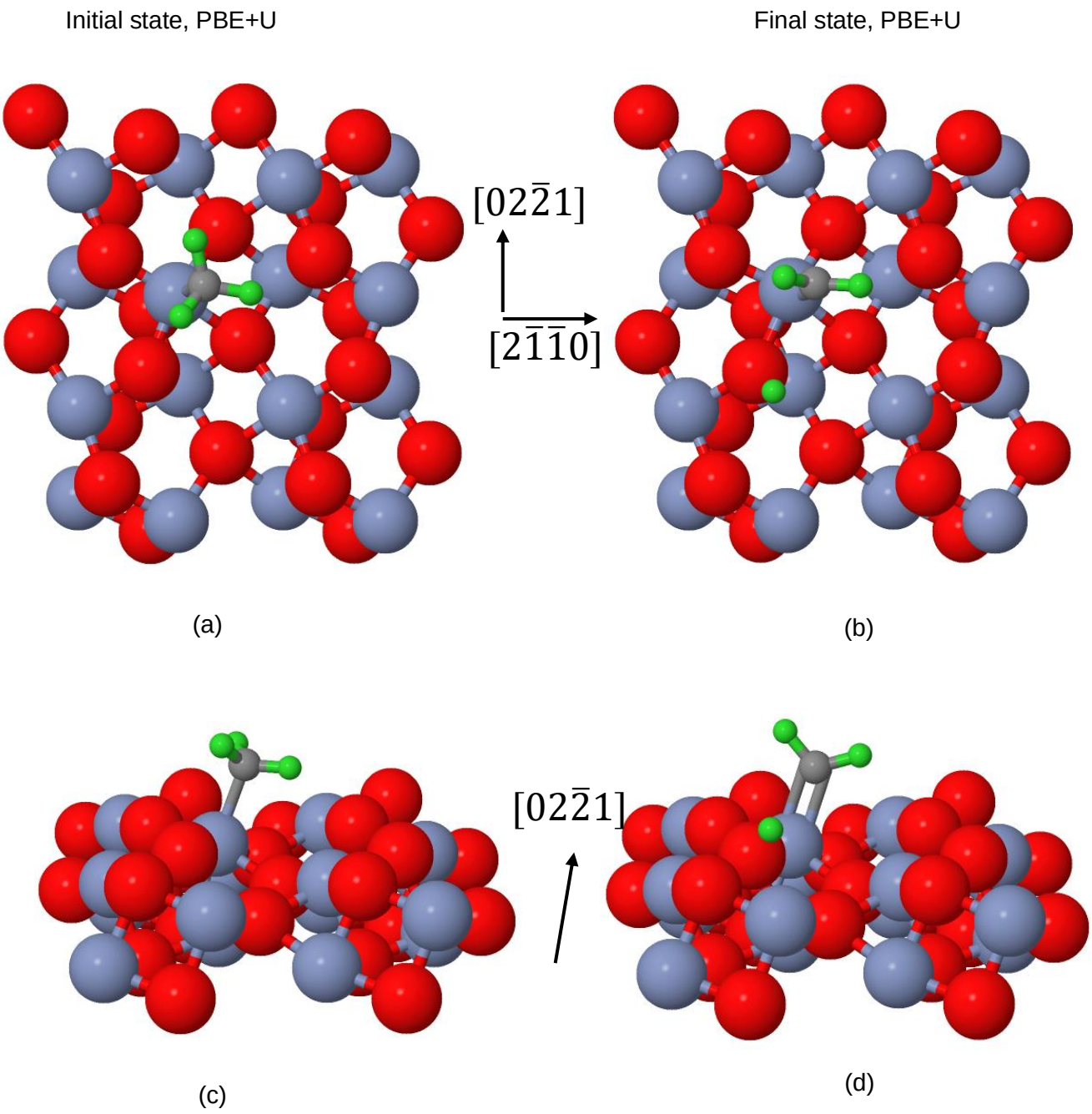

Figure 4-8 The images of initial state (a and c) viewed in two direction, and final state (b and d) viewed in two directions of the α-hydrogen elimination step of CH_3- on (10$\bar{1}$2) surface, as predicted by PBE+U functional using experimentally observed adsorption sites for carbon species. (a) and (b) are in top view while (c) and (d) are in a slanted view of the surface. Chromium cations are in light blue, oxygen atoms are in red, carbon atom is in grey, hydrogen in green. Surface directions are also labeled.

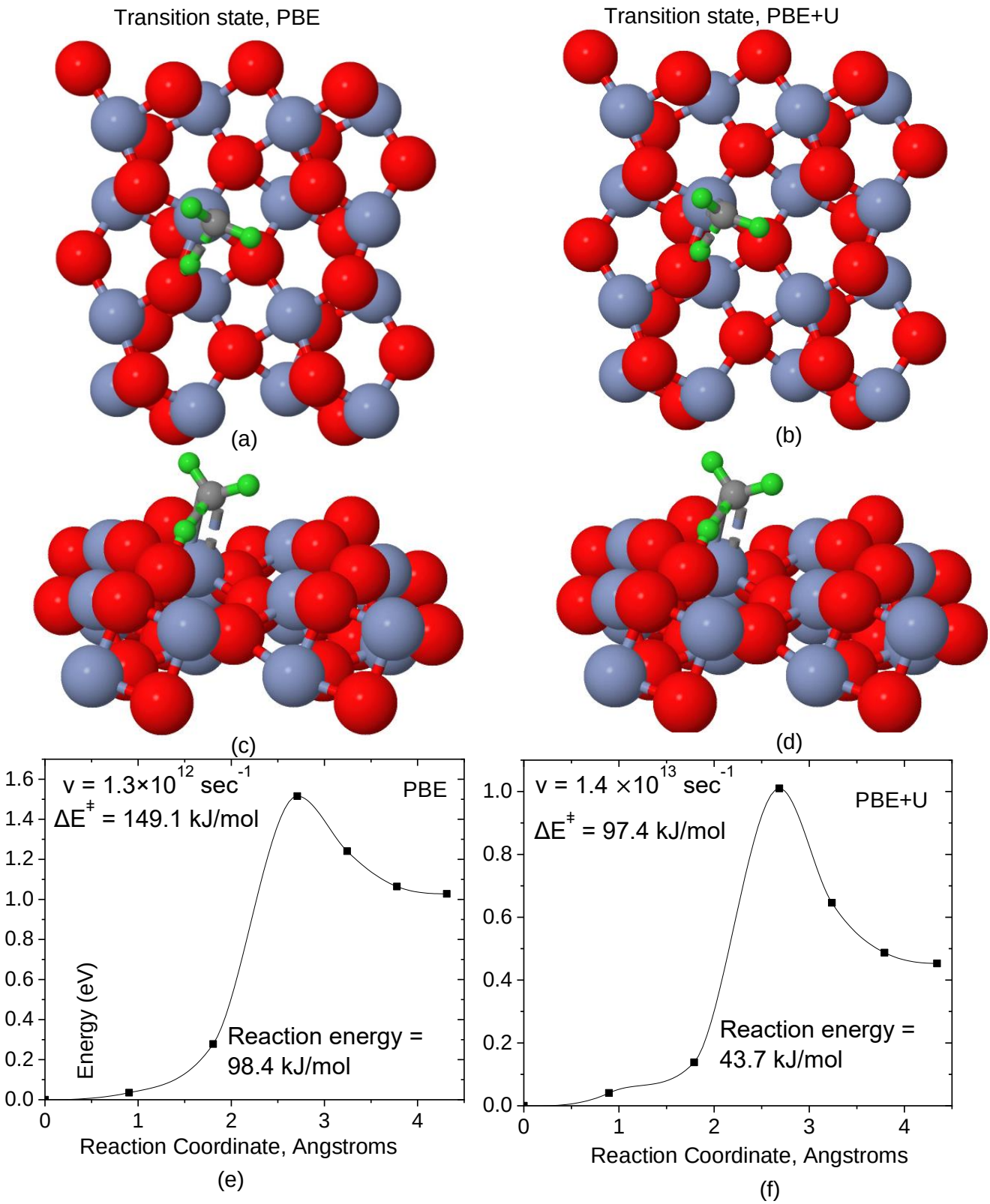

Figure 4-9 The transition states of the α-hydrogen elimination step of CH_3- on $(10\bar{1}2)$ surface as predicted by PBE (a and c) and PBE+U (b and d), respectively. Subplots a and b are in top view, while c and d are in a slanted view. The minimum energy pathway (MEP) of the reaction, as predicted by PBE and PBE+U, are shown in e and f, respectively. Activation barriers ($\Delta E^{\ddagger}$), reaction prefactor ν, and reaction energies are labeled.

transition state the cleaved hydrogen is closer to the adjacent oxygen than to the α carbon with a nearly sp^2 hybridization for carbon at the transition state. Figure 4-9 (b) and (d) show the transition state of the α-hydrogen elimination of CH_3- as predicted by PBE+U. No obvious geometric differences are observed between PBE and PBE+U transition states. The MEPs associated with the reactions (figure 4-9 (e) and (f)) show that PBE predicts an activation barrier of 1.52 eV (149.1 kJ/mol) with an endothermic reaction energy of 1.02 eV (98.4 kJ/mol), while PBE+U predicts an MEP with an endothermic reaction of 43.7 kJ/mol and an activation barrier of 97.4 kJ/mol. Frequency analysis for the reaction step using PBE and PBE+U gives one imaginary frequency in each case as expected for the transition state. Prefactors determined from the PBE and PBE+U normal frequencies are 1.3×10^{12} sec^{-1} and 1.4×10^{13} sec^{-1}, respectively. Zero-point energy corrections are also calculated based on the obtained frequencies. The post-correction activation barriers as predicted by PBE and PBE+U become 139.3 kJ/mol and 86.3 kJ/mol. The predicted energies are compared in table 4-1 along with the experimental activation barrier.

In the absence of iodine adatoms and using and using the fragment binding sites determined experimentally, PBE accurately predicts the reaction barrier post-correction, deviating only 3% from the experimental value, while PBE+U underestimates by 36%. PBE is undoubtedly the success story, beating the expectation that PBE+U is supposed to perform better than PBE since +U offers better treatment of the highly-correlated electronic structure. The prefactors determined by PBE and PBE+U are both within one order of magnitude from the assumed value of 1×10^{13} sec^{-1} used to determine the experimental activation barrier for CH_3- dehydrogenation, and affirms the validity of the assumption.

Figure 4-10 shows the initial and final states for α-hydrogen elimination from a methyl group with an adjacent I adatom present as simulated by PBE. PBE predicts binding of the I adatom on a cation site as observed experimentally, with methyl and methylene in the initial and final state, respectively, showing little difference in geometry to that in Figure 4-8 in the absence of I. PBE+U predicts a molecular CH_3I adsorbate with at least a 2 eV barrier to dissociation as the rate limiting step, so the simulation of dehydrogenation of CH_3- in the presence of I using experimental binding sites via PBE+U is not shown.

Figure 4-11 (a) and (b) shows the geometries of the transition state from two viewing angles as determined by PBE using the initial and final states shown in figure 4-10. The corresponding minimum energy pathways (MEPs) are shown in figure 4-11 (c) for PBE. With an iodine adatom at a cation center adjacent to the methyl binding site, PBE predicts a transition state geometry similar to that observed in the absence of I. For the PBE case, the MEP in figure 4-11 (c) is similar in shape to the PBE case without iodine. The reaction barrier decreases from 149.1 kJ/mol to 135.2 kJ/mol, and the endothermic reaction energy decreases from 98.4 kJ/mol to 47.6 kJ/mol. The prefactors for this case is 2.3×10^{12} sec^{-1}.

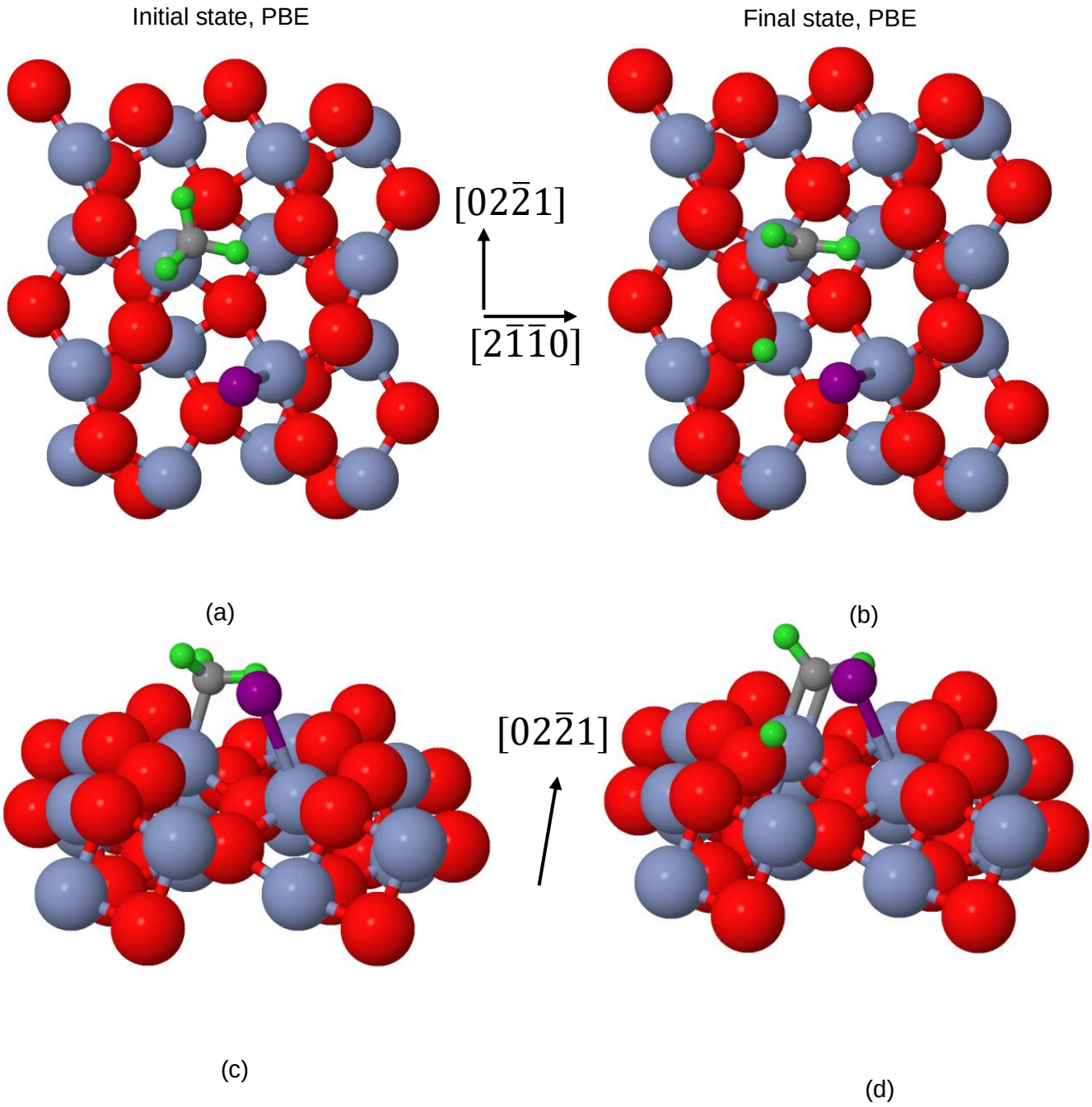

Figure 4-10 The images of initial state (a and c) viewed in two direction, and final state (b and d) viewed in two directions of the α-hydrogen elimination step of CH_3- on (10$\bar{1}$2) surface with I present on the adjacent cation, as predicted by PBE functional using experimentally observed adsorption sites for carbon species. (a) and (b) are in top view while (c) and (d) are in a slanted view of the surface. Chromium cations are in light blue, oxygen atoms are in red, carbon atom is in grey, hydrogen in green. Surface directions are also labeled.

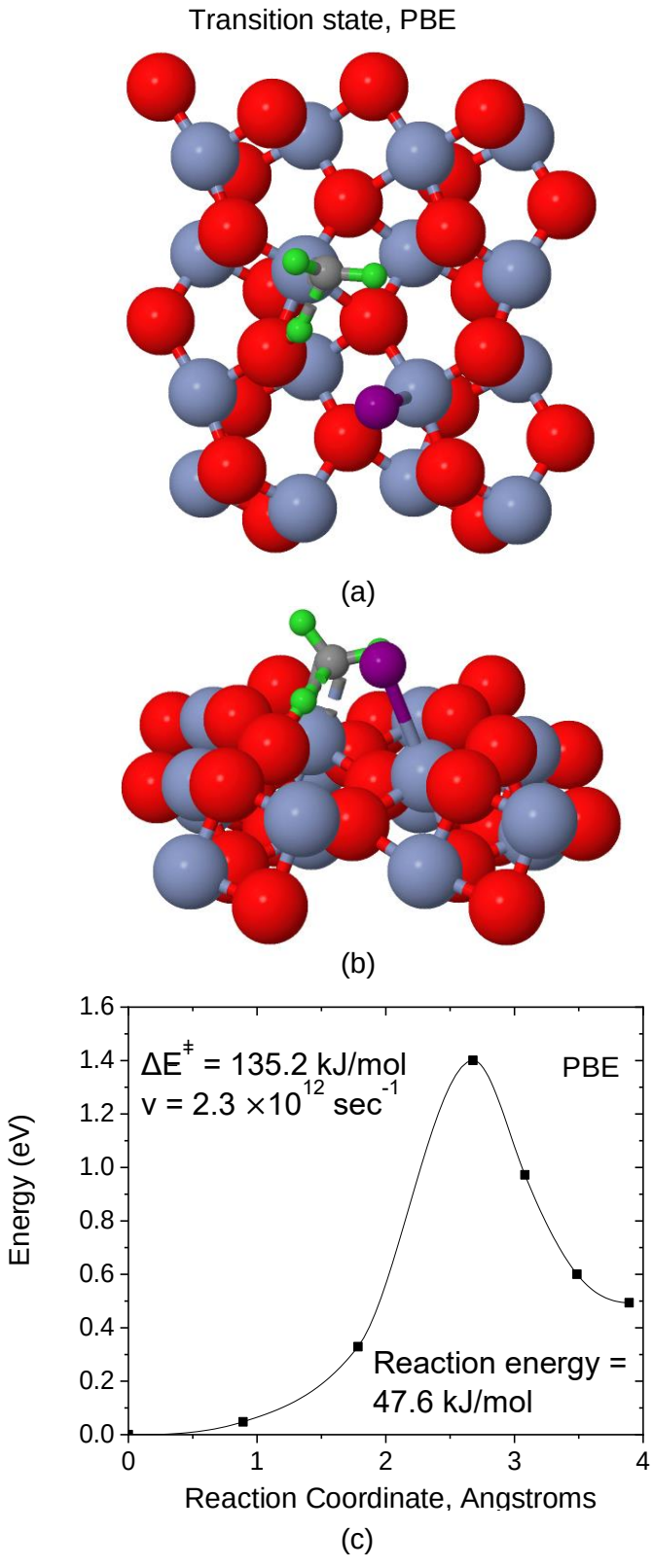

Figure 4-11 The transition states of the α-hydrogen elimination step of CH_3- on $(10\bar{1}2)$ surface as predicted by PBE (a and b). Subplot a is in top view, while b is in a slanted view. The minimum energy pathway (MEP) of the reaction, as predicted by PBE, is shown in c. Activation barriers ($\Delta E^{\ddagger}$), reaction prefactor ν, and reaction energies are labeled.

The introduction of an iodine adatom has an observable impact on the reaction energetics in the case of PBE. Post-correction, the simulated reaction barrier for α-hydrogen elimination is 125.5 kJ/mol with I present, and deviates -7% from the experimental reaction barrier, which is a slightly worse result than the 3% error with I absent. The large barrier of C-I bond-breaking (at least 2eV) for the molecular CH_3I as predicted by PBE+U suggests that this method predicts the wrong rate limiting step. Therefore it is reasonable to ignore the reaction geometries of the dehydrogenation of CH_3- in the presence of I and the associated MEP as predicted by PBE+U. While PBE+U is often considered a preferred method for highly correlated transition metal oxide systems, it fails dramatically in this specific case compared to PBE. We again note that in all of the cases considered so far, the initial and final states for the reaction simulations have been based on the experimentally-determined binding sites for methyl and methylene intermediates, not the minimum energy configurations predicted by the simulations alone.

4.5.3. PBE reaction energetics with simulated minimum-energy binding configurations for methyl and methylene intermediates

In section 4.5.3, all the simulations were based on experimentally-determined cation binding sites for the methyl and methylene intermediates. However, as described in section 4.5.1, both PBE and PBE+U predict a minimum energy bridging configuration for methylene between an adjacent surface cation and anion, while PBE+U predicts a strong preference for methyl binding to O anion sites. Since computational studies are often undertaken without any available experimental benchmarks, it seems prudent also to carry out the simulations using minimum energy binding sites for the initial and final states estimated without regard to the experimental findings. This section considers only the case

for PBE simulations, with the following section, 4.5.4, considers the case for PBE+U simulations.

Figure 4-12 shows the initial and final states for the dehydrogenation of a methyl group as predicted by PBE using the simulated minimum-energy binding configurations for methyl and methylene species. In the initial state CH_3- binds at a surface cation. In the final state, the methylene is in the bridged binding configuration between a cation and a nearest neighbor O anion giving an sp^3-like carbon center. The addition of an I adatom on the adjacent cation does not result in observable differences in the geometry of the methyl (initial state) or methylene (final state), and thus are not shown here.

Figure 4-13 shows the geometry of the transition state as predicted by PBE. Similar to the structures in figure 4-9 (a) and (c), PBE predicts that in the transition state the H atom to undergo C-H bond cleavage is closer to the adjacent oxygen than the α carbon. The remaining CH_2= appears to be in a nearly sp^2 hybridization at the transition state. The addition of an I adatom on the adjacent cation did not result in discernable geometric differences, and thus is not shown here. Figure 4-13 (c) shows the MEP for the simulation without an I adatom which gives an activation barrier of 146.4 kJ/mol with an endothermic reaction energy of 92.1 kJ/mol. Figure 4-13 (d) shows the MEP for the reaction with an I adatom is present on the adjacent cation. The activation barrier is slightly lower, 134.9 kJ/mol in the presence of I. More noticeable, the addition of iodine changes the reaction from endothermic to slightly exothermic, with a reaction energy of -8.1 kJ/mol. Post-correction, PBE predicts the activation barriers to be 136.2 and 124.7 kJ/mol for the I-

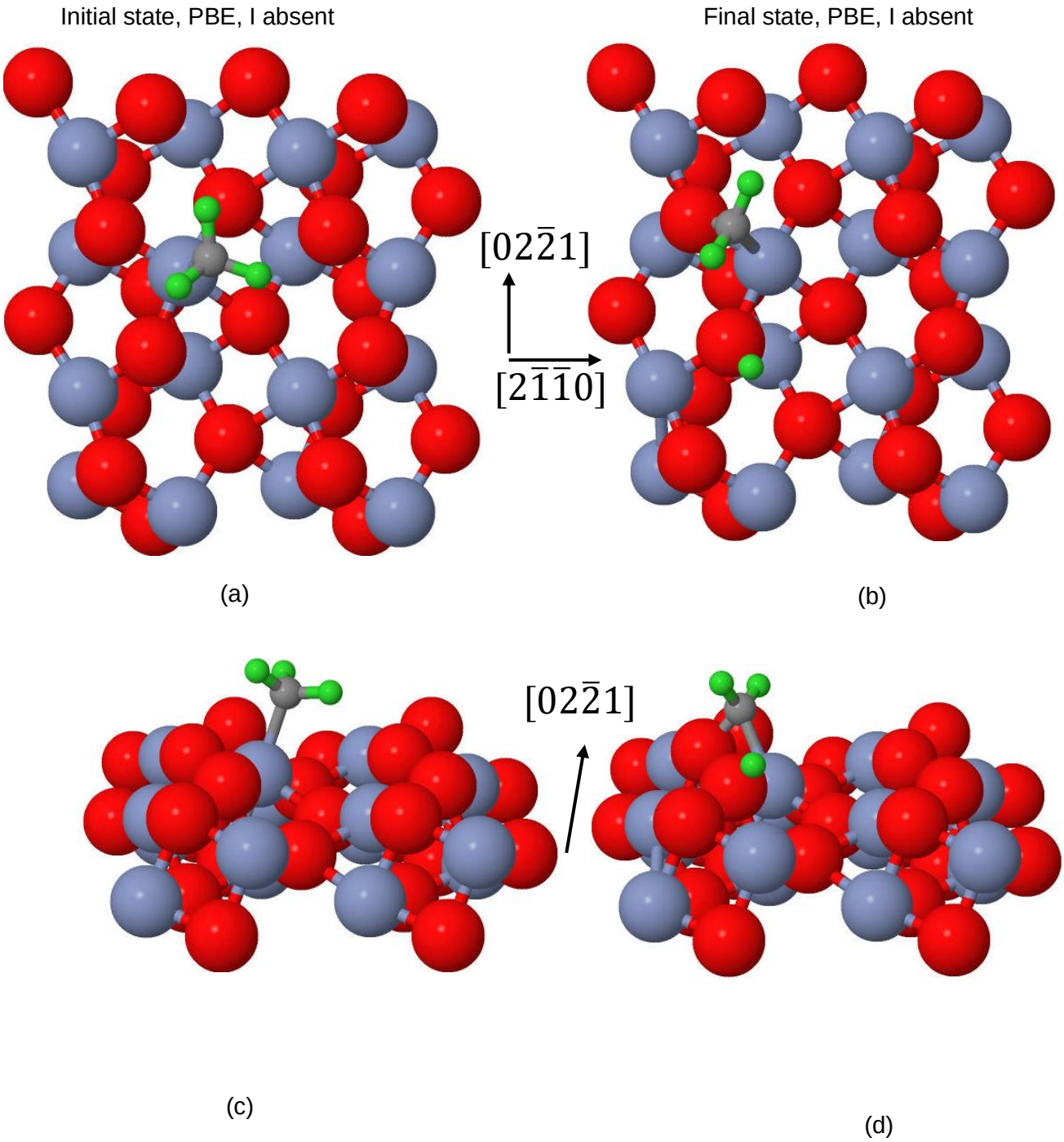

Figure 4-12 The images of the initial, and final states from cNEB calculations of the α-hydrogen elimination step of CH_3- on (10$\bar{1}$2) surface, using PBE-predicted adsorption configurations. Computation functional used for cNEB is PBE.

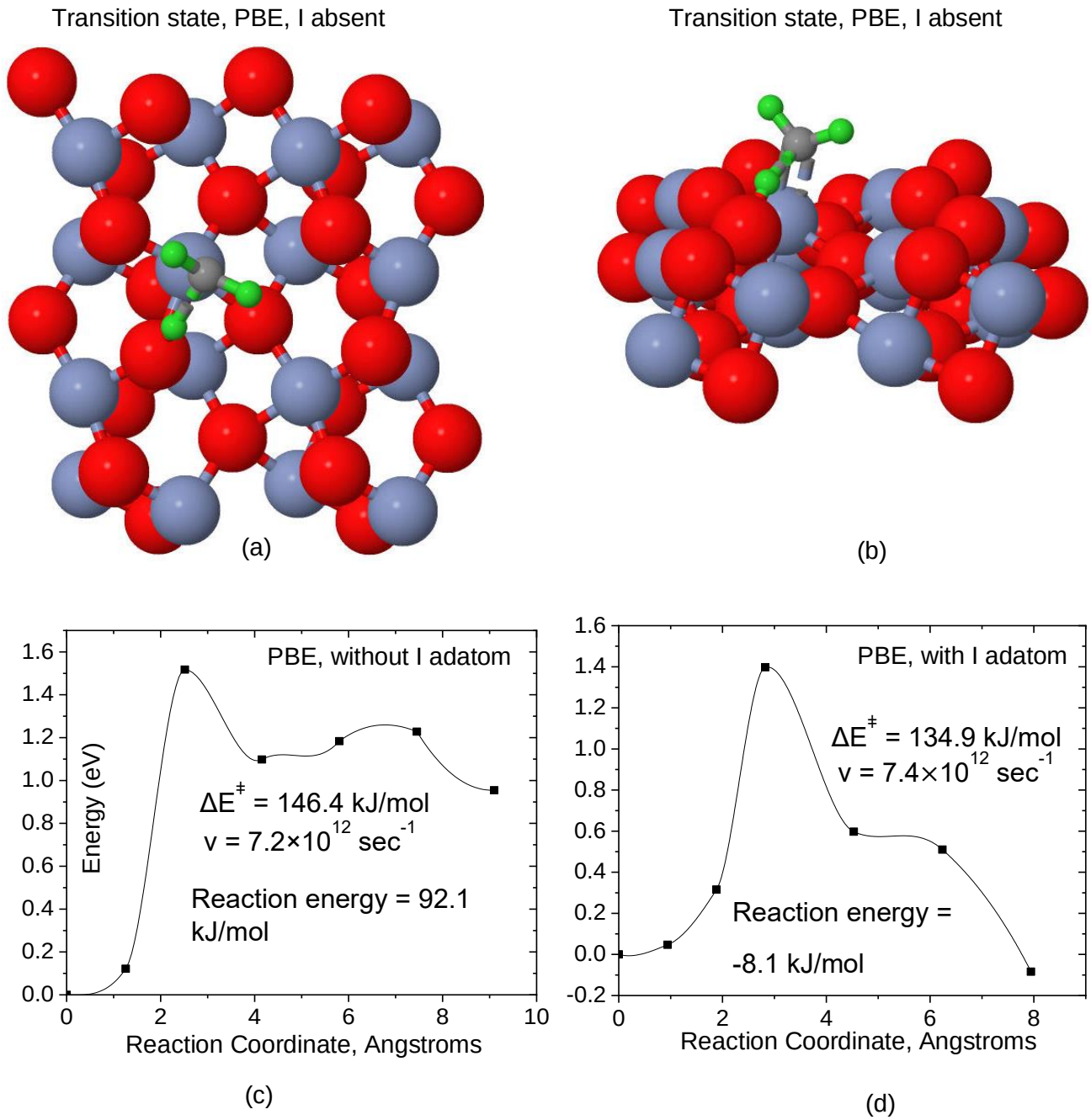

Figure 4-13 The reaction coordinates of the α-hydrogen elimination of a methyl group to form a methylene and a hydrogen on α-Cr_2O_3 $(10\bar{1}2)$, using PBE-predicted adsorption configurations for methyl and methylene. Iodine adatom is absent in the first MEP but is present in the second. Reaction barriers ($\Delta E^{\ddagger}$) and reaction energies are labeled.

absent and I-present cases. The prefactors are 7.2×10^{12} sec^{-1}, and 7.4×10^{12} sec^{-1}, respectively. The reaction barriers are also listed in table 4-2 for comparison purposes.

Even though the final states for methylene predicted here do not match the experimental observations, the ability for methylene to alternate between sp^2 and sp^3 as it moves across the surface has been demonstrated: a previous DFT study showed that methylene undergoes a "thermally-driven" rehybridization between sp^2 and sp^3 as it moves across $Cr_2O_3(0001)$ surface to combine into ethylene molecules [4]. Recall also that methylene migration and recombination is proposed in our reaction mechanism (step 2), and the methylene sp^3 hybridization between an anion and cation shown here would appear along the reaction coordinate for methylene diffusion.

Comparing the simulation results obtained here using simulated and experimentally determined binding configurations for the methylene intermediate, the PBE activation barriers (139.3 kJ/mol by PBE using experimental binding sites, and 136.2 kJ/mol by PBE using PBE-predicted binding sites), are very similar despite the differences in the final states because of the similarity in the initial state and transition state. When an iodine adatom is present on the adjacent cation, the reaction barrier decreases by a 11.5 kJ/mol to 124.7 kJ/mol, deviating about 7 % from the experimentally determined reaction barrier, which is within chemical accuracy. Overall, these simulations demonstrate that PBE provides and accurate estimate of the activation barrier with the inclusion of an I adatom, and is insensitive to minor changes in binding of the methylene intermediate in the final state.

4.5.4. PBE+U reaction energetics with simulated minimum-energy binding configurations for methyl and methylene intermediates

The simulations reported in section 4.5.3 were repeated with PBE+U using the predicted minimum energy binding configurations for methyl and methylene intermediates. Figure 4-14 shows the initial and final states for the dehydrogenation of the methyl as predicted by PBE+U from the top and the slanted viewing angles. In the initial state, the CH_3- is bound at a surface oxygen. In the final state, the methylene takes a bridging conformation between adjacent cations and surface oxygen anions, resulting in an sp^3 hybridization. When an I adatom is introduced on an adjacent cation, no significant geometric differences are observed in the geometries of the initial and final states configurations for methyl and methylene, therefore the initial and final state geometries with I present are not shown.

Figure 4-15 (a) and (b) show the transition state as predicted by PBE+U in accordance with the initial and final states as shown in figure 4-14. At the transition state, the leaving hydrogen atom atom is closer to the adjacent oxygen than to the α carbon. The carbon center appears to be in sp^3-like hybridization at the transition state on top of the surface oxygen. When I adatom is introduced, no significant changes are observed to the reacting species in the transition state, therefore the transition state with an I adatom is not shown. The MEP from figure 4-15 (c) is generated in the absence of iodine, and shows that PBE predicts a reaction barrier of 166.3 kJ/mol with an endothermic reaction energy of 68.0 kJ/mol. Figure 4-15 (d) shows the addition of an iodine adatom on the adjacent cation increases the predicted reaction barrier increases to 188.1 kJ/mol while decreasing the endothermic reaction energy to 59.4 kJ/mol (table 2) Post-correction, the activation barriers are 157.5 kJ/mol as predicted by PBE+U without I present, and 178.0 kJ/mol with I present..

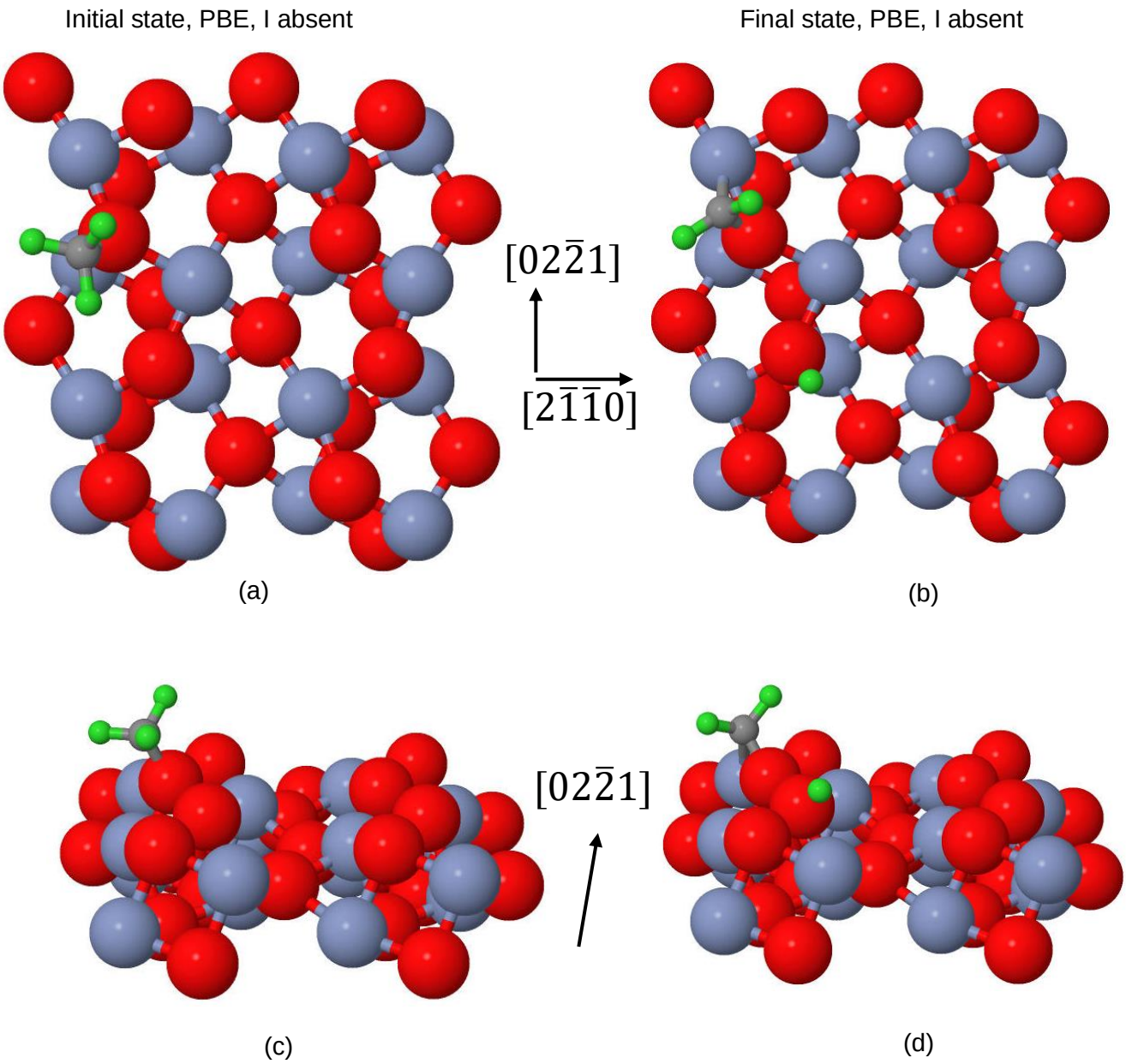

Figure 4-14 The images of the initial, and final states from cNEB calculations of the α-hydrogen elimination step of CH_3- on (10$\bar{1}$2) surface, using PBE+U-predicted adsorption configurations. Computation functional used for cNEB is PBE+U.

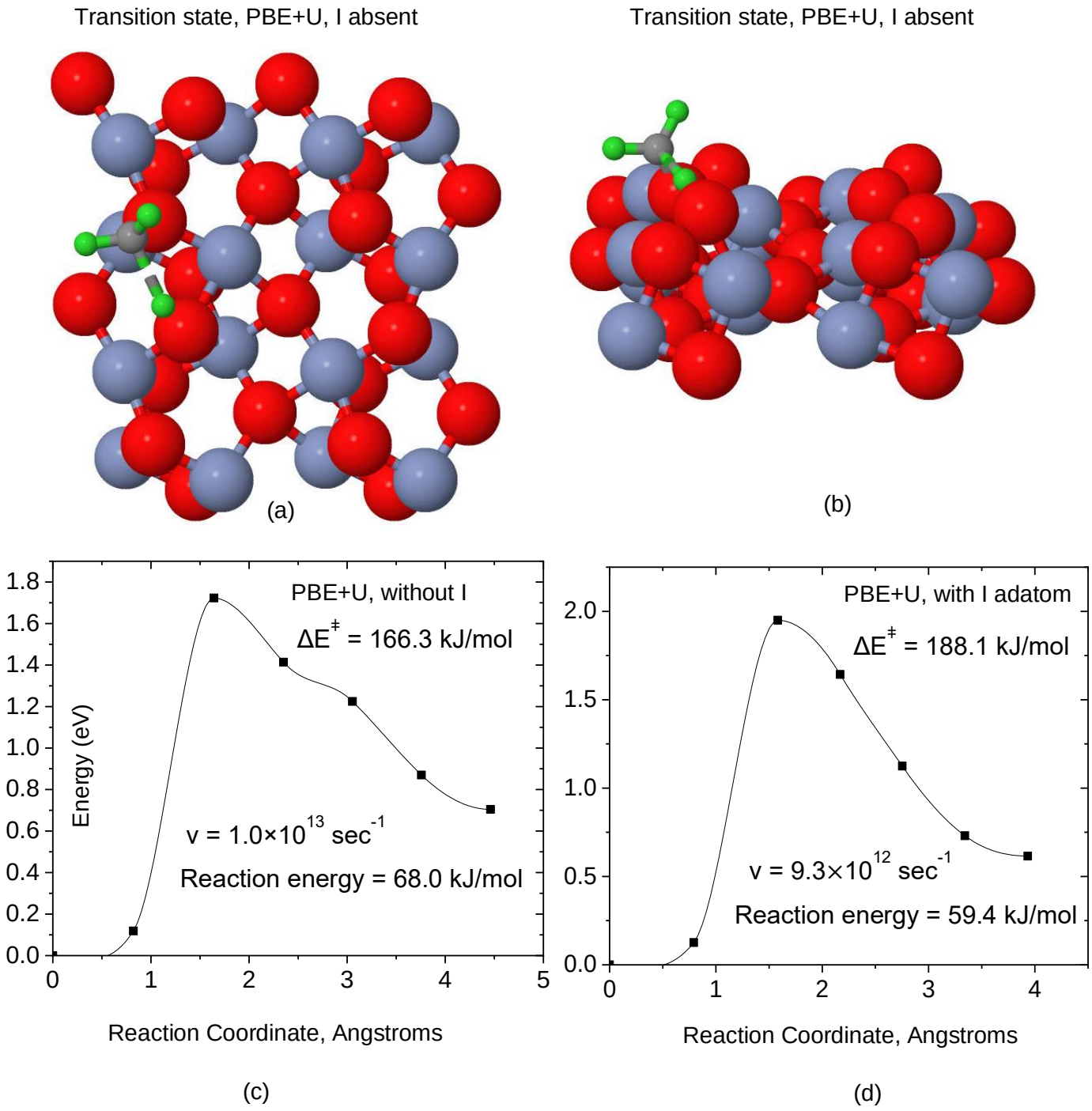

Figure 4-15 The reaction coordinates of the α-hydrogen elimination of a methyl group to form a methylene and a hydrogen on α-Cr_2O_3 $(10\bar{1}2)$, using PBE+U-predicted adsorption configurations for methyl and methylene. Iodine adatom is absent in the first MEP but is present in the second. Reaction barriers ($\Delta E^{\ddagger}$) and reaction energies are labeled.

Compared to the PBE simulations, the performance of PBE+U is again inferior in this case. Absent the iodine adatom, PBE+U gives a less accurate reaction barrier than PBE: 17% higher than the experimental value for PBE+U compared to 1% higher for PBE (table 2). When an I adatom is present, PBE+U becomes even less accurate as the error increases to about 32%, while the barrier for PBE increases to within 7% of the experimental barrier.

4.6 Conclusion

On the nearly-stoichiometric surface of α-$Cr_2O_3(10\bar{1}2)$, the reaction chemistry of CH_3I is similar to that on the metals, where CH_3I dissociates upon adsorption, breaking into an iodine adatom and a surface methyl fragment. TPD experiments indicate that a first-order methyl dehydrogenation (α-hydrogen elimination) reaction with an activation barrier of 135 ± 2 kJ/mol is the rate-limiting elementary step in a reaction sequence that produces ethylene, methane and H_2 as gas phase products. Synchrotron XPS shows that the surface CH_3- groups resulting from C-I bond scission bind at both surface cation and anion sites, while iodine adatoms bind at Cr cation sites. Previous work on the reaction of di-iodomethane, CH_2I_2 confirms that ethylene is formed through the surface diffusion and coupling of methylene, $=CH_2$, fragments [23] which preferentially bind at surface cation sites [24].

DFT simulations showed that PBE gives a reasonable prediction of the binding sites for CH_3- fragments, while PBE+U does not. Both PBE and PBE+U fail to predict the correct binding sites for $=CH_2$ fragments. For simulations of the rate-limiting α-hydrogen elimination reaction from CH_3- run in accordance with the *experimentally-observed*

binding configurations for the carbon species, PBE gives a very accurate prediction on the reaction barrier when an adjacent I adatom is absent, deviating 3 % from the experimental activation barrier. PBE+U gives a poor estimate for the activation barrier (nearly 40% too low) in the absence of an I adatom, but fails spectacularly in simulations including iodine by predicting the initial C-I bond breaking as the rate-limiting step.

When simulations are run in accordance with the *DFT minimum-energy* binding configurations, PBE is still able to accurately predict the reaction barrier (1% to 7% error) because of the similarity in the initial state and transition state which are insensitive to the product methylene binding configuration in the final state. PBE+U gives a more reasonable estimate in this case as well, but with a significantly higher error in comparison to the experimental results (17 to 32% error) than seen with PBE. The greater success for PBE over PBE+U for this system is unexpected given the general assumption that is prevalent in the literature that +U simulations are more appropriate for systems with highly correlated electronic structures. We note however, this conclusion has only been shown to apply in this narrowly-tailored reaction system, where U and J parameters were optimized for the bulk properties.

4.7. Tables

		+U	Prefactors sec^{-1}	Reaction energy	Barrier	Barrier + dZPE	% diff
TPD exp			1.0×10^{13}		135±2	135±2	
PBE			1.3×10^{12}	98.4	149.1	139.3	3%
PBE	I-present		2.3×10^{12}	47.6	135.2	125.5	-7%
PBE+U		U-J=4eV	1.4×10^{13}	43.7	97.4	86.3	-36%

Table 4-1 The predicted prefactors, the thermodynamics, the reaction barriers of the dehydrogenation of methyl groups on α-$Cr_2O_3(10\bar{1}2)$, using experimentally-determined adsorption configurations for the carbon species. +U method is Dudarev.

		+U	Prefactors sec^{-1}	Reaction energy	Barrier	Barrier + dZPE	% diff
TPD exp			1.0×10^{13}		135±2	135±2	
PBE			7.2×10^{12}	92.1	146.4	136.2	1%
PBE	I-present		7.4×10^{12}	-8.1	134.9	124.7	-7%
PBE+U		U-J=4eV	1.0×10^{13}	68.0	166.3	157.5	17%
PBE+U	I-present	U-J=4eV	9.3×10^{12}	59.4	188.1	178.0	32%

Table 4-2 The predicted thermodynamics, the reaction barriers of the dehydrogenation of methyl groups on α-$Cr_2O_3(10\bar{1}2)$, using the adsorption configurations as predicted by DFT for the carbon species. +U method is Dudarev.

References

[1] D.J. Hucknall, Selective Oxidation of Hydrocarbons, Academic Press, 1974.

[2] B.E. Bent, Mimicking aspects of heterogeneous catalysis: generating, isolating, and reacting proposed surface intermediates on single crystals in vacuum, Chemical reviews, 96 (1996) 1361-1390.

[3] H.H. Kung, Transition metal oxides: surface chemistry and catalysis, Elsevier, 1989.

[4] Y. Dong, J.D. Brooks, T.-L. Chen, D.R. Mullins, D.F. Cox, Methylene migration and coupling on a non-reducible metal oxide: The reaction of dichloromethane on stoichiometric α-Cr_2O_3(0001), Surface Science, 632 (2015) 28-38.

[5] Y. Dong, J.D. Brooks, T.-L. Chen, D.R. Mullins, D.F. Cox, Reactions of methyl groups on a non-reducible metal oxide: The reaction of iodomethane on stoichiometric α-Cr_2O_3 (0001), Surface Science, 641 (2015) 148-153.

[6] S.C. York, D.F. Cox, Dehalogenation of 1,1,2-Trichloro-1-fluoroethane over α-Cr_2O_3 (10$\bar{1}$2), The Journal of Physical Chemistry B, 107 (2003) 5182-5189.

[7] S.C. York, D.F. Cox, Dehalogenation of 1-chloro-1-fluoroethene to acetylene on α-Cr_2O_3 (10$\bar{1}$2), Journal of Catalysis, 214 (2003) 273-283.

[8] J.D. Brooks, Q. Ma, D.F. Cox, Reactions of ethyl groups on a model chromia surface: Ethyl chloride on stoichiometric α-Cr_2O_3 (101$\bar{}$2), Surface Science, 603 (2009) 523-528.

[9] C.M. Chiang, T. Wentzlaff, C. Jenks, B. Bent, Carbon–carbon bond forming reactions on Cu (110) surfaces, Journal of Vacuum Science & Technology A: Vacuum, Surfaces, and Films, 10 (1992) 2185-2190.

[10] P. Chuang, Y. Chan, S.-H. Chien, R. Klauser, T. Chuang, Study of alkyl chain propagation by electron beam dissociation of methyl groups on Cu(110), Chemical physics letters, 354 (2002) 179-185.

[11] F. Solymosi, I. Kovacs, K. Revesz, Selective oxygen addition to adsorbed CH_2 and CH_3 on Pd (100), Surface Science, 356 (1996) 121-129.

[12] J.-L. Lin, C.-M. Chiang, C.J. Jenks, M.X. Yang, T.H. Wentzlaff, B.E. Bent, Alkyl chain propagation by methylene insertion on Cu (100), Journal of Catalysis, 147 (1994) 250-263.

[13] W. Huang, J.M. White, A Spectroscopic Investigation of Carbon− Carbon Bond Formation by Methylene Insertion on a Ag (111) Surface: Mechanism and Kinetics, Journal of the American Chemical Society, 126 (2004) 14527-14532.

[14] Q. Yang, K. Maynard, A. Johnson, S. Ceyer, The structure and chemistry of CH_3 and CH radicals adsorbed on Ni (111), The Journal of Chemical Physics, 102 (1995) 7734-7749.

[15] J. Chen, T. Beebe Jr, J. Crowell, J. Yates Jr, Reaction of atomically clean aluminum and chemically modified aluminum with alkyl halides, Journal of the American Chemical Society, 109 (1987) 1726-1729.

[16] C. Bol, C. Friend, Effects of Oxygen Coverage on the Partial Oxidation of Methylene: Reactions of Diiodomethane on Oxygen-Covered Rh (111), Journal of the American Chemical Society, 117 (1995) 11572-11579.

[17] X.-L. Zhou, Z.-M. Liu, J. Kiss, D. Sloan, J. White, Surface Chemistry of Chloroiodomethane, Coadsorbed with H and O, on Pt (111), Journal of the American Chemical Society, 117 (1995) 3565-3592.

[18] M. Chen, S. Bates, R. Van Santen, C. Friend, The chemical nature of atomic oxygen adsorbed on Rh (111) and Pt (111): A density functional study, The Journal of Physical Chemistry B, 101 (1997) 10051-10057.

[19] F. Solymosi, Oxidation of hydrocarbon fragments on metal single crystals and on supported metals, Journal of Molecular Catalysis A: Chemical, 131 (1998) 121-133.

[20] A. Kis, J. Kiss, F. Solymosi, Reaction of CH_2 with adsorbed O on Ru (001) surface, Surface Science, 459 (2000) 149-160.

[21] S. Pak, C.E. Smith, M.P. Rosynek, J.H. Lunsford, Conversion of methyl radicals to methanol and formaldehyde over vanadium oxide catalysts, Journal of Catalysis, 165 (1997) 73-79.

[22] C. Su, J.-C. Yeh, C.-C. Chen, J.-C. Lin, J.-L. Lin, Study of adsorption and reactions of methyl iodide on TiO_2, Journal of Catalysis, 194 (2000) 45-54.

[23] C.M. Byrd, PhD Dissertation: Reaction chemistry of C_1 hydrocarbon fragments and oxygenates on Cr_2O_3(1012), in: Chemical Engineering, Virginia Tech, 2003.

[24] M.A. Minton, D.F. Cox, in, unpublished work.

[25] D. Adler, Insulating and metallic states in transition metal oxides, in: Solid state physics, Elsevier, 1968, pp. 1-113.

[26] E. Newnham, Y.D. Haan, Refinement of the a Al_2O_3, Ti_2O_3, V_2O_3 and Cr_2O_3 structures, Zeitschrift für Kristallographie-Crystalline Materials, 117 (1962) 235-237.

[27] A.H. Hill, A. Harrison, C. Dickinson, W. Zhou, W. Kockelmann, Crystallographic and magnetic studies of mesoporous eskolaite, Cr_2O_3, Microporous and Mesoporous Materials, 130 (2010) 280-286.

[28] L. Corliss, J. Hastings, R. Nathans, G. Shirane, Magnetic structure of Cr_2O_3, Journal of Applied Physics, 36 (1965) 1099-1100.

[29] S.C. York, M.W. Abee, D.F. Cox, α-Cr_2O_3 (1012): surface characterization and oxygen adsorption, Surface Science, 437 (1999) 386-396.

[30] P. Lawrence, S. Parker, P.W. Tasker, Computer simulation studies of perfect and defective surfaces in Cr_2O_3, Journal of the American Ceramic Society, 71 (1988).

[31] P. Tasker, The stability of ionic crystal surfaces, Journal of Physics C: Solid State Physics, 12 (1979) 4977.

[32] R.J. Lad, V.E. Henrich, Structure of α-Fe_2O_3 single crystal surfaces following Ar^+ ion bombardment and annealing in O_2, Surface Science, 193 (1988) 81-93.

[33] J. Moulder, W. Stickle, P. Sobol, K. Bomben, Handbook of X-ray photoelectron spectroscopy; Chastain, J, Perkin-Elmer Corp., Eden Prairie, MN, (1992).

[34] P.E. Blöchl, Projector augmented-wave method, Physical Review B, 50 (1994) 17953-17979.

[35] G. Kresse, D. Joubert, From ultrasoft pseudopotentials to the projector augmented-wave method, Physical Review B, 59 (1999) 1758-1775.

[36] G. Kresse, J. Furthmüller, Efficient iterative schemes for ab initio total-energy calculations using a plane-wave basis set, Physical Review B, 54 (1996) 11169.

[37] G. Kresse, J. Hafner, Ab initio molecular dynamics for liquid metals, Physical Review B, 47 (1993) 558.

[38] G. Kresse, Efficiency of ab-initio total energy calculations for metals and semiconductors using a plane-wave basis set, Computational Material Science, 6 (1996) 15.

[39] J.P. Perdew, K. Burke, M. Ernzerhof, Generalized Gradient Approximation Made Simple, Physical Review Letters, 77 (1996) 3865-3868.

[40] H.J. Monkhorst, J.D. Pack, Special points for Brillouin-zone integrations, Physical Review B, 13 (1976) 5188.

[41] A. Rohrbach, J. Hafner, G. Kresse, Ab initio study of the (0001) surfaces of hematite and chromia: Influence of strong electronic correlations, Physical Review B, 70 (2004) 125426.

[42] H. Jónsson, G. Mills, K.W. Jacobsen, Nudged elastic band method for finding minimum energy paths of transitions, (1998).

[43] G. Mills, H. Jónsson, G.K. Schenter, Reversible work transition state theory: application to dissociative adsorption of hydrogen, Surface Science, 324 (1995) 305-337.

[44] G. Mills, H. Jónsson, Quantum and thermal effects in H_2 dissociative adsorption: Evaluation of free energy barriers in multidimensional quantum systems, Physical Review Letters, 72 (1994) 1124.

[45] X. Li, A.J. Gellman, D.S. Sholl, Density functional theory study of β-hydride elimination of ethyl on flat and stepped Cu surfaces, The Journal of Chemical Physics, 127 (2007) 144710.

[46] K.K. Irikura, Experimental vibrational zero-point energies: Diatomic molecules, Journal of Physical and Chemical Reference Data, 36 (2007) 389-397.

[47] V.I. Anisimov, F. Aryasetiawan, A. Lichtenstein, First-principles calculations of the electronic structure and spectra of strongly correlated systems: the LDA+ U method, Journal of Physics: Condensed Matter, 9 (1997) 767.

[48] S. Dudarev, G. Botton, S. Savrasov, C. Humphreys, A. Sutton, Electron-energy-loss spectra and the structural stability of nickel oxide: An LSDA+ U study, Physical Review B, 57 (1998) 1505.

[49] P.A. Redhead, Thermal Desorption of Gases, Vacuum, (1962) 9.

[50] S.J. Garrett, V.P. Holbert, P.C. Stair, E. Weitz, The adsorption and photochemistry of CD_3I on TiO_2(110), The Journal of Chemical Physics, 100 (1994) 4615-4625.

[51] R.J. Levis, J. Zhicheng, N. Winograd, Thermal decomposition of methanol absorbed on palladium {111}. A new reaction pathway involving methyl formation, Journal of the American Chemical Society, 111 (1989) 4605-4612.

[52] M. Bowker, R. Madix, XPS, UPS and thermal desorption studies of alcohol adsorption on Cu (110): I. Methanol, Surface Science, 95 (1980) 190-206.

[53] J.F. Moulder, W.F. Stickle, P.E. Sobol, K.D. Bomben, Handbook of x-ray photoelectron spectroscopy: a reference book of standard spectra for identification and interpretation of, Perkin-Elmer: Boca Raton, FL, (1992).

[54] X.-L. Zhou, F. Solymosi, P. Blass, K. Cannon, J. White, Interactions of methyl halides (Cl, Br and I) with Ag (111), Surface Science, 219 (1989) 294-316.

[55] X.-L. Zhou, J. White, Alkyl halide photochemistry on Ag (111): III. Methyl iodide, Surface Science, 241 (1991) 270-278.

[56] F. Zaera, Formation and thermal decomposition of ethyl groups on transition metal surfaces: Ethyl iodide on Pt (111), Surface Science, 219 (1989) 453-466.

[57] G. Henkelman, B.P. Uberuaga, H. Jónsson, A climbing image nudged elastic band method for finding saddle points and minimum energy paths, The Journal of Chemical Physics, 113 (2000) 9901-9904.

Chapter 5

DFT Study of Reaction Chemistry of CH_3CH_2Cl on α-$Cr_2O_3(10\bar{1}2)$

5.1 Introduction

The manipulations of the hydrocarbons to produce more commercially lucrative chemicals have always enjoyed ample research interest [1-9] due to the abundance of petrochemicals. The dehydrogenation of the ethane for example, produces a commercially desirable ethylene, and is done in large-scale through steam cracking [10]. However, a catalytic route to ethane dehydrogenation that can lower the temperature (and hence energy costs) and give higher selectivity to ethylene is desirable.

Most ultra-high vacuum (UHV) surface science studies of catalytic ethane dehydrogenation chemistry bypass the initial C-H bond breaking event since ethane desorbs at temperatures lower than those required for C-H bond activation. One method for forming surface alkyl species at low temperature in UHV is through the dissociative adsorption of alkyl halides. The weak C-X (X = halogen) bonds cleave at low temperatures leaving a halogen adatom and a surface alkyl that can be studied with traditional surface science techniques. For example, Jenks and Bent demonstrated that β-hydride elimination occurs on Cu(110), Cu(111) and Cu(100) surfaces [11]. In another example, Solymosi et al. [12] demonstrated that the illumination of adsorbed ethyl iodide can result in ethyl fragments that could undergo the same dehydrogenation on Rh(111). The reaction has even been demonstrated on a non-metallic Si(100) surface [13].

In contrast, there are few studies of this reaction on metal oxide single crystal surfaces. Previous work by Brooks et al. [14] has experimentally examined the reaction of

β-hydrogen elimination from the ethyl groups on α-$Cr_2O_3(10\bar{1}2)$ UHV. The dissociative adsorption of the CH_3-CH_2-Cl on α-$Cr_2O_3(10\bar{1}2)$ produces cation-bound ethyl groups and cation-bound chlorine adatoms as clearly evidenced by synchrotron XPS [14]. Temperature-programmed-desorption (TPD) experiments by Brooks et al. give CH_2=CH_2, H_2, and CH_3-CH_3 as reaction products, with first-order β-hydrogen elimination from of the ethyl group identified as the rate-limiting elementary surface reaction step:

$$\text{-}CH_2\text{-}CH_3 \rightarrow CH_2{=}CH_2 + \text{-}H \quad (1)$$

An activation barrier of 31 kcal/mol (130 kJ/mol) was reported [14], assuming a prefactor of 1×10^{13} sec^{-1}. It was also observed that the activation barrier shows no sensitivity to the coverage of chlorine adatoms, although the activity decreases with increasing Cl coverage due to site blocking of surface cations by Cl adatoms [14].

This work seeks to complement the experimental study of the β-hydrogen elimination from ethyl groups on α-$Cr_2O_3(10\bar{1}2)$ surface by providing DFT simulations of the rate-limiting step in question. The PBE [15] functional is used, and the +U approach [16, 17] is also examined as it is thought to be particular useful for transition metal oxides with highly-correlated electronic structures, such as Cr_2O_3 [18].

5.2 $Cr_2O_3(10\bar{1}2)$

α-Cr_2O_3 has the corundum structure and is an insulator with a band gap of 3.4 eV [19, 20]. The crystal structure is predicated on "a hexagonal close packed array of O^{2-} ions, with two-thirds of the interstitial octahedral sites filled by Cr^{3+} ions" [21]. α-Cr_2O_3 is also anti-ferromagnetic, with ferromagnetic Cr^{3+} sheets having alternating spins in the direction perpendicular to the $(10\bar{1}2)$ surface [18].

A previous study characterizing α-$Cr_2O_3(10\bar{1}2)$ [22] using x-ray photoelectron spectroscopy (XPS), Auger electron spectroscopy (AES), and low-energy electron diffraction (LEED) established that after ion bombardment followed by annealing in ultra-high vacuum at 900 K, a nearly-stoichiometric (1×1) surface can be prepared. This (1×1) surface is illustrated in figure 5-1. The $(10\bar{1}2)$ surface has a rectangular periodicity (a:b = 0.94) [22] and is the most thermodynamically stable of all the low-index surfaces [23]. Previous work by Tasker [24] has shown that for metal oxides, a stable surface termination is expected with a repeating unit of layers that is both neutral in dipole moments and in charge. For α-$Cr_2O_3(10\bar{1}2)$, this leads to a repeat unit of five atomic layers arranged as [O^{2-}, Cr^{3+}, O^{2-}, Cr^{3+}, O^{2-}] along $[10\bar{1}2]$. The O^{2-} anions at the top atomic layer are three-fold coordinated, while the second atomic layer Cr^{3+} cations are five-fold coordinated, resulting in one degree of coordinative unsaturation for each with respect to the bulk [25]. As figure 5-1 (a) shows, the top atomic layer oxygens appear as zig-zag rows in the $[02\bar{2}1]$ direction. Between these zig-zagging rows of oxygen are troughs exposing third atomic layer, fully-coordinated oxygen anions.

5.3 Methods

Calculations were performed using the method of projector-augmented-wave [26, 27] within the Vienna Ab-initio Simulation Package (VASP)[28-30]. The PBE (Perdue-Burke-Ernzerhof) functional, which utilizes a standard generalized gradient approximation (GGA) was used to treat the exchange and correlation in the electronic system [15]. An 80-atom slab consisting of two stoichiometric [O^{2-}, Cr^{3+}, O^{2-}, Cr^{3+}, O^{2-}] repeat units along the $[10\bar{1}2]$ direction is used, exposing a (2×2) surface mesh. A vacuum gap of 15 Å is used to generate the slab geometry. For all calculations, the k-point sampling was generated with a

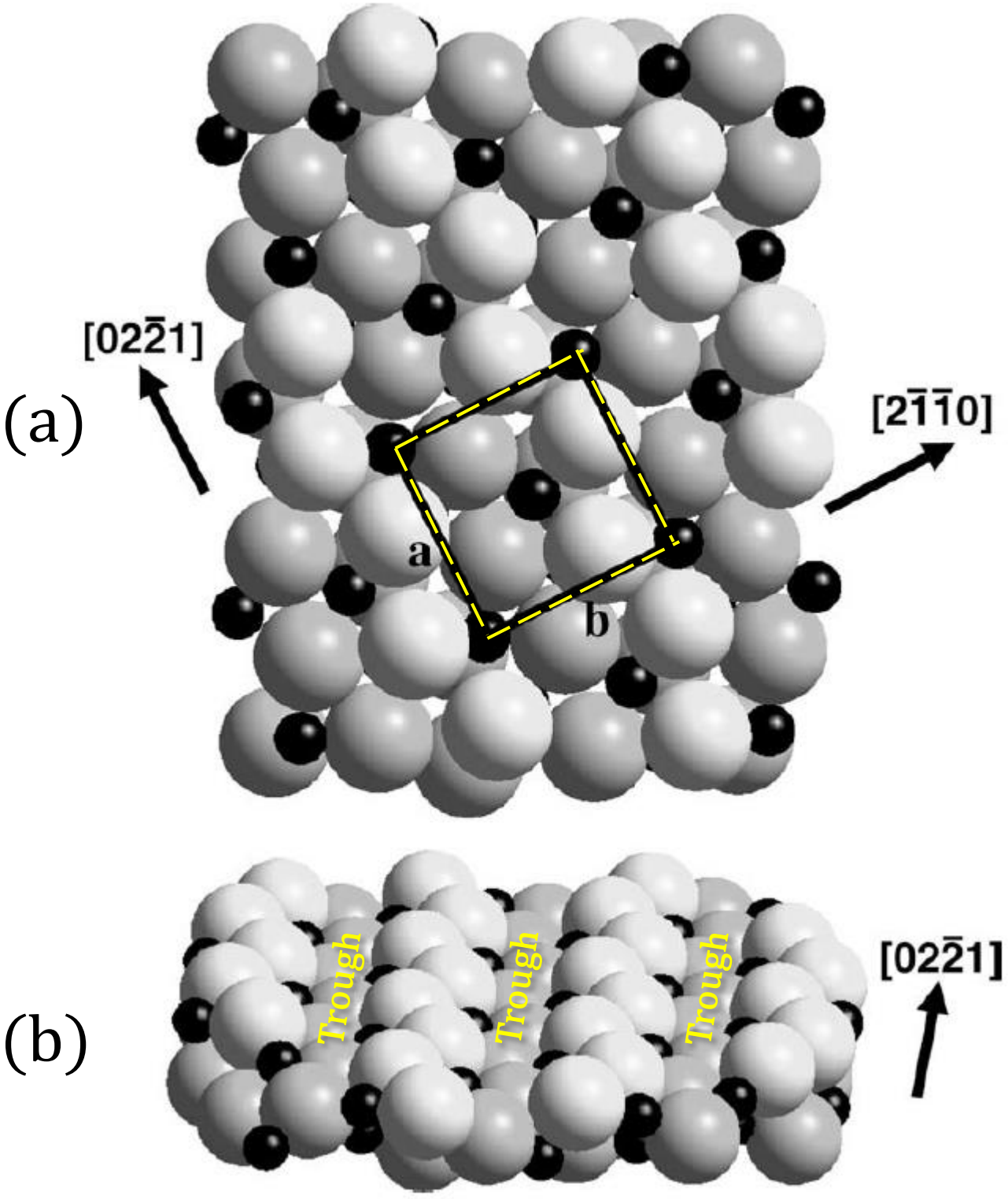

Figure 5-1 Ball model representation of the ideal α-Cr_2O_3 (10$\bar{1}$2) surface. (a) Top view, showing the (10$\bar{1}$2) surface parallel to the plane of the page. Surface periodicity is illustrated with a surface unit cell drawn in yellow dashed line. (b) shows a slanted view of one stoichiometric repeating layer. Small, black spheres represent Cr^{3+} cations, large, light spheres represent O^{2-} anions. Figure adapted with permission from Brooks, et al. (2009).

Monkhorst-Pack scheme [31] using a 3×1×3 mesh for structure and energy calculations. The atoms in the lower repeat unit have their positions fixed, while the atoms in the top five atomic layers were free to move. The initial magnetic moments are set per the known antiferromagnetic ordering in α-Cr_2O_3 [18, 32-34]. In DFT, this ordering is also the ground-state magnetic ordering [35]. The minimum energy pathways (MEPs) for ethyl dehydrogenation were investigated using the climbing-image nudged elastic band method (cNEB) [32-34, 36]. A cut-off energy of 400 eV is used for all calculations. For all geometry-optimized structures, the forces are less than 0.01 eV/Å for individual atoms.

Reaction prefactors are calculated from the normal frequencies of the initial state and transition state via harmonic transition state theory, excluding the one imaginary frequency[37]. The zero-point energy (ZPE) correction for each activation barrier is calculated within the harmonic oscillator approximation [37, 38]. For frequency calculations, the forces are less than 0.0005 eV/ Å.

The prediction of electronic properties of a highly-correlated transition metal oxide such as α-Cr_2O_3, is widely-known to be problematic for DFT [35]. The problem reportedly can be reportedly addressed by including an on-site Coulomb repulsion (DFT+U) [16, 17]. A set of U = 5.0 and J = 1.0 parameters are used as suggested previously for striking a balance between the bulk structural properties and the electronic properties, although this does not guarantee optimal results for surface properties [35]. The DFT+U method used was developed by Dudarev et al. [16].

5.4 Results and discussions

DFT is used to examine both the binding sites of the different surface intermediates for comparison to the experimental XPS results, and to examine the energetics of the rate-limiting, elementary ethyl dehydrogenation (β-hydrogen elimination) step observed in TPD. DFT (PBE) and DFT+U (PBE+U) is used and compared. Additionally, the energetics of the rate-limiting elementary surface reaction step has been examined in the presence and in the absence of Cl adatoms. TPD experiments show that the activation barrier for the reaction is insensitive to the surface coverage of chlorine adatoms, therefore the reaction of isolated ethyl fragments in the absence of chlorine has been considered as a base case. However, it is noted that the use of ethyl chloride as a reactant precludes a chlorine-free experimental situation, since the dissociative adsorption of ethyl chloride is expected to yield an ethyl group and a chlorine adatom on neighboring sites. Hence, both situations (with and without Cl) have been examined to provide insight into the role of surface chlorine adatoms in the simulations.

5.4.1. DFT-predicted reaction coordinates and energetics

Geometry optimizations for PBE and PBE+U were completed for a cation-bound ethyl group (initial state), and for an cation-bound ethylene molecule with one H adatom on the adjacent anion (final state) on the 80-atom cell representing the $(10\bar{1}2)$ surface in VASP in accordance with the experimentally determined binding sites for the intermediate species [14]. This is followed by the determination of the minimum energy pathway (MEP) and the transition state for ethyl dehydrogenation using the cNEB method implemented within VASP.

Figure 5-2 shows the initial and final states for β-hydrogen elimination from an ethyl group bound on a surface Cr^{3+} cation (initial state) and an ethylene molecule adsorbed at the same cation with a hydrogen adatom on an adjacent surface cation (final state) as predicted by PBE. As figure 5-2 (c) shows, the ethyl group is bound at the vacant cation coordination site in the initial state. In the final state, the leaving hydrogen binds to the adjacent oxygen anion, while the ethylene molecule is π-bonded parallel to the surface atop the cation.

Figure 5-3 (a) and (b) shows the transition state geometry for β-hydrogen elimination for the ethyl group as predicted by PBE using the cNEB based on the initial and final states shown in figure 5-2. Also included in figure 5-3 is the associated minimum energy pathway (MEP) for the reaction predicted by PBE in figure 5-3 (c). As figure 5-3 shows, in the transition state the β-hydrogen approaches the adjacent lattice oxygen, while the β-carbon appears to be in transition from a sp^3 hybridization to sp^2. The MEPs show that PBE predicts an activation barrier of 0.96 eV (92.6 kJ/mol), and a reaction that is endothermic by 27.0 kJ/mol. PBE predict a prefactor of 9.3×10^{12} sec^{-1} for the dehydrogenation reaction. These results are listed in table 5-1. Addition of the ZPE corrections gives final values for the activation barrier to be 77.9 kJ/mol for PBE.

Figure 5-4 shows the initial and final states for β-hydrogen elimination from an ethyl group bound on a surface Cr^{3+} cation (initial state) as predicted by PBE+U. As figure 5-4 (c) shows, the ethyl group is bound at the vacant cation coordination site in the initial state. In the final state (5-4 (b) and (d)), the leaving hydrogen binds to the oxygen anion in the second coordination sphere of the cation binding site, while the ethylene molecule is

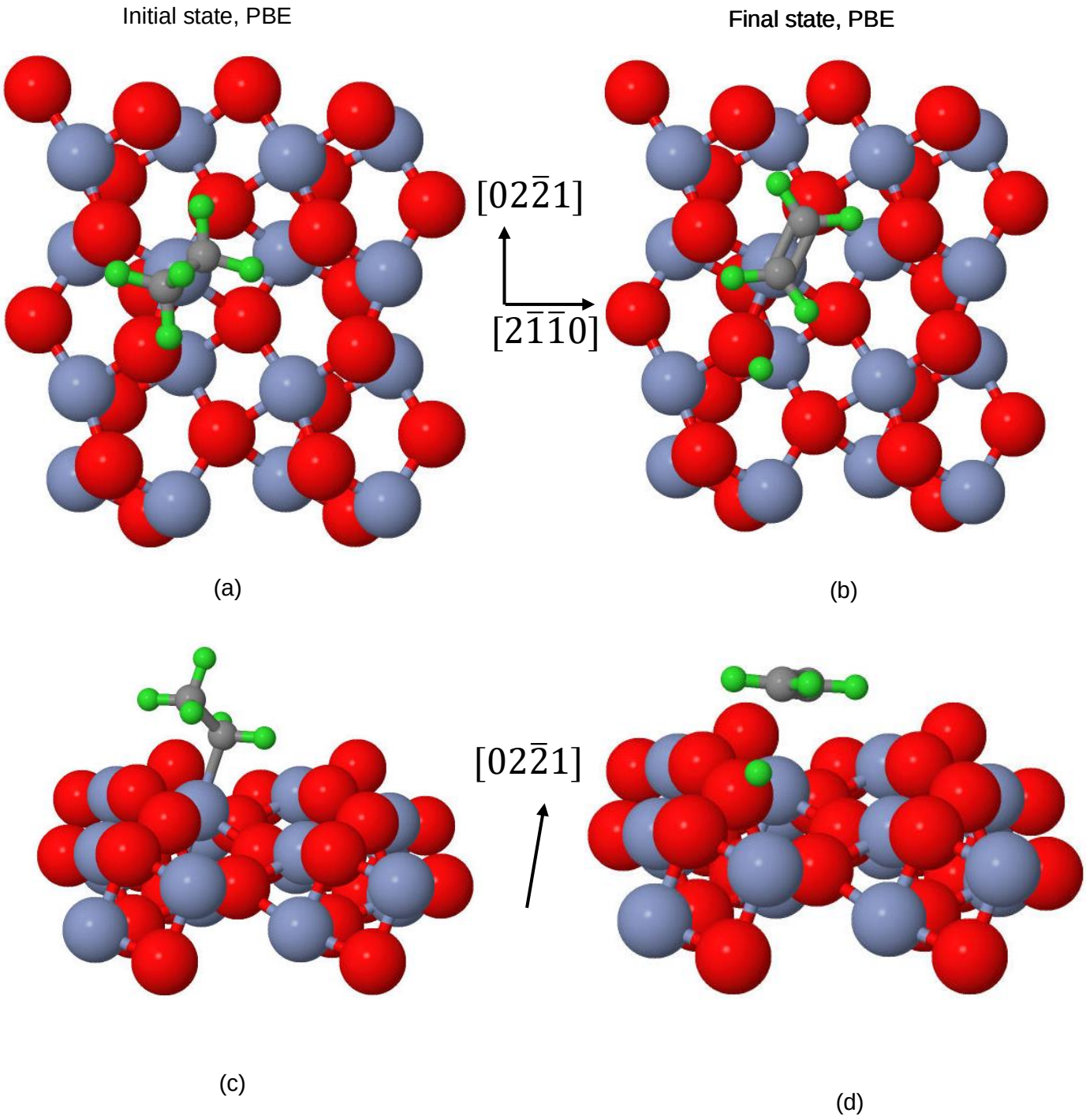

Figure 5-2 Initial state (a and c) and final state (b and d) for β-hydrogen elimination from CH_3CH_2- on the (10$\bar{1}$2) surface, as predicted using the PBE functional. Chromium cations are in light blue, oxygen atoms are in red, carbon atom is in grey, hydrogen in green.

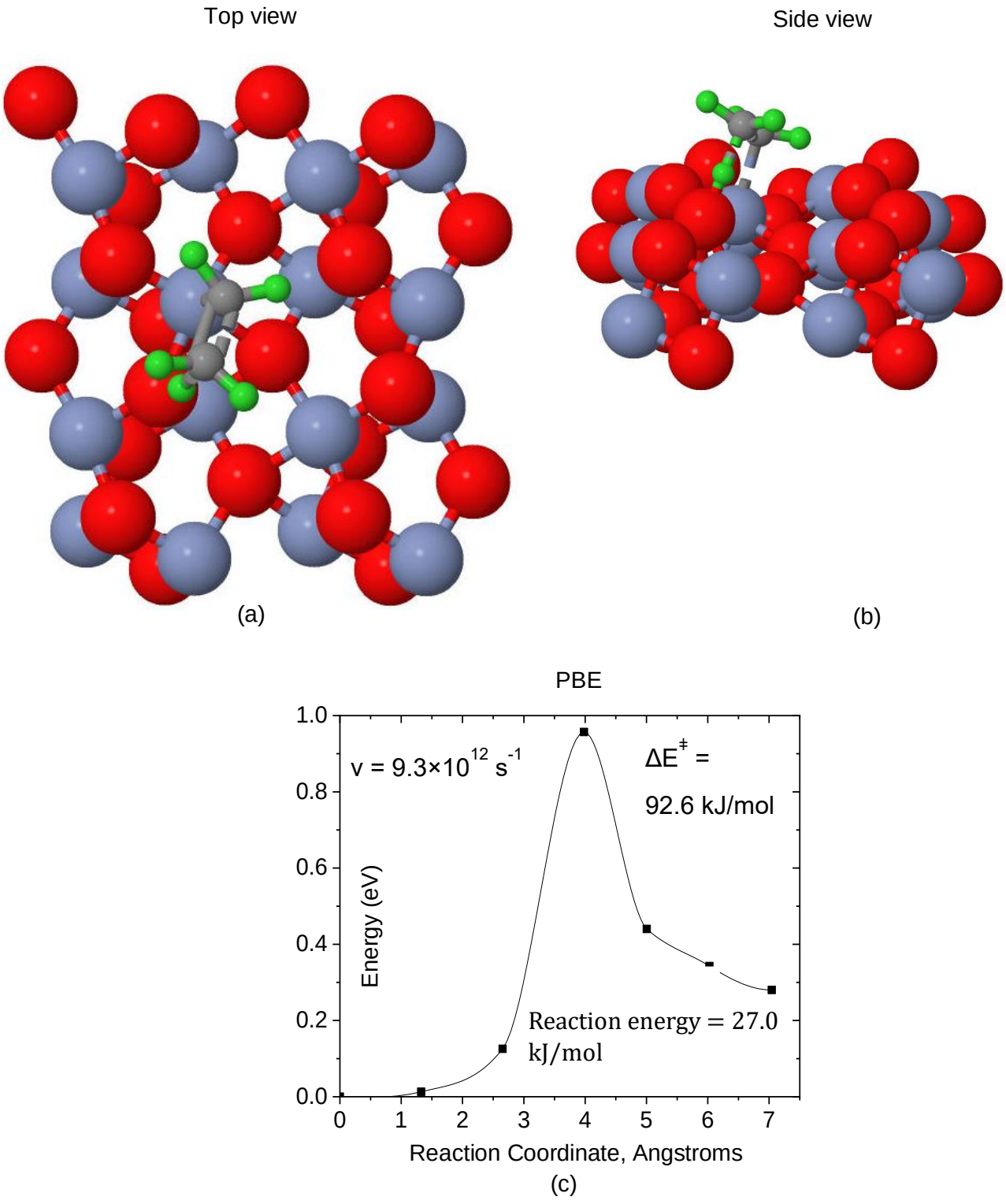

Figure 5-3 The images of the transition state of the dehydrogenation of the ethyl group as determined using the cNEB method with the PBE functional. Minimum energy pathways (MEP) of the dehydrogenation based on PBE (c). Cr cations are in light blue, O anions are in red, C atom is in grey, H in green.

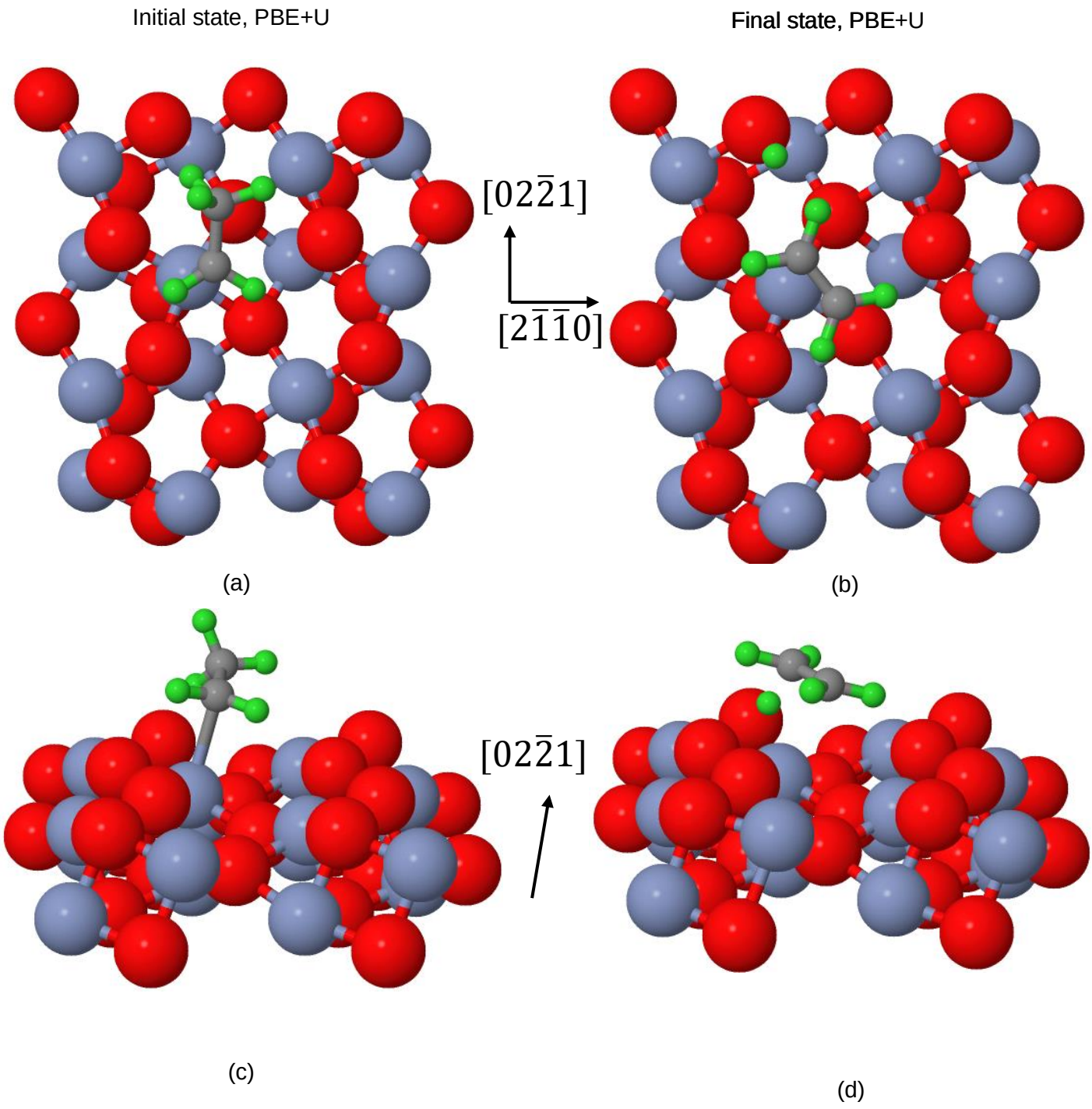

Figure 5-4 Initial state (a and c) and final state (b and d) for β-hydrogen elimination from CH_3CH_2- on the (10$\bar{1}$2) surface, as predicted using the PBE+U. Chromium cations are in light blue, oxygen atoms are in red, carbon atom is in grey, hydrogen in green.

π-bonded atop the cation.

Figure 5-5 (a) and (b) shows the transition state geometry for β-hydrogen elimination for the ethyl group as predicted by PBE+U using the cNEB based on the initial and final states shown in figure 5-4. Also included in figure 5-5 is the associated minimum energy pathway (MEP) for the reaction predicted by PBE+U. As figure 5-5 shows, in the transition state the β-hydrogen approaches a lattice oxygen in the second coordination sphere, while the β-carbon appears to be in transition from a sp^3 hybridization to sp^2. The MEPs show that PBE predicts an activation barrier of 31.0 kJ/mol, and a reaction that is exothermic by 72.5 kJ/mol. PBE+U predict a prefactor of 7.8×10^{11} sec^{-1} for the dehydrogenation reaction. These results are listed in table 5-1. Addition of the ZPE corrections gives final values for the activation barrier to be 25.9 kJ/mol for PBE.

Without chlorine present, PBE and PBE+U both substantially underestimate the experimental activation barrier (130 kJ/mol) for β-hydrogen elimination, with PBE under-predicting by 40%, and PBE+U by a dramatic 80%. Additionally, the two methods predict opposite reaction thermodynamics, endothermic for PBE and exothermic for PBE+U.

These cNEB calculations are repeated with initial and final states of ethyl dehydrogenation (β-hydrogen elimination), shown in figure 5-6, with a Cl adatom present on the adjacent cation across the trough using PBE. The Cl is placed on the cation adjacent to the ethyl fragment as it should provide a more realistic representation of the dissociation of the CH_3CH_2Cl molecule. Only PBE geometries are shown here because PBE+U incorrectly predicts an activation barrier of dissociation of at least 1.8 eV for C-Cl bond breaking of ethyl-chloride as the rate-limiting step, and therefore PBE+U-based

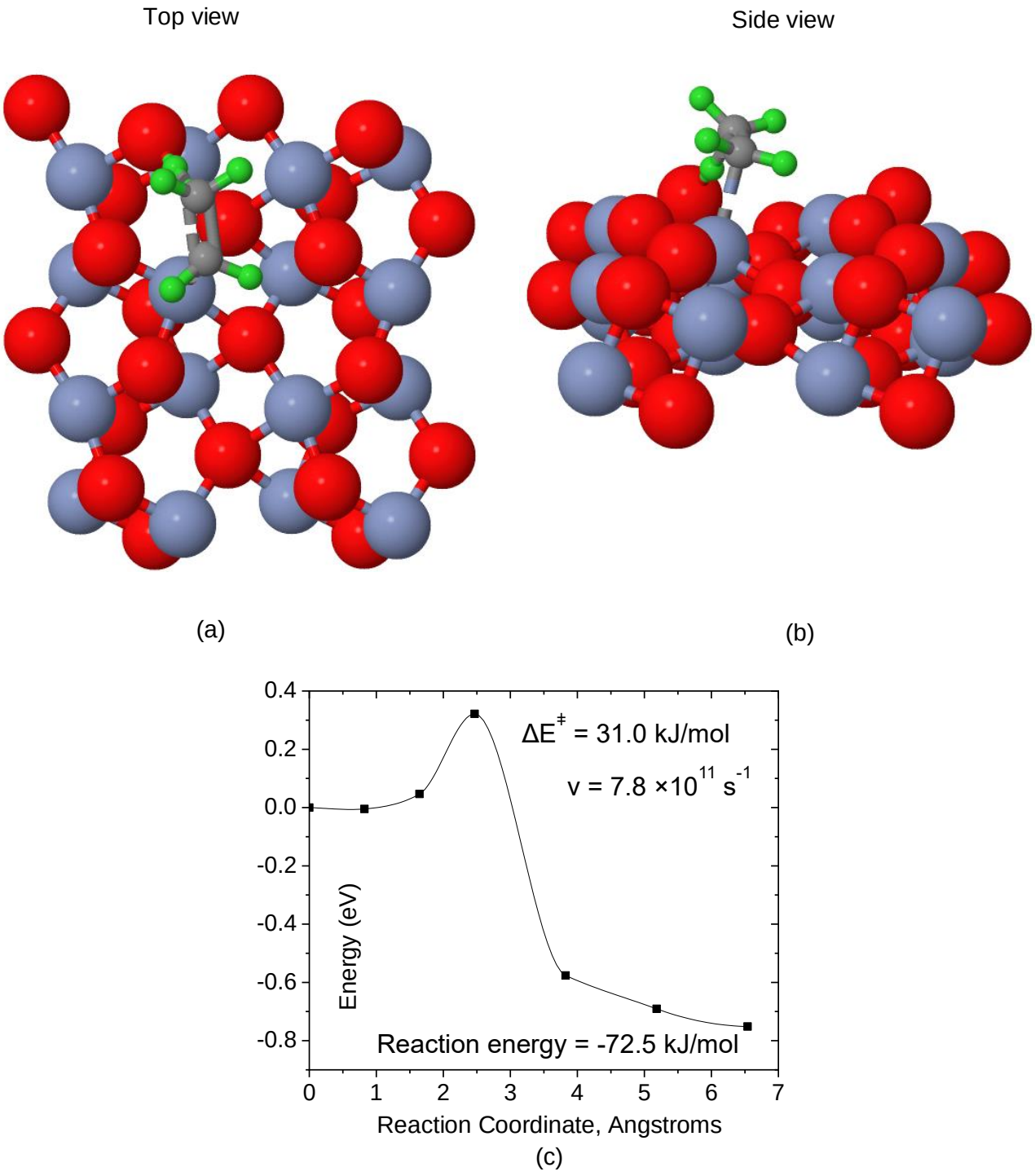

Figure 5-5 The images of the transition state of the dehydrogenation of the ethyl group as determined using the cNEB method with the PBE+U. Minimum energy pathways (MEP) of the dehydrogenation based on PBE+U (c). Cr cations are in light blue, O anions are in red, C atom is in grey, H in green.

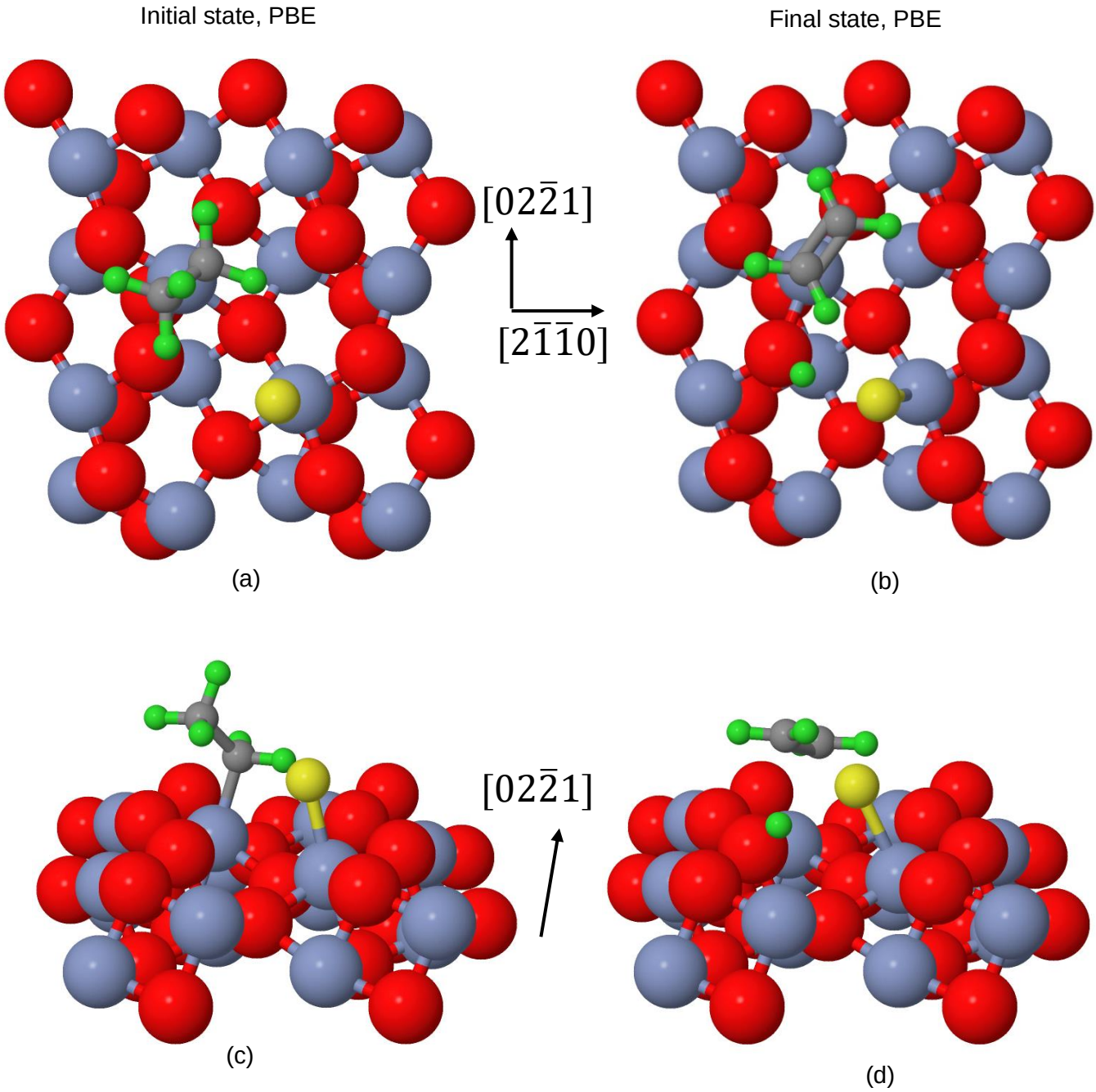

Figure 5-6 Initial state (a and c), and final state (b and d) for β-hydrogen elimination from CH_3CH_2- on (10$\bar{1}$2) surface with Cl present on the adjacent cation. Images are from predictions using PBE functional. Chromium cations are in light blue, oxygen atoms are in red, carbon atom is in grey, hydrogen in green, chlorine in yellow.

cNEB calculations for the dehydrogenation of the ethyl group with Cl present are not discussed here.

The PBE transition state is shown in figure 5-7 (a) and (b). The MEPs predicted by PBE is shown in figure 5-7(c). In the presence of a chlorine adatom, PBE predicts an activation barrier of 93.3 kJ/mol, and the reaction to be exothermic with a heat of reaction of -77.1 kJ/mol. When a surface chlorine adatom is present, PBE gives prefactors of 1.7×10^{13} sec^{-1}. These results are also listed in table 5-1. Following ZPE corrections, the activation barriers are 78.7 kJ/mol, underpredicting the experimental activation energy by 39% in a slight improvement over the previous Cl-absent PBE prediction.

In the case of PBE, the presence of chlorine results in a slight 0.8 kJ/mol increase in activation barrier, but gives a change in the reaction thermodynamics from endothermic to exothermic. This indicates a direct influence of the chlorine adatom in the dehydrogenation process. Overall, PBE simulations performs better than PBE+U simulations for predicting the activation barrier of the β-hydrogen elimination an ethyl groups on the α-$Cr_2O_3(10\bar{1}2)$ surface, since PBE+U incorrectly predicts the C-Cl bond-breaking to be the rate-limiting step, although all the simulations significantly underestimate the activation barrier.

5.5 Conclusion

A computational study of β-hydrogen elimination from an ethyl group on the surface of α-$Cr_2O_3(10\bar{1}2)$ was completed using DFT for comparison to previous experimental work [14]. The simulations show that in the absence of surface chlorine adatoms, PBE predicts a reaction energy of 77.9 kJ/mol, underpredicting the experimental activation barrier by

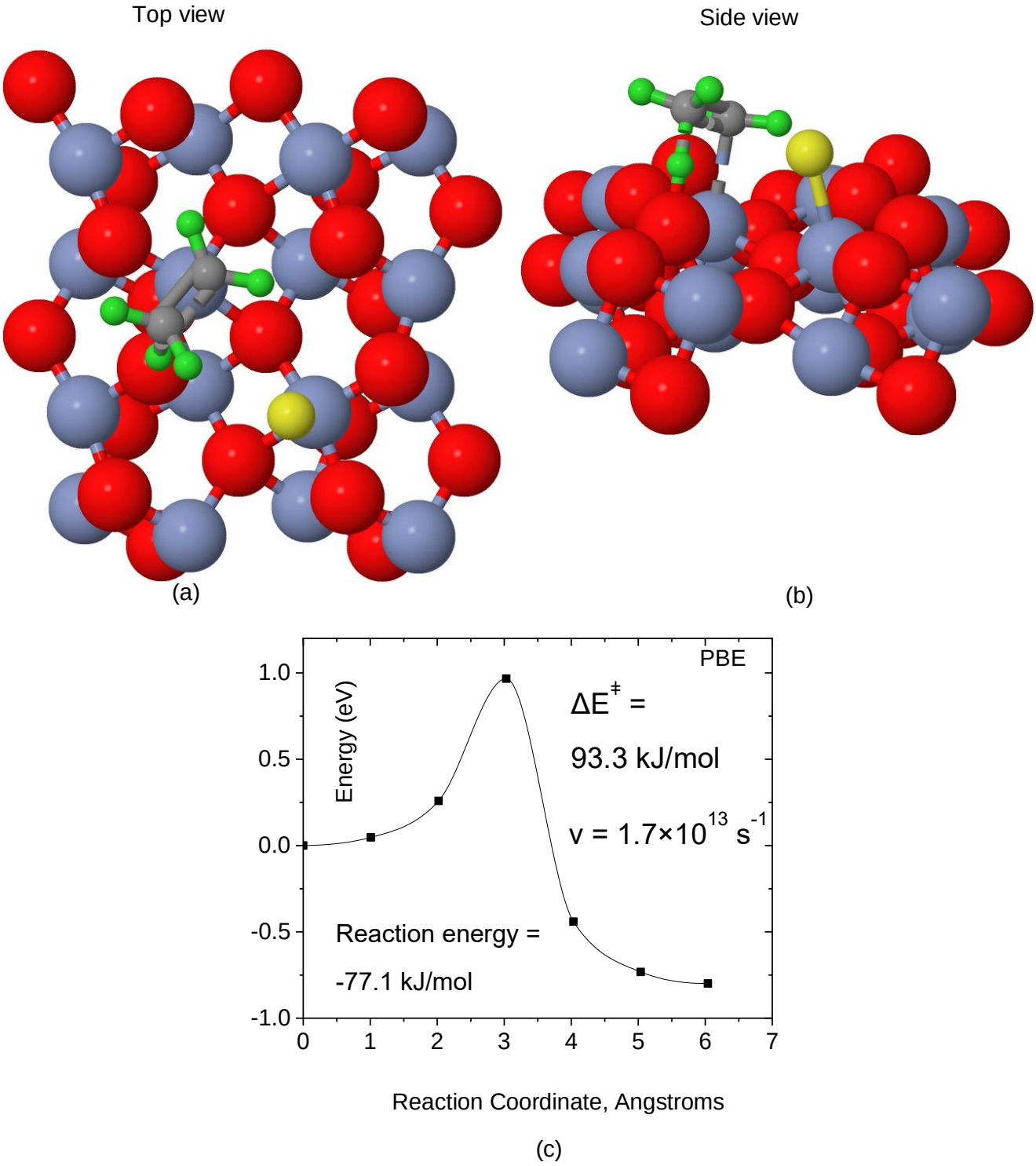

Figure 5-7 Images of the transition state for β-hydrogen elimination from an ethyl group with a surface Cl present. PBE+U gives similar geometries. Minimum energy pathways for the reaction are shown for PBE (c). Cr cations are in light blue, O anions are in red, C atom is in grey, H in green, and Cl in light yellow.

40%. When a chlorine adatom is present, the predicted activation barrier slightly improves. PBE+U drastically underestimates the activation barrier by 80% or more when Cl is absent. When Cl is present, PBE+U incorrectly predicts the C-Cl bond-breaking to be the rate-limiting step. Given the success in of PBE in predicting the barrier for α-hydrogen elimination from surface methyl species, the lack of success with β-hydrogen elimination from surface ethyl species is unexpected. Additionally, the observation of a better performance of PBE vs PBE+U is the opposite of general expectations in the literature for this substrate and reaction system where U and J parameters are optimized for the bulk.

5.6 Tables

		+U	Prefactors	Reaction energy	Barrier	Barrier + dZPE	% diff
			sec^{-1}				
TPD exp			1.0×10^{13}		130	130	
PBE			9.3×10^{12}	27.0	92.6	77.9	-40%
PBE	Cl-		1.7×10^{13}	-77.1	93.3	78.7	-39%
PBE+U		U-J=4eV	7.8×10^{11}	70.6	31.0	25.9	-80%

Table 5-1 The predicted prefactors, thermodynamics and activation barriers for dehydrogenation of ethyl groups on α-$Cr_2O_3(10\bar{1}2)$.

References

[1] Y. Dong, J.D. Brooks, T.-L. Chen, D.R. Mullins, D.F. Cox, Methylene migration and coupling on a non-reducible metal oxide: The reaction of dichloromethane on stoichiometric α-Cr_2O_3(0001), Surface Science, 632 (2015) 28-38.

[2] Y. Dong, J.D. Brooks, T.-L. Chen, D.R. Mullins, D.F. Cox, Reactions of methyl groups on a non-reducible metal oxide: The reaction of iodomethane on stoichiometric α-Cr_2O_3 (0001), Surface Science, 641 (2015) 148-153.

[3] X.-L. Zhou, Z.-M. Liu, J. Kiss, D. Sloan, J. White, Surface Chemistry of Chloroiodomethane, Coadsorbed with H and O, on Pt (111), Journal of the American Chemical Society, 117 (1995) 3565-3592.

[4] M. Smith, L. Zhang, S. Driscoll, U. Ozkan, Effect of surface species on activity and selectivity of MoO_3/SiO_2 catalysts in partial oxidation of methane to formaldehyde, Catalysis letters, 19 (1993) 1-15.

[5] Z. Liang, T. Li, M. Kim, A. Asthagiri, J.F. Weaver, Low-temperature activation of methane on the IrO_2(110) surface, Science, 356 (2017) 299-303.

[6] S. Lillehaug, K.J. Børve, M. Sierka, J. Sauer, Catalytic dehydrogenation of ethane over mononuclear Cr (III) surface sites on silica. part I. C—H activation by σ-bond metathesis, Journal of Physical Organic Chemistry, 17 (2004) 990-1006.

[7] A.D. Baker, C. Baker, C.R. Brundle, D.W. Turner, The electronic structures of methane, ethane, ethylene and formaldehyde studied by high-resolution molecular photoelectron spectroscopy, International Journal of Mass Spectrometry and Ion Physics, 1 (1968) 285-301.

[8] A. De Vekki, S. Marakaev, Catalytic partial oxidation of methane to formaldehyde, Russian Journal of Applied Chemistry, 82 (2009) 521-536.

[9] C. Bol, C. Friend, Effects of Oxygen Coverage on the Partial Oxidation of Methylene: Reactions of Diiodomethane on Oxygen-Covered Rh (111), Journal of the American Chemical Society, 117 (1995) 11572-11579.

[10] A. Bodke, D. Olschki, L. Schmidt, E. Ranzi, High selectivities to ethylene by partial oxidation of ethane, Science, 285 (1999) 712-715.

[11] C.J. Jenks, B.E. Bent, F. Zaera, The chemistry of alkyl iodides on copper surfaces. 2. Influence of surface structure on reactivity, The Journal of Physical Chemistry B, 104 (2000) 3017-3027.

[12] F. Solymosi, L. Bugyi, A. Oszkó, Generation of C_2H_5 species: Thermal and photoinduced dissociation of C_2H_5I on Rh (111), Langmuir, 12 (1996) 4145-4152.

[13] L.A. Keeling, L. Chen, C.M. Greenlief, A. Mahajan, D. Bonser, Direct evidence for β-hydride elimination on Si (100), Chemical Physics Letters, 217 (1994) 136-141.

[14] J.D. Brooks, Q. Ma, D.F. Cox, Reactions of ethyl groups on a model chromia surface: Ethyl chloride on stoichiometric α-Cr_2O_3 ($10\bar{1}2$), Surface Science, 603 (2009) 523-528.

[15] J.P. Perdew, K. Burke, M. Ernzerhof, Generalized Gradient Approximation Made Simple, Physical Review Letters, 77 (1996) 3865-3868.

[16] S. Dudarev, G. Botton, S. Savrasov, C. Humphreys, A. Sutton, Electron-energy-loss spectra and the structural stability of nickel oxide: An LSDA+ U study, Physical Review B, 57 (1998) 1505.

[17] V.I. Anisimov, F. Aryasetiawan, A. Lichtenstein, First-principles calculations of the electronic structure and spectra of strongly correlated systems: the LDA+ U method, Journal of Physics: Condensed Matter, 9 (1997) 767.

[18] L. Corliss, J. Hastings, R. Nathans, G. Shirane, Magnetic structure of Cr_2O_3, Journal of Applied Physics, 36 (1965) 1099-1100.

[19] D. Adler, Insulating and metallic states in transition metal oxides, in: Solid state physics, Elsevier, 1968, pp. 1-113.

[20] E. Newnham, Y.D. Haan, Refinement of the a Al_2O_3, Ti_2O_3, V_2O_3 and Cr_2O_3 structures, Zeitschrift für Kristallographie-Crystalline Materials, 117 (1962) 235-237.

[21] A.H. Hill, A. Harrison, C. Dickinson, W. Zhou, W. Kockelmann, Crystallographic and magnetic studies of mesoporous eskolaite, Cr_2O_3, Microporous and Mesoporous Materials, 130 (2010) 280-286.

[22] S.C. York, M.W. Abee, D.F. Cox, α-Cr_2O_3 (1012): surface characterization and oxygen adsorption, Surface Science, 437 (1999) 386-396.

[23] P. Lawrence, S. Parker, P.W. Tasker, Computer simulation studies of perfect and defective surfaces in Cr_2O_3, Journal of the American Ceramic Society, 71 (1988).

[24] P. Tasker, The stability of ionic crystal surfaces, Journal of Physics C: Solid State Physics, 12 (1979) 4977.

[25] R.J. Lad, V.E. Henrich, Structure of α-Fe_2O_3 single crystal surfaces following Ar^+ ion bombardment and annealing in O_2, Surface Science, 193 (1988) 81-93.

[26] P.E. Blöchl, Projector augmented-wave method, Physical Review B, 50 (1994) 17953-17979.

[27] G. Kresse, D. Joubert, From ultrasoft pseudopotentials to the projector augmented-wave method, Physical Review B, 59 (1999) 1758-1775.

[28] G. Kresse, J. Furthmüller, Efficient iterative schemes for ab initio total-energy calculations using a plane-wave basis set, Physical Review B, 54 (1996) 11169.

[29] G. Kresse, J. Hafner, Ab initio molecular dynamics for liquid metals, Physical Review B, 47 (1993) 558.

[30] G. Kresse, Efficiency of ab-initio total energy calculations for metals and semiconductors using a plane-wave basis set, Computational Material Science, 6 (1996) 15.

[31] H.J. Monkhorst, J.D. Pack, Special points for Brillouin-zone integrations, Physical Review B, 13 (1976) 5188.

[32] H. Jónsson, G. Mills, K.W. Jacobsen, Nudged elastic band method for finding minimum energy paths of transitions, (1998).

[33] G. Mills, H. Jónsson, G.K. Schenter, Reversible work transition state theory: application to dissociative adsorption of hydrogen, Surface Science, 324 (1995) 305-337.

[34] G. Mills, H. Jónsson, Quantum and thermal effects in H_2 dissociative adsorption: Evaluation of free energy barriers in multidimensional quantum systems, Physical Review Letters, 72 (1994) 1124.

[35] A. Rohrbach, J. Hafner, G. Kresse, Ab initio study of the (0001) surfaces of hematite and chromia: Influence of strong electronic correlations, Physical Review B, 70 (2004) 125426.

[36] G. Henkelman, B.P. Uberuaga, H. Jónsson, A climbing image nudged elastic band method for finding saddle points and minimum energy paths, The Journal of Chemical Physics, 113 (2000) 9901-9904.

[37] X. Li, A.J. Gellman, D.S. Sholl, Density functional theory study of beta-hydride elimination of ethyl on flat and stepped Cu surfaces, J Chem Phys, 127 (2007).

[38] K.K. Irikura, Experimental vibrational zero-point energies: Diatomic molecules, Journal of Physical and Chemical Reference Data, 36 (2007) 389-397.

Chapter 6

Conclusions and recommended future work

6.1 Conclusions

In this study, the adsorption of CO and NH_3 on MnO(100) has been studied experimentally using temperature-programmed desorption (TPD) and computationally using density functional theory (DFT). Additionally, density functional theory was used to simulate α-hydrogen elimination from methyl groups, and β-hydrogen elimination from ethyl groups on α-$Cr_2O_3(10\bar{1}2)$ following previous experimental work. This study is done in an effort establish quality experimental benchmarks of adsorption and reaction systems on transition metal oxide with highly-correlated electronic structures, while providing comparative results of DFT calculations.

6.1.1. CO and NH_3 adsorption on MnO(100)

TPD results show that CO undergoes physisorption on MnO(100) surface, with a desorption peak temperature of CO from surface terrace sites at 130 K in the low coverage limit. For calculations, PBE is insufficient to adequately describing the surface geometry upon adsorption of CO on MnO(100), and +U package is essential to address this issue. PBE+U underpredicts the adsorption energy by about 50%. However, with the van der Waals (vdW) correction packages applied, the predicted adsorption energies are in excellent agreement with the experimental results. PBE+U with DFT-D3 method of Becke-Johnson gives the best prediction on adsorption energy.

NH_3 undergoes coverage-dependent adsorption on the MnO(100) surface. In the low-coverage limit, the desorption peak temperature of NH_3 on MnO(100) is 235 K. Similar

to the scenario for CO, the +U is essential for a reasonable prediction of the surface geometry following adsorption. At the low-coverage limit, PBE+U with Tkatchenko-Scheffler method with iterative Hirshfeld partitioning gives the best prediction on the adsorption energy.

While the DFT+U simulations are capable of predicting the adsorption energies to within experimental error when a particular van der Waals correction is applied, it is not clear which vdW correction should be used without the comparison to experimental data.

6.1.2. α-hydrogen elimination from CH_3- and β-hydrogen elimination from CH_3CH_2- on α-$Cr_2O_3(10\bar{1}2)$

For both α-hydrogen elimination from CH_3- and β-hydrogen elimination from CH_3CH_2-on α-$Cr_2O_3(10\bar{1}2)$ PBE provides the better predictions of the activation barrier than does PBE+U. Additionally, PBE+U gives unreasonable prediction on the reaction in some cases. For α-hydrogen elimination from CH_3-, the prediction by PBE in the presence of an iodine on the adjacent cation provides the best prediction of the activation barrier, while for β-hydrogen elimination from CH_3CH_2-, the prediction by PBE in the absence of a Cl provides the best prediction on the activation barrier. Overall, the PBE prediction for α-hydrogen elimination from CH_3- is better than that for β-hydrogen elimination.

Prevalent in the literature is the applications of +U package in addressing the strong correlations between the unpaired d-electrons in the transition metal oxide [1, 2]. Our work has demonstrated this is not always the optimal strategy in the case of surface chemistry.

6.2 Recommendations for Future Work

Future works can be done on completing the CO and NH_3 adsorption studies on α-$Cr_2O_3(10\bar{1}2)$ surface using DFT, after the issue of surface defect is addressed. The obtained experimental adsorption energies can be readily compared to computational results. Additionally, more transition metal oxide with highly-correlated electronic structures, such as α-Fe_2O_3 can be used for developing adsorption and reaction benchmarks.

References

[1] J. Graciani, A.M. Márquez, J.J. Plata, Y. Ortega, N.C. Hernández, A. Meyer, C.M. Zicovich-Wilson, J.F. Sanz, Comparative Study on the Performance of Hybrid DFT Functionals in Highly Correlated Oxides: The Case of CeO_2 and Ce_2O_3, Journal of Chemical Theory and Computation, 7 (2011) 56-65.

[2] E.R. Johnson, A.D. Becke, Communication: DFT treatment of strong correlation in 3d transition-metal diatomics, The Journal of Chemical Physics, 146 (2017) 211105.